Adaptive light-sheet microscopy for long-term, high-resolution imaging in living organisms

Supplementary Information

Loic A. Royer[1,2,*], William C. Lemon[1], Raghav K. Chhetri[1], Yinan Wan[1], Michael Coleman[3], Eugene Myers[2] and Philipp J. Keller[1,*]

[1] *Howard Hughes Medical Institute, Janelia Research Campus*
Ashburn, Virginia, USA
[2] *Max Planck Institute of Molecular Cell Biology and Genetics*
Dresden, Germany
[3] *Coleman Technologies Incorporated*
Newtown Square, Pennsylvania, USA

[*]*Correspondence should be addressed to*
L.A.R. (royer@mpi-cbg.de) and P.J.K. (kellerp@janelia.hhmi.org).

Nature Biotechnology: doi:10.1038/nbt.3708

Supplementary Methods

Supplementary Methods 1	Software and hardware architecture
Supplementary Methods 2	Image quality metrics in theory and practice
Supplementary Methods 3	Special optimization theory for spatiotemporally adaptive imaging
Supplementary Methods 4	General optimization theory for spatiotemporally adaptive imaging
Supplementary Methods 5	Analysis of three-dimensional light-sheet geometry
Supplementary Methods 6	Quantifying improvements in spatial resolution and image quality

Supplementary Figures

Supplementary Figure 1	Light-sheet microscope design for spatiotemporally adaptive imaging
Supplementary Figure 2	Digital control of three-dimensional light-sheet orientation
Supplementary Figure 3	Side-by-side comparison of focus metrics
Supplementary Figure 4	Synthetic benchmarks for evaluating focus metrics
Supplementary Figure 5	Application of DCTS focus metric to light-sheet image data
Supplementary Figure 6	Recovering focus information for image data with challenging properties
Supplementary Figure 7	Minimizing focus metric errors by using low-pass filtering
Supplementary Figure 8	Degrees of freedom and workflow of spatiotemporally adaptive imaging
Supplementary Figure 9	General optimization theory for spatiotemporally adaptive imaging
Supplementary Figure 10	Online perturbation benchmark of adaptive imaging performance
Supplementary Figure 11	Analysis and system calibration of light-sheet angles alpha and beta
Supplementary Figure 12	Whole-brain functional imaging using the adaptive imaging framework
Supplementary Figure 13	Spatiotemporally adaptive imaging of *Drosophila* embryonic development
Supplementary Figure 14	Improving resolution and signal strength in *Drosophila* embryos
Supplementary Figure 15	Improving resolution and signal strength in zebrafish embryos
Supplementary Figure 16	Adaptive axial positioning of the light-sheet waist
Supplementary Figure 17	Spatial dependency of light-sheet angle beta in a *Drosophila* embryo
Supplementary Figure 18	Modeling spatial variance of light-sheet angle beta in a *Drosophila* embryo
Supplementary Figure 19	Physiology controls for adaptive imaging of zebrafish embryogenesis

Supplementary Tables

Supplementary Table 1	Synthetic performance benchmarks for evaluating focus metrics
Supplementary Table 2	Dependency of synthetic focus metric performance on low-pass filtering
Supplementary Table 3	Real-data performance benchmarks for evaluating focus metrics
Supplementary Table 4	Dependency of real-data focus metric performance on low-pass filtering
Supplementary Table 5	Protocol for adaptive imaging in the system perturbation benchmark
Supplementary Table 6	Protocol for adaptive imaging of *Drosophila* embryonic development
Supplementary Table 7	Protocol for adaptive imaging of zebrafish embryonic development
Supplementary Table 8	Protocol for interleaved imaging of zebrafish embryonic development
Supplementary Table 9	Protocol for adaptive two-color imaging of nervous system development
Supplementary Table 10	Protocol for adaptive whole-brain functional imaging
Supplementary Table 11	Light-sheet microscope for spatiotemporally adaptive imaging

Supplementary Videos

Supplementary Video 1	Perturbation benchmark of spatiotemporally adaptive imaging performance
Supplementary Video 2	Spatiotemporally adaptive imaging of *Drosophila* embryogenesis
Supplementary Video 3	Recovery of high spatial resolution in *Drosophila* adaptive imaging
Supplementary Video 4	Recovery of cellular resolution in deep tissue layers by adaptive imaging
Supplementary Video 5	Spatiotemporally adaptive imaging of zebrafish embryogenesis
Supplementary Video 6	Recovery of high spatial resolution in zebrafish adaptive imaging
Supplementary Video 7	Quantification of resolution improvements in zebrafish adaptive imaging
Supplementary Video 8	Spatiotemporally adaptive two-color imaging of neural development
Supplementary Video 9	Spatiotemporally adaptive whole-brain functional imaging in larval zebrafish
Supplementary Video 10	Example of system drift during non-adaptive long-term imaging

Supplementary Methods

Overview

In the following sections, we first provide details on the software and hardware architecture used in our framework for spatiotemporally adaptive imaging with light-sheet microscopy (**Supplementary Methods 1**). Second, we provide a systematic analysis of image quality metrics and discuss the design principles of our synthetic and real-data benchmarks for identifying the best image quality metric for light-sheet microscopy (**Supplementary Methods 2**). Third, we provide the mathematical theory behind local adaptive optimization in multi-axis illumination and multi-axis detection light-sheet microscopes (**Supplementary Methods 3**). Fourth, we formulate a general theory of spatiotemporally adaptive imaging using global optimization of all degrees of freedom for all imaging depths and colors across the specimen volume (**Supplementary Methods 4**). Fifth, we discuss the theory and concepts behind the image-based reconstruction of three-dimensional light-sheet orientation inside the specimen (**Supplementary Methods 5**). Sixth, we describe the methods used to estimate improvements in spatial resolution and image quality (**Supplementary Methods 6**).

Nature Biotechnology: doi:10.1038/nbt.3708

Part I | Software and Hardware Architecture

Our framework is an integrated system consisting of a light-sheet microscope equipped with digitally controllable piezo positioners and galvanometer scanners for positioning and orienting light-sheet and detection focus planes, real-time electronics, microscope control software for spatiotemporally adaptive imaging, algorithms for image quality estimation and three-dimensional light-sheet geometry reconstruction, as well as algorithms for system optimization. In the following section we provide details about the system architecture, from mechano-optical degrees of freedom to control electronics and main software sub-systems.

Mechano-optical design of light-sheet microscope for spatiotemporally adaptive imaging

A computer model of the light-sheet microscope is shown in **Supplementary Fig. 1**, which employs a color code to identify the various microscope components responsible for providing digital access to the 10 primary degrees of freedom required for spatiotemporally adaptive imaging.

Digital control of position and orientation of light-sheet and detection focus planes

In order to optimize image quality and spatial resolution during long-term imaging of dynamic biological processes, such as whole-embryo development or the formation of tissues and organs, our approach to spatiotemporally adaptive imaging relies on digital control of the ten degrees of freedom characterizing relative offsets and angles between all light sheets and detection focal planes. By automating the control of these degrees of freedom, the adaptive imaging framework is able to compensate for spatiotemporal changes in the specimen's optical properties, local and global distribution and maturation of fluorescent markers, and mechanical and thermal drift in various microscope components.

A key requirement for exploiting the full potential of the multiview light-sheet microscope in providing high-quality image data is the precise digital control of the following degrees of freedom:

- For precise control of the position of detection focal planes (D_1 and D_2) along the optical axis of the respective detection system, both detection objectives of the light-sheet microscope are mounted on P-622.1CD Hera piezo positioners with 250 µm travel range, operated with E-665 piezo amplifiers and controllers (Physik Instrumente).
- For precise control of the position of light-sheet waists (Y_1 and Y_2) along the optical axis of the respective illumination system, both illumination objectives of the light-sheet microscope are mounted on P-628.1CD Hera piezo positioners with 800 µm travel range, operated with E-665 piezo amplifiers and controllers (Physik Instrumente).
- For precise control of light-sheet offsets perpendicular to the optical axis of the respective illumination system (I_1 and I_2) as well as roll (α_1 and α_2) and yaw (β_1 and β_2) light-sheet angles in sample space, we use two pairs of dual-axis 6215H galvanometer scanners (Cambridge Technology) in the illumination arms of the light-sheet microscope. In each

Nature Biotechnology: doi:10.1038/nbt.3708

illumination arm, the first dual-axis scanner is conjugated to the specimen plane and controls the angular orientation of the light sheet in sample space, whereas the second dual-axis scanner is conjugated to the objective back focal plane and controls the lateral light-sheet offset (and also facilitates scanned light-sheet illumination itself).

Implementation of digital control of light-sheet roll and yaw angles

In a light-sheet microscope utilizing laser scanning for planar illumination[1], a Gaussian "pencil beam" is rapidly scanned across the sample to create a thin light sheet. The use of a dual-axis galvanometer scanner, such as the Cambridge Technology model 6215H used in the microscope described here, facilitates not only light-sheet scanning itself but also offsetting the light sheet perpendicular to the illumination axis and controlling the 'roll' angle α, i.e. light-sheet rotation about the propagation axis of the illuminating laser beam. However, the 'yaw' angle β, i.e. rotation about the axis defined by the points representing the location of the scanned Gaussian beam waist, can only be adjusted by either physically displacing the light-sheet galvanometer scanner laterally or displacing the illumination beam at the light-sheet galvanometer scanner laterally. The first approach, in addition to being cumbersome, does not allow the flexibility of integration of the 'yaw' angle into an automated, digital control framework. Below, we describe the implementation of the second approach by using a second dual-axis galvanometer scanner in the illumination path that allows the light sheet to be pivoted by β in the sample plane in a digitally controlled manner.

A dual-axis pivot galvanometer scanner (see **Supplementary Fig. 2** and components labeled PG1 and PG2 in **Supplementary Fig. 1**) is positioned at a focal-distance between two relay lenses such that the collimated beam from the laser is focused onto the vertical scanning mirror by the first relay lens, and the second relay lens restores collimation and directs the beam onto the dual-axis light-sheet galvanometer scanner (see **Supplementary Fig. 2** and components labeled LG1 and LG2 in **Supplementary Fig. 1**). By adjusting the tilts of the scanning mirrors (L and V in **Supplementary Fig. 2**; L: lateral scanning mirror, V: vertical scanning mirror), the illumination beam can be positioned off the optical axis anywhere in the XZ plane. The beams along the optical axis and the pivoted beam are illustrated in blue and red, respectively, in **Supplementary Fig. 2**. We note that the orientation of the pivot plane, illustrated in shaded red in **Supplementary Fig. 2b**, flips by $(90°-\eta)$ as it exits the dual-axis light-sheet galvanometer scanner, where η is the angle between the shafts of the two scanning mirrors in the light-sheet galvanometer scanner (for Cambridge Technology 6215H using 61021506R40 XY-mount, η is 17°). Thus, the pivot galvanometer scanner needs to displace the beam by an optical angle of θ_x to create the lateral displacement after the light-sheet galvanometer scanner, and additionally, to correct for the shaft-angle η, the beam needs to also be displaced by θ_z, as illustrated in **Supplementary Fig. 2**. Cumulatively, the beam is displaced by an angle γ with respect to the optical axis as measured at the vertical scanning mirror (V), where the illumination beam is brought to focus. This culminates in the light sheet being pivoted by an angle β about the line of light-sheet focus in the sample plane.

Nature Biotechnology: doi:10.1038/nbt.3708

Parameterization of light-sheet roll and yaw angles

The following mathematical relationships help establish the optical angles θ_x and θ_z to be generated by the vertical and lateral mirrors of the pivot galvanometer scanner, respectively. The deviation of the beam from the optic-axis γ is given by:

$$\gamma = \tan^{-1}\left(\frac{OP}{f_R}\right) \quad \text{(Eq. 1)}$$

In Eq. 1, f_R is the focal length of the relay lens. The pivot angle in the sample plane is given by:

$$\beta = \tan^{-1}\left(\frac{M \times OP}{f_{f\theta}}\right) \quad \text{(Eq. 2)}$$

In Eq. 2, M is the magnification of the tube lens and the objective given by f_{TL}/f_{obj}, and $f_{f\theta}$ is the focal length of the f_θ-lens. Thus, we can re-write the deviation of the beam from the optical axis γ in terms of known quantities as follows:

$$\gamma = \tan^{-1}\left(\frac{1}{f_R} \times \frac{f_{f\theta}}{M} \times \tan\beta\right) \quad \text{(Eq. 3)}$$

Note that, in the above equations, all angles are defined in free space. Experimentally, the pivot angle is in the immersion medium and is given by $\beta_m = \beta/n_m$, where n_m is the refractive index of the immersion medium. Hence, once the intended pivot β (or, β_m) is defined, the deviation of the beam from the optical axis γ can be obtained using the above relationship, and the optical angles to be generated by the two scanning mirrors in the pivot galvanometer scanner can be ascertained using the following equations derived using the geometric configuration shown in **Supplementary Fig. 2b**:

$$\theta_x = \tan^{-1}(\tan\gamma \times \cos\eta) \quad \text{(Eq. 4)}$$

$$\theta_z = \tan^{-1}\left[\frac{\tan\gamma \times \sin\eta}{\sqrt{1 + \tan^2\gamma\cos^2\eta + 2\left(\frac{\Delta}{f_R}\right) + \left(\frac{\Delta}{f_R}\right)^2}}\right] \quad \text{(Eq. 5)}$$

In Eq. 5, Δ is the separation between the L and V scanning mirrors in the pivot galvanometer scanner.

Nature Biotechnology: doi:10.1038/nbt.3708

Detailed list of microscope hardware components

Our custom light-sheet microscope for spatiotemporally adaptive imaging consists of a laser system, two illumination arms, two detection arms, a custom specimen chamber, a four-axis specimen positioning system, a computer workstation and real-time electronics for microscope control and data acquisition, custom LabVIEW-based software for microscope control and custom Java/LabVIEW-based software for spatiotemporally adaptive imaging. An overview of the components of this microscope is provided below and in tabular form in **Supplementary Table 11**.

The two layers of the microscope (comprising optics and sample positioning hardware, respectively) are assembled on a custom RG grade breadboard (Newport, custom product code 04SI69108) and an ST-UT2-48-8 optical table equipped with an IQ-200-YG-8 damper upgrade, supported by four S-2000 series 28" isolators with automatic leveling (Newport).

The laser illumination unit consists of a pulsed Ti:Sapphire laser (Chameleon Ultra II, Coherent), beam-splitting optics (Melles Griot, Casix, Linos) for supplying both illumination arms with IR laser beams, a laser array with three solid-state lasers coupled into a dual-port fiber module (SOLE-3, Omicron), fiber collimators and dichroic mirrors for combining laser beams in the visible and IR portions of the spectrum.

Each illumination arm consist of a laser shutter (VS14S2ZM1-100, Uniblitz), a filter wheel (96A351, Ludl) equipped with notch and neutral density filters (Chroma and Melles Griot), a two-axis galvanometer scanner with silver-coated 6 mm mirrors for scanned light-sheet formation and positioning (Cambridge Technology), a two-axis galvanometer scanner with silver-coated 6 mm mirrors for light-sheet pivoting (Cambridge Technology), a lens pair (Edmund Optics), a custom f-theta lens supporting 488-1100 nm laser wavelengths (66-S80-30T-488-1100nm, Special Optics) and two sets of matched tube lenses and illumination objectives (Olympus and Nikon; optimized for one- and two-photon excitation, respectively).

Each detection arm consists of a high numerical aperture water-dipping detection objective (16x/0.8 NA, Nikon; or 20x/1.0 NA, Carl Zeiss), a matched tube lens (Nikon or Carl Zeiss), a filter wheel (96A354, Ludl) equipped with band-, short- and long-pass filters (Semrock and AHF), and an sCMOS camera (Orca Flash 4.0 V2, Hamamatsu).

The real-time electronics framework consists of a PXI-8110 real-time controller equipped with four PXI-6733 high-speed analog output boards, a PXI-8432/2 serial interface board and a PXI-7354 four-axis stepper/servo motion controller (National Instruments), as well as a C-809.40 four-channel servo amplifier (Physik Instrumente) and four BNC-2110 shielded connector blocks (National Instruments).

The microscope control software operates on a high-performance computer workstation (Colfax International) for image acquisition and short-term data storage. This workstation is equipped with two Xeon E5-2687W CPUs (Intel), 192 GB of memory allocated to imaging ring buffers, 14 SAS hard disks (2.5 XE 900 GB, Western Digital) combined into two RAID-0 arrays using an RS2WG160 SAS RAID controller (Intel) for concurrent streaming from two sCMOS cameras and an X520-SR1 10G fiber controller (Intel) for data offloading to the storage server.

Nature Biotechnology: doi:10.1038/nbt.3708

Overview of software architecture

The custom microscope control software consists of three primary modules, including the AutoPilot libraries and two modules for microscope control:

i) A software layer for real-time control and synchronization of all electronics components used in the microscope (incl. cameras, filter wheels, shutters, piezo positioners, galvanometer scanners, motorized stages, Pockels cell and laser systems) and execution of the imaging workflow. This module was written in 32-bit LabVIEW and deployed on the PXI-8110 real-time controller.

ii) A software frontend that consists of modules for receiving, processing and online visualization of image data streams and a graphical user interface (GUI) for configuring imaging experiments and AutoPilot-based microscope control. This module was written in 64-bit LabVIEW and deployed on the host computer.

iii) A set of AutoPilot libraries facilitating all core computations and system optimization associated with the AutoPilot framework. These libraries were written in Java and C/C++.

Microscope control software

The microscope control software was developed using the LabVIEW development environment (version 2012, National Instruments). The application uses a distributed architecture, with the user interface, image acquisition and file logging located on a high performance workstation and the instrument control, waveform generation, and experiment sequencing control software located on a real-time control system (PXI-8110, National Instruments). The PXI chassis also holds four PXI-6733 8-channel analog output modules, which are used to control galvanometer scanners, laser modulation, camera triggers, piezo positions and shutter states. Other PXI modules are used to control filter wheels and sample stage motion. The host computer and the real-time controller communicate via a TCP/IP server client architecture.

AutoPilot software library

The AutoPilot library was written in Java. This library, which is freely available at *https://microscopeautopilot.github.io*, contains the code for (i) all focus/image quality metrics evaluated as part of this work, (ii) the programming interface for microscope state modeling and optimization, (iii) the algorithms for mapping the 3D geometry of the light-sheet inside the sample and (iv) C/C++ interfaces for AutoPilot integration into the LabVIEW control software.

Nature Biotechnology: doi:10.1038/nbt.3708

Part II | Image Quality Metrics in Theory and Practice

After detailing the methodological requirements motivating our systematic investigation of image quality metrics, we provide information about the mathematical notation used throughout this section and discuss general theoretical concepts underlying image quality metrics. We then review 30 different image quality metrics. Some of these metrics are taken from existing literature while others are either new or modified from existing metrics. We evaluate these measures on synthetic and real-data benchmarks and identify the best image quality metrics for light-sheet microscopy.

Alignment and focus optimization in light sheet microscopy

A fundamental challenge in spatiotemporally adaptive imaging and optimizing the system state of complex, multi-axis microscopes is the estimation and comparative analysis of image quality. Mechanical or optical proxy measurements (e.g. phase detection autofocus) cannot serve as substitutes for an image quality metric because they first need to be calibrated against image quality and are subsequently susceptible to the same mechanical and thermal drifts that affect optical paths in the microscope. It follows that robust and computationally efficient measures of image quality are essential for the development of microscopes capable of spatiotemporal self-optimization. Mismatches in the geometry of light-sheet and detection focal planes of the light-sheet microscope cause image quality to degrade, primarily by defocus in a first-order approximation.

Image quality metrics have been studied extensively within the computer vision field[2-6]. However, existing metrics have never been evaluated for the purpose of automated image analysis in light-sheet microscopy. Importantly, imaging with light-sheet microscopy is very different from other imaging modalities such as wide-field microscopy and photography. Optical sectioning of a thin volume is achieved with spatially confined illumination. Subsequently, an image of this volume section is acquired using an objective with a similarly thin depth of field. Different parts of the illuminated volume appear more or less in focus depending on their position relative to the detection focal plane. Further differences arise from the hyperbolic axial profile of the Gaussian light sheet, aberrations introduced by the sample, and loss of contrast as a result of light scattering. Moreover, the relative impact of noise increases with increasing imaging speed and decreasing exposure time. Thus, a thorough evaluation of existing image quality metrics is indispensable in order to identify the best-performing metrics for the purpose of adaptive imaging in light-sheet microscopy and to determine how these metrics can be further improved.

Mathematical notation

In the following, I is a two-dimensional image with pixel intensities $I_{x,y}$. The number of pixels in the image I is denoted by $n(I)$. The width and height of image I are $w(I)$ and $h(I)$, respectively. For simplicity we adopt the convention that the expression $I_{x,y}$ corresponds to the pixel value of

Nature Biotechnology: doi:10.1038/nbt.3708

image I at coordinates (x', y'), where x', y' are bounded within $0 \leq x' \leq (w(I) - 1)$ and $0 \leq y' \leq (h(I) - 1)$. The mean, maximum, variance and kurtosis of I are denoted by $\mu(I), max(I)$, $\sigma^2(I)$, and $\gamma(I)$. The histogram of b bins between min and max of image I is denoted by $h_{b,min,max}(I)$ and is itself treated as a one-dimensional image. The L_p norm of an image I is denoted as $L_p(I)$. The discrete Fourier transform (DFT) of image I is denoted by $\mathcal{F}(I)$, the discrete cosine transform (DCT) of image I by $\mathcal{F}_c(I)$, and the Haar wavelet transform of image I by $\mathcal{W}_h(I)$. In the case of the discrete Fourier transform $\mathcal{F}(I)$ the coordinates (x, y) for $\mathcal{F}(I)_{x,y}$ are within the ranges $x \in \left[-\frac{1}{2}w(I), +\frac{1}{2}w(I)\right]$ and $y \in \left[-\frac{1}{2}h(I), +\frac{1}{2}h(I)\right]$. Applying a k by k median filter to an image I is denoted as $M_k(I)$. The notation $\left[I_{x,y+1}\right]$ represents the whole image (of unchanged width and height) translated along the y-axis by +1. A constant image can be denoted by $[1]$. In general, any expression with free variables x and y enclosed in brackets represents an image with these pixel intensities. The notation $[\![I]\!]_{x,y}^{T,X,Y}$ represents the pixel intensity at (x, y) of a T by T image tile of coordinate (X,Y). The function $d_I(x, y)$ returns the distance of the pixel (x, y) from the center of the image I. The function abslog_b is a guarded absolute logarithm of base b:

$$\mathrm{abslog}_b(\mathrm{x}) = \begin{cases} \log_b x & if\ x > 0 \\ \log_b -x & if\ x < 0 \\ 0 & if\ x = 0 \end{cases} \qquad \text{(Eq. 6)}$$

Image quality metrics and image formation

We define an image quality metric as a function f that takes an image I as argument and returns a real number. Given an image I_1, and another image I_2 that is the result of applying blur to I_1, an image quality metric should return a higher value for I_1 than for I_2. In a first-order approximation, the blur can be modeled as the convolution with a Gaussian kernel K: $I_2 = I_1 * K$. More precisely, this kernel can be approximated as the cross-section of the light-sheet microscope's point spread function (PSF) at the detection focal plane. In practice, the volumetric nature of the imaging process combined with non-defocus aberrations and scattering effects lead to a more complex relation between I_2 and I_1. The effective primary phenomenon, however, is similar to low-pass filtering of the spatial frequency content of the image. We can state the defining properties of an image quality metric as follows:

$$r < r' \Rightarrow f(I * K_r) > f(I * K_{r'}) \qquad \text{(Eq. 7)}$$

In Eq. 7, K_r and $K_{r'}$ are arbitrary non-sparse kernels of support radius r and r' respectively. These kernels can be approximated by Gaussian kernels of standard deviation σ where $r = 1.1775\ \sigma$ (assuming r is a *full width at half maximum*).

Nature Biotechnology: doi:10.1038/nbt.3708

Brightness and contrast invariance

Because of noise and possible slight variations in overall image brightness and contrast, image quality metrics should be robust enough to be invariant to affine transformations of the pixel intensities:

$$f(\alpha I) = f(I)$$
$$f(\alpha[1] + I) = f(I) \quad \text{(Eq. 8)}$$

Noise invariance

We consider microscopy images acquired by a band-limited optical system and degraded by sensor noise. It follows that any signal outside of the optical transfer function support is necessarily noise. Therefore, we also require that image quality metrics be only dependent on spatial frequencies that can pass through the optical band pass:

$$f_{r_o}\left(I * K_{r_o}\right) = f_{r_o}(I) \quad \text{(Eq. 9)}$$

In Eq. 9, K_{r_o} is a kernel with same support radius r_o as the optical transfer function. In practice we thus need to parameterize the image quality metric f with r_o to adapt to different optical configurations. In the following, f_{r_o} stands for the image quality metric f parameterized with the kernel support radius r_o.

Classes of image quality metrics

We surveyed the literature[7-9] on image quality metrics and found the following four main classes:

i) Among the oldest metrics are *Differential* image quality metrics such as Tenengrad[4] and Brenner's[6]. These measures rely on first- and second-order image finite difference schemes that respond to the sharpness of edges in the image.

ii) *Statistical* image quality metrics consider each pixel as the samples from a random variable and compute e.g. the pixel intensity histogram entropy, variance, and kurtosis to estimate the sharpness of images.

iii) *Correlative* image quality metrics such as Vollath's F4 and F5[3] rely on image auto-correlation.

iv) *Spectral* image quality metrics are based on the discrete Fourier transform[7] (DFT), discrete cosine transform[2] (DCT) and wavelet transforms[10, 11]. While the complexity of most image quality metrics is linear in image size, computing Fourier transforms and other spectral transforms are more expensive computationally – more specifically $\mathcal{O}(n \log n)$. With the advent of fast multi-core CPUs, the application of these measures for online focusing has become feasible.

Nature Biotechnology: doi:10.1038/nbt.3708

In the following, we group the different image quality metrics by class and provide mathematical details and intuition for each metric. We assume – without loss of generality – that the images I for which we compute the image quality metrics are square, i.e. $w(I)$=$h(I)$.

Differential image quality metrics

These metrics rely on the strong response of the first and second derivatives to sharp features in well-focused images. Their weakness is that the first and second derivatives of images are also very sensitive to noise. Hence, these metrics perform poorly for images with low signal-to-noise ratios. To improve comparability of these metrics to other metrics with built-in low-pass filters, we augment differential image quality metrics with a low-pass filtering preprocessing step (see paragraph "Low-pass filtering" below).

- Brenner's[6] measure:

$$B(I) \stackrel{\text{def}}{=} \frac{1}{n(I)} \sum_{x,y} \left(I_{x,y-1} - I_{x,y+1}\right)^2 \qquad \text{(Eq. 10)}$$

- Absolute Laplacian[5]:

$$AL(I) \stackrel{\text{def}}{=} \frac{1}{n(I)} \sum_{x,y} \left|2I_{x,y} - I_{x-1,y} - I_{x+1,y}\right| + \left|2I_{x,y} - I_{x,y-1} - I_{x,y+1}\right| \qquad \text{(Eq. 11)}$$

- Squared Laplacian-like:

$$SL(I) \stackrel{\text{def}}{=} \frac{1}{n(I)} \sum_{x,y} \left(8I_{x,y} - I_{x-1,y} - I_{x+1,y} - I_{x,y-1} - I_{x,y+1} - I_{x-1,y-1} - I_{x+1,y+1} - I_{x+1,y-1} - I_{x-1,y+1}\right)^2 \qquad \text{(Eq. 12)}$$

- Total Variation:

$$TV(I) \stackrel{\text{def}}{=} \frac{1}{n(I)} \sum_{x,y} \sqrt{\left(I_{x+1,y} - I_{x-1,y}\right)^2 + \left(I_{x,y+1} - I_{x,y-1}\right)^2} \qquad \text{(Eq. 13)}$$

- Block Total Variation:

$$BTV_k(I) \stackrel{\text{def}}{=} \frac{1}{n(I)} \sum_{x,y} \sqrt{\sum_{\substack{x-k \le x' \le x+k \\ y-k \le y' \le y+k}} \left(I_{x,y} - I_{x',y'}\right)^2} \qquad \text{(Eq. 14)}$$

Nature Biotechnology: doi:10.1038/nbt.3708

- Tenengrad[4] measure:

$$TG(I) \stackrel{\text{def}}{=} \frac{1}{n(I)} \sum_{x,y} \left(\mathcal{S}_h(I)_{x,y}{}^2 + \mathcal{S}_v(I)_{x,y}{}^2 \right) \quad \text{(Eq. 15)}$$

In Eq. 15, $\mathcal{S}(I)$ is the Sobel gradient filter:

$$\mathcal{S}_h(I)_{x,y} \stackrel{\text{def}}{=} I_{x+1,y-1} + 2I_{x+1,y} + I_{x+1,y+1} - I_{x-1,y-1} - 2I_{x-1,y} - I_{x-1,y+1} \quad \text{(Eq. 16)}$$

$$\mathcal{S}_v(I)_{x,y} \stackrel{\text{def}}{=} I_{x-1,y+1} + 2I_{x,y+1} + I_{x+1,y+1} - I_{x-1,y-1} - 2I_{x,y-1} - I_{x+1,y-1} \quad \text{(Eq. 17)}$$

Correlative image quality metrics

These metrics rely on the correlation between neighboring pixels. The intuition underlying these metrics is that for sharp images neighboring pixels are less correlated than for blurred images, which is a direct consequence of the low-pass filtering introduced by a defocus.

- Vollath F4 measure[3]:

$$V_4(I) \stackrel{\text{def}}{=} \frac{1}{n(I)} \sum_{x,y} I_{x,y} \left(I_{x+1,y} - I_{x+2,y} \right) \quad \text{(Eq. 18)}$$

- Vollath F5 measure[3]:

$$V_5(I) \stackrel{\text{def}}{=} \frac{1}{n(I)} \left(\sum_{x,y} I_{x,y} I_{x+1,y} - \frac{1}{n} \left(\sum_{x,y} I_{x,y} \right)^2 \right) \quad \text{(Eq. 19)}$$

- Symmetric Vollath F4 measure[3]:

$$MV_4(I) \stackrel{\text{def}}{=} \frac{1}{n(I)} \left(\begin{array}{l} \left| \sum_{x,y} I_{x,y} \left(I_{x+1,y} - I_{x+2,y} \right) \right| + \left| \sum_{x,y} I_{x,y} \left(I_{x-1,y} - I_{x-2,y} \right) \right| \\ + \left| \sum_{x,y} I_{x,y} \left(I_{x,y+1} - I_{x,y+2} \right) \right| + \left| \sum_{x,y} I_{x,y} \left(I_{x,y-1} - I_{x,y-2} \right) \right| \end{array} \right) \quad \text{(Eq. 20)}$$

Statistical image quality metrics

These metrics rely on simple statistical quantities such as mean, max, variance, kurtosis or histogram of pixel intensities. A more elaborate and novel metric is the L_p sparsity measure. By taking the ratio between the $L_{p^{-1}}$ norm and the L_p norm (of the image treated as a vector) one can measure how sparse the image is. Intuitively, an image is sparsest when it is focused.

Nature Biotechnology: doi:10.1038/nbt.3708

- Image mean intensity:

$$MEAN(I) \stackrel{\text{def}}{=} \mu(I) \quad \text{(Eq. 21)}$$

- Maximum intensity:

$$MAX(I) \stackrel{\text{def}}{=} max(I) \quad \text{(Eq. 22)}$$

- Variance:

$$VAR(I) \stackrel{\text{def}}{=} \sigma^2(I) \quad \text{(Eq. 23)}$$

- Normalized variance:

$$NVAR(I) \stackrel{\text{def}}{=} \frac{\sigma^2(I)}{\mu(I)^2} \quad \text{(Eq. 24)}$$

- Kurtosis:

$$K(I) \stackrel{\text{def}}{=} \gamma(I) \quad \text{(Eq. 25)}$$

- Difference image kurtosis:

$$DK(I) \stackrel{\text{def}}{=} \gamma\left(\left[I_{x+1,y+1} - I_{x-1,y-1}\right]\right) \quad \text{(Eq. 26)}$$

- Histogram entropy:

$$HE(I) \stackrel{\text{def}}{=} \sum_i h(I)_i \ln h(I)_i \quad \text{(Eq. 27)}$$

- L_p sparsity:

$$LPS_p(I) \stackrel{\text{def}}{=} n^{p-\frac{1}{p}} \left(\frac{L_{p-1}(I)}{L_p(I)}\right) \text{ with } p > 1 \quad \text{(Eq. 28)}$$

  A choice of $p = 2$ is sufficient to ensure a higher response for sparse images. The correction term $n^{p-\frac{1}{p}}$ makes the measure independent of image size.

Spectral image quality metrics

The fact that light microscopy images are degraded by camera readout noise and acquired by a band-limited optical system calls for image quality metrics explicitly designed to quantify all and only the information that can pass through the optical band-pass filter of the microscope. We included the following candidate transforms in our evaluation: Discrete Fourier Transform (DFT), Discrete Cosine Transform (DCT) and Discrete Wavelet Transform (DWT). The most promising transform turned out to be the Discrete Cosine Transform (DCT) in our tests, confirming the results by Kristan[2] on the Bayes Spectral Entropy. We construct several variants

Nature Biotechnology: doi:10.1038/nbt.3708

using e.g. Shannon entropy, Haar wavelet transform, L_p sparsity, and power ratio of high versus low frequencies:

- Kristan's Bayes spectral entropy[2]:

$$KBSE(I) \stackrel{\text{def}}{=} -\mu\left(1 - \frac{\left(\sum_{x+y<6} \mathcal{F}_c(\llbracket I \rrbracket^{8,X,Y})_{x,y}{}^2\right)}{\left(\sum_{x+y<6} \mathcal{F}_c(\llbracket I \rrbracket^{8,X,Y})_{x,y}\right)^2}\right) \quad \text{(Eq. 29)}$$

- Normalized DCT Bayes entropy:

$$NDCTBE_{r_o}(I) \stackrel{\text{def}}{=} 1 - \frac{\frac{{r_o}^2}{2}\left(\sum_{x+y<r_o} \mathcal{F}_c(I)_{x,y}{}^2\right)}{\left(\sum_{x+y<r_o} \mathcal{F}_c(I)_{x,y}\right)^2} \quad \text{(Eq. 30)}$$

- Generalized normalized DCT Bayes entropy:

$$GNDCTBE_{r_o,p}(I) \stackrel{\text{def}}{=} 1 - \frac{\left(\frac{{r_o}^2}{2}\right)^{p-1}\left(\sum_{x+y<r_o} \mathcal{F}_c(I)_{x,y}{}^p\right)}{\left(\sum_{x+y<r_o} \mathcal{F}_c(I)_{x,y}\right)^p} \quad \text{(Eq. 31)}$$

- Normalized DCT Shannon entropy:

$$DCTS_{r_o}(I) \stackrel{\text{def}}{=} -\frac{2}{{r_o}^2}\sum_{x+y<r_o}\left|\frac{\mathcal{F}_c(I)_{x,y}}{L_2(\mathcal{F}_c(I))}\right|\text{abslog}_2\left(\frac{\mathcal{F}_c(I)_{x,y}}{L_2(\mathcal{F}_c(I))}\right) \quad \text{(Eq. 32)}$$

- Normalized DCT Shannon entropy after 3x3 median filtering:

$$DCTSM_{r_o}(I) \stackrel{\text{def}}{=} -\frac{2}{{r_o}^2}\sum_{x+y<r_o}\left|\frac{\mathcal{F}_c(M_3(I))_{x,y}}{L_2(\mathcal{F}_c(M_3(I)))}\right|\text{abslog}_2\left(\frac{\mathcal{F}_c(M_3(I))_{x,y}}{L_2(\mathcal{F}_c(M_3(I)))}\right) \quad \text{(Eq. 33)}$$

- Normalized DFT Shannon entropy:

$$DFTS_{r_o}(I) \stackrel{\text{def}}{=} -\frac{1}{4{r_o}^2}\sum_{\substack{-r_o<x<r_o \\ -r_o<y<r_o}}\left|\frac{\mathcal{F}(I)_{x,y}}{L_2(\mathcal{F}(I))}\right|\text{abslog}_2\left(\frac{\mathcal{F}(I)_{x,y}}{L_2(\mathcal{F}(I))}\right) \quad \text{(Eq. 34)}$$

- Normalized Haar wavelet transform Shannon entropy:

$$NHWTSE_{r_o}(I) \stackrel{\text{def}}{=} -\frac{1}{{r_o}^2}\sum_{\substack{x<r_o \\ y<r_o}}\left|\frac{\mathcal{W}_h(I)_{x,y}}{L_2(\mathcal{W}_h(I))}\right|\text{abslog}_2\left(\frac{\mathcal{W}_h(I)_{x,y}}{L_2(\mathcal{W}_h(I))}\right) \quad \text{(Eq. 35)}$$

Nature Biotechnology: doi:10.1038/nbt.3708

- DCT high to low frequency ratio[7]:

$$DCTR_{r_o,r_{HL},r_{DC}}(I) \stackrel{\text{def}}{=} \frac{\sum_{-r_o<x<r_o,\,-r_o<y<r_o}\left|\mathcal{F}_c(I)_{x,y}\right|^2 - \sum_{-r_{DC}<x<r_{DC},\,-r_{DC}<y<r_{DC}}\left|\mathcal{F}_c(I)_{x,y}\right|^2}{\sum_{-r_{HL}<x<r_{HL},\,-r_{HL}<y<r_{HL}}\left|\mathcal{F}_c(I)_{x,y}\right|^2 - \sum_{-r_{DC}<x<r_{DC},\,-r_{DC}<y<r_{DC}}\left|\mathcal{F}_c(I)_{x,y}\right|^2} \quad \text{(Eq. 36)}$$

- DFT high to low frequency ratio[7]:

$$DFTR_{r_o,r_{HL},r_{DC}}(I) \stackrel{\text{def}}{=} \frac{\sum_{-r_o<x<r_o,\,-r_o<y<r_o}\left|\mathcal{F}(I)_{x,y}\right|^2 - \sum_{-r_{DC}<x<r_{DC},\,-r_{DC}<y<r_{DC}}\left|\mathcal{F}(I)_{x,y}\right|^2}{\sum_{-r_{HL}<x<r_{HL},\,-r_{HL}<y<r_{HL}}\left|\mathcal{F}(I)_{x,y}\right|^2 - \sum_{-r_{DC}<x<r_{DC},\,-r_{DC}<y<r_{DC}}\left|\mathcal{F}(I)_{x,y}\right|^2} \quad \text{(Eq. 37)}$$

- DCT L_p sparsity:

$$DCTLPS_p(I) \stackrel{\text{def}}{=} n(I)^{p-\frac{1}{p}}\left(\frac{L_{p^{-1}}(\mathcal{F}_c(I)}{L_p(\mathcal{F}_c(I))}\right) \quad \text{(Eq. 38)}$$

- Logarithmic moment of DFT spectral power:

$$LMSP_{r_o}(I) \stackrel{\text{def}}{=} \frac{1}{n(I)}\sum_{x^2+y^2<{r_o}^2}\mathcal{F}(I)_{x,y}\log(1+d_I(x,y)) \quad \text{(Eq. 39)}$$

Implementation of the DCT and DFT based spectral image quality metrics

We use the high-performance multi-threaded pure Java DCT implementation from the JTransforms[12] library. This library offers comparable performance to FFTW3[13].

Low-pass filtering

All spectral measures are parameterized with r_o, the putative support radius of the optical transfer function (OTF). If we assume – without loss of generality – a square image *I* and a laterally isotropic point spread function (PSF), the relationship between the PSF radius r_p and the OTF support radius is: $r_p = \frac{w(I)}{r_o}$.

In order to put all image quality metrics on equal footing with respect to noise handling, we add an image downscaling preprocessing step to non-spectral image quality metrics that emulates the low-pass filtering built into spectral metrics. This downscaling factor is chosen as the closest integer such that one pixel in the preprocessed image corresponds roughly to a $2r_p * 2r_p$ square patch in the original image. We observed that this simple and convolution-less preprocessing step restored the performance of most non-spectral image quality metrics in noisy data sets without adversely affecting their speed advantage over spectral measures.

Nature Biotechnology: doi:10.1038/nbt.3708

Image size invariance

To the extent mathematically feasible we normalize all measures to the number of pixels in the images. This reduces dependency of the image quality metric on image size.

Benchmark data set of synthetic focus stacks

Real light-sheet microscopy image data sets are degraded by multiple factors, such as noise, optical aberrations, and loss of contrast by light scattering. The first benchmark data set we used to evaluate the 30 image quality metrics introduced above is a synthetic data set in which the blur kernel and amount of noise are known. This data set consists of four test images: *Lenna*[14], *Barbara*, *Fingerprint* as well as *Embryo* (our own test image obtained from a RFP-histone marked fly embryo). As shown in **Supplementary Fig. 4a** these test images offer a variety of textures beyond what can typically be found in light-sheet microscopy image data. For each of the four test images we generated a synthetic defocus image sequence consisting of 100 images. The blur kernel was chosen as a plain Gaussian kernel K_r with standard deviation $r_i = |i - 50|$ for each plane i in this image stack. We generated five additional stacks by adding Gaussian noise with standard deviations 10%, 20%, 30%, 40% and 50% of the signal's average intensity (see **Supplementary Fig. 4a**). The result is a data set of 24 focus stacks with varying levels of noise (see examples in **Supplementary Fig. 4c**). Since the purpose of our first benchmark is to understand the influence of blur kernel size and noise on the various image quality metrics, we first test the image quality metrics on synthetic focus stacks generated from known standard images, Gaussian blur kernels of known standard deviation, and Gaussian noise of known level. For each focus stack and each image quality metric, we compute a focus curve (see examples on **Supplementary Fig. 4b**) and analyze its characteristics.

Quantifying error, range, noise and computational cost

For each focus curve obtained with a given image quality metric we compute the focus error, range score (R-score), density of local extrema (DLE), and computation time in nanoseconds per pixel.

The focus error is $e = |i - 50|$ where i is the index of the plane for which the image quality metric reaches its highest value. The R-score is defined by the ratio between R_{10} and R_{90} as follows: $R = \frac{R_{10}}{R_{90}}$ where R_x is the diameter of the set of values i for which $f(I_i) > \frac{x}{100} f(I_{50})$, with I_i representing the image with index i. The R-score characterizes the shape of the focus curve: it is large for image quality metrics that have a sharp tip and a wide base. The density of local extrema is the proportion of local extrema in the focus curve. A perfect focus curve unaffected by noise has only one extremum (its maximum), whereas an image quality metric affected by noise can have extrema at any location in a worst-case scenario and thus have a DLE of 1. Computing the DLE of a focus curve is a way of estimating the trustworthiness of local extrema.

Nature Biotechnology: doi:10.1038/nbt.3708

The computation time was determined in units of nanoseconds per pixel (ns/p). This measure is normalized to the number of pixels. For example 10 ns/p means roughly a 10 ms computation time for a 1000 × 1000 image. Of course this quantification ignores in a first approximation the non-linear complexity of some operations such as the DFT and DCT. Yet, these averages are sufficient and intuitive for the purpose of comparing computational efficiency on a benchmark data set.

Tuning the low-pass filter parameter

As discussed above, all image quality metrics included in this comparison either have a built-in low-pass filter parameter (for spectral metrics) or were retrofitted with a low-pass filter pre-processing step. We determined the optimal support diameter by determining the parameter r_p for which the median focus error is minimal (see **Supplementary Fig. 7**). In the case of the synthetic benchmark we determined the optimal parameter r_p to be 6 pixels (see **Supplementary Fig. 7a**).

Benchmark results for synthetic focus stacks

For each image quality metric we compute the median focus error, mean focus error, max focus error, median R-score, and median DLE. The results are shown in **Supplementary Table 1**. Mean errors range from 0.16 to 31 and most metrics achieve a median error of 0. However, only 4 measures – all based on entropy measures applied to the DCT – achieve a mean error of 0.16 and median error of 0 at the same time (units are Gaussian kernel standard deviations measured in pixels). Only 5 metrics fail to produce a median error of zero: *Mean*, *Kurtosis*, *Kurtosis of differences*, *Maximum* and *Normalized Haar wavelet transform Shannon entropy* (the worst of all evaluated image quality metrics). Considering the results on a per-class basis, we find that statistical image quality metrics perform worst, correlative and differential metrics are tied in the middle, and spectral metrics (except Haar-based) achieve the lowest mean error.

Noise is the challenge

As shown in **Supplementary Fig. 3**, the focus value response to a noiseless focus stack is remarkably accurate for almost all image quality metrics. Only a few – mostly statistical metrics – fail to produce a unimodal monotonous response: *Normalized Haar wavelet transform Shannon entropy, Kurtosis, Kurtosis of differences,* and *Shannon entropy of histogram*. It is only after adding noise that the image quality metrics start to exhibit performance differences. Image degradation due to non-defocus aberrations is not a major problem. Indeed, it is known that image quality metrics respond similarly to non-defocus and defocus aberrations[15]. This can be intuitively understood by the fact that non-defocus aberrations only lead to an increase in the support volume of the point-spread function, which in turn leads to a low-pass filter behavior.

Nature Biotechnology: doi:10.1038/nbt.3708

Canonical response

The noiseless response of the best DCT based image quality metrics shown in **Supplementary Fig. 3** suggests a simple approximate model for the image quality metric response to blur by a kernel K_r in the ideal noiseless case. In a first-order approximation one can *empirically* model the relationship between the standard deviation r of the Gaussian kernel and the normalized image quality metric value $f(I * K_r)$ with a power-tent function:

$$f_n(I * K_r) = \mathrm{T}_\alpha(r) \quad \text{with } \mathrm{T}_\alpha(r) = 1 - |r|^\alpha \text{ and } 0 < \alpha \tag{Eq. 40}$$

Note that the tent is concave for $0 < \alpha < 1$ and convex for $1 < \alpha$. The value α depends on the frequency content of the image. **Supplementary Fig. 3** shows that the focus curves for the noiseless *Fingerprint* focus stack have more pronounced concavity than the other noiseless focus stacks. Moreover, **Supplementary Fig. 4b** shows that the addition of noise also increases concavity.

The normalized image quality metric can be modeled as follows:

$$f(I * K_r) = a + b\mathrm{T}_\alpha(\sigma r) \tag{Eq. 41}$$

a, b, σ are normalization parameters. Until now we have not considered the optical parameters of the system. For a perfect lens of given numerical aperture (NA) and a given wavelength λ the relationship between the defocus distance z and the standard deviation r of the point-spread function approximated as a Gaussian kernel is:

$$r(z) = r_0 \sqrt{1 + \left(\frac{z}{z_r}\right)^2} \tag{Eq. 42}$$

In Eq. 42, $z_r = \frac{\pi {r_0}^2}{\lambda}$ is the Raleigh length of the corresponding focal volume[16], with $r_0 = \frac{\lambda}{\pi NA}$.

It follows that an approximate and partly empirically derived model for the image quality metric response to defocus by z is:

$$f(I_z) \approx a + b\mathrm{T}_\alpha\left(\sigma r_0 \sqrt{1 + \left(\frac{z}{z_r}\right)^2}\right) \tag{Eq. 43}$$

Here, $I_z = I * K_{r(z)}$. For large defocus distances z the kernel radius $r(z)$ is asymptotically linear and thus the tent function is a good approximation. For small defocus distances z the hyperbolic profile takes precedence. This smooth maximum is seen in real measured focus curves (see

Nature Biotechnology: doi:10.1038/nbt.3708

Supplementary Fig. 5c). This is in contrast to the sharp tip at the maximum of the focus curves parameterized by z instead of $r(z)$ (see **Supplementary Fig. 4b**).
The model given above for $f(I_z)$ would suggest that the image quality metric always decreases when increasing $|z|$ and thus does not admit a lower bound. However, in practice, size and bandwidth limited images cause a saturation effect: increasing the kernel radius eventually leads to a nearly constant image and thus a nearly constant response of the image quality metric. At the limit, the saturation effect leads to a finite support and asymptotically constant behavior and the hyperbolic profile induces a smooth maximum. These two effects explain why most focus curves have Gaussian-like unimodal responses.

Benchmark data set of light-sheet focus stacks

After studying the response of image quality metrics to ideal, synthetic focus stacks we turn to a more realistic and practically relevant benchmark for light-sheet microscopy. It consists of 66 focus stacks collected with a SiMView light-sheet microscope. Each focus stack is a series of n images I_z acquired at focus locations $z_i = z_{opt} + \mathrm{i}\Delta z$, with the optimal focus position z_{opt} and the step size Δz. Samples used in these imaging experiments range from fluorescent beads as well as nuclei-labeled *D. melanogaster* and *C. elegans* embryos at various developmental stages and in various orientations. Moreover, to make the benchmark data set more challenging and diverse we varied the step size Δz, number of planes per focus stack n, image size, size ratio of sample vs. field of view and the signal to noise ratio (by varying the laser power). We also added focus stacks for samples in which faint auto-fluorescence is the only visible signal.
We performed ground truth annotations for each focus stack by manually determining the plane exhibiting the best focus quality. The best focused image in a given focus stack is determined by browsing the sequence of images in forward and reverse order and visually determining the sharpest image. Such manual focusing is non-trivial and time-consuming and the procedure must be executed carefully to maximize confidence in the annotation. The procedure is furthermore inherently subjective and biased – e.g. the choice might be biased towards the regions of the image considered most relevant by the human annotator. However, despite this potential bias this approach is both valid and important, since the purpose of the manual data assessment is to determine the image quality metric that best mimics the natural focus sensitivity of human vision and all implicit criteria that contribute to the decision-making process. This analysis is thus complementary to the objective, synthetic benchmarks described above. Using the ground truth annotations, we compute focus error, R-score and DLE for all focus curves obtained by applying each image quality metric to each focus stack.

Benchmark results for light-sheet focus stacks

As shown in **Supplementary Fig. 7b**, we determined the optimal diameter of the low-pass filter to be 3 pixels, i.e. the optimal value of r_p is 1.5 (see **Supplementary Table 2**). The value of 3 pixels is expected for our optical configuration, since the theoretical PSF associated with our 16×/0.8 NA detection objectives covers a 3×3 pixel region on the detector, i.e. PSF support is

Nature Biotechnology: doi:10.1038/nbt.3708

effectively 3×3 pixels. This optimal value is expected to be different for detection systems with significantly different NA and/or magnification, and for detectors with a significantly different pixel size. The benchmark results are shown in **Supplementary Table 3**. Only 4 metrics achieve a median error of zero: all of these are based on entropy measures applied to the DCT and they furthermore match the four best-performing metrics determined in the synthetic benchmarks. Differential metrics, which are augmented with low-pass filtering ($r_p = 3$) like all other non-spectral metrics, follow with median focus errors between 250 and 810 nm. Correlative metrics perform similar to differential metrics, with the exception of Vollath's F5 (median focus error of 1.63 μm). Statistical metrics perform worse, with a median focus error of 10 μm for the worst metric (Shannon entropy of pixel intensity histogram).

The best image quality metrics for light-sheet microscopy

The four best image quality metrics perform almost identically – the dominant component being the DCT. Yet, the very best image quality metric is the *Normalized DCT Shannon entropy* (DCTS) with a mean error of 320 nm and the highest R-Score among the four best measures. It has a higher median DLE but this does not affect its accuracy. We choose DCTS as our image quality metric because it is the second fastest (27 ns/p on average) and has the highest range score (7.35) which yields a better tradeoff between maximum sharpness and broad side tails of the focus curve. The four best measures have mean errors below or equal to 330 nm, which is close to half of the emission wavelengths of GFP (515 nm) and RFP (600 nm) but well below the detection system's depth of focus of 1.75 μm (using a Nikon 16x/0.8 objective and a Hamamatsu Orca Flash 4.0 camera with pixel pitch of 6.5 μm). With such high accuracy in some of the most difficult, real image data sets (see three particularly challenging examples in **Supplementary Fig. 6**) the image-based assessment of optimal focus settings in light-sheet microscopy can effectively be considered a solved problem. In practice, the human observer needs time and experience to resolve sharpness differences at a focus distance of about 1 μm from the optimal focus, which can already be sufficient to compromise our ability to delineate boundaries between neighboring cell nuclei, as shown in the first example presented in **Supplementary Fig. 6** (see blue arrow highlighting one such boundary between two neighboring cell nuclei).

Why do DCT-based measures perform so well?

Our benchmark shows that the single most important factor for achieving high accuracy is the use of a DCT as frequency domain transform. The DCT is known as one of the best transforms for signal compression purposes, compared to the DFT or other related transforms (Hartley, SLT, Walsh, Haar). The DCT (and more precisely, the DCT-2) can accurately encode an image with fewer coefficients than the DFT[17], while producing less ringing. This is in part a consequence of the DCT being the most energy-compact transform after the signal-dependent Karhunen-Loève transform (KLT)[18]. Our first intuition that the DCT could be used for focusing came from anecdotal evidence using digital cameras: when taking multiple shots of the same scene under low light conditions the sharpest picture (least shaking of the camera's detector) can be reliably

Nature Biotechnology: doi:10.1038/nbt.3708

recognized as the largest JPEG-encoded file. Indeed, the JPEG format uses the DCT as its primary transform followed by an entropy-encoding compression scheme. This intuition was further confirmed when consulting the work by Kristan on the Bayes Spectral Entropy[2]. In general, compression-based methods for measuring data quality have shown their success in other fields[19]. Our synthetic focus stack benchmark results revealed that achieving insensitivity to noise is the main challenge. Since the DCT concentrates most of the signal energy in the low frequency components, the low-pass filtering intrinsic to the definition of the DCTS and other DCT-based image quality metrics becomes especially effective at separating noise from signal.

Computational cost

The cost of accuracy is computation time: the computational cost for DCTS is on average 27 nanoseconds per pixel across the entire benchmark data set, which is almost 6 times slower than the best non-spectral metric (Tenengrad) with median and mean errors of just 250 and 610 nm, respectively. In more time-constrained scenarios the Tenengrad measure thus offers a reasonable tradeoff between accuracy and speed.

Structured illumination focusing

For samples with difficult (featureless) texture of the fluorescent signal or when photo-bleaching and photo-toxicity must be kept to a minimum, we implemented an option to use a digitally modulated structured light sheet[20] to artificially introduce high-frequency modulation in the optical section. In the same manner that structured light sheets can improve the optical sectioning ability of a light sheet microscope, structured light sheets can also improve the response of an image quality metric. The spatial modulation frequency must be chosen as high as the optical transfer function of the microscope allows. When acquiring a focus stack, we maintain the same phase for all images and reduce the laser power to a level that still allows good focusing.
The optimal modulation period can be automatically determined by performing a systematic, sampled search of e.g. ten periods within a predefined interval $[p_{min}, p_{max}]$. Selecting the period yielding the highest DCTS value is a good heuristic for this purpose.

Adjusting laser power

The DCT spectrum can be leveraged to estimate the signal-to-noise ratio in an image. Intuitively, an image composed exclusively of noise has a random DCT spectrum with uniformly distributed energy over all frequencies. In the presence of signal, computing the power ratio of signal versus noise provides a way of estimating the signal to noise ratio. This can be achieved by estimating the noise baseline power outside of the microscope's transmitted frequency band and thus estimating the ratio of signal to noise within the band pass (the baseline is the same). The laser power can be adjusted to the lowest level that satisfies a certain minimal observed SNR ratio.

Nature Biotechnology: doi:10.1038/nbt.3708

Part III | Special Optimization Theory for Spatiotemporally Adaptive Imaging

We showed in Part II above that the DCTS image quality metric and other DCT based metrics are the best-performing image quality metrics for light-sheet microscopy. Equipped with these metrics we can in principle adjust and evaluate each alignment parameter of the microscope in isolation to optimize image quality. However, in a complex multi-view light sheet microscope with multiple detection and illumination arms, all relevant parameters are interdependent. In the following we explain the mathematical theory behind our optimization approach. For simplicity and exposition clarity we first restrict ourselves to a local optimization approach for a light-sheet microscope comprising up to two illumination and two detection arms (SiMView microscope layout[21]) and consider only system parameters corresponding to the translation of detection focus and light sheet planes. In Part IV, we extend this theory further to a general optimization theory that considers measurements at all reference planes simultaneously. For simplicity, we omit the advanced degrees of freedom of the adaptive imaging framework (Y, α, β) in Part III.

The microscope's state variables

The SiMView microscope layout consists of two coaxial detection arms and two coaxial illumination arms in an orthogonal configuration. The state variables relevant for focusing are the positions of the two detection planes, denoted D_1 and D_2, and the positions of the two light sheets along the detection axis, denoted I_1 and I_2. These four state variable constitute the state vector of the system:

$$S = \begin{pmatrix} D_1 \\ D_2 \\ I_1 \\ I_2 \end{pmatrix} \qquad \text{(Eq. 44)}$$

The two detection arms image light emitted by the specimen onto two cameras C_1 and C_2. For each camera C_u there are two different images that can be formed by illuminating the sample using either the first or second illumination arms. Therefore, for each combination of illumination and detection arm (I_u, D_v) the microscope can produce an image that is more or less focused depending on the values of I_u and D_v. These variables are directly controllable by the microscope's electronics and software framework and have arbitrary undefined zero positions that cannot be assumed to correspond to a focused state.

Manual focusing

Manual focusing of a four-arm light-sheet microscope would consist of e.g. fixing the D_1 variable and then adjusting I_1 and I_2 independently. Finally, variable D_2 can be set to two *a priori* different values based on the previously determined values I_1 and I_2. In order to reconcile these two values, one can simply take the average (if imaging eventually needs to be performed

Nature Biotechnology: doi:10.1038/nbt.3708

with both light sheets simultaneously). Other orders are possible, for example: fix I_1 first, then determine D_1 and D_2, and finally find a compromise for I_2. This naïve sequential approach has several shortcomings: (i) The only constraint that can be defined is the fixing of a variable, (ii) there is no guarantee that the overall system corrections are minimal, and (iii) the scheme is inherently progressive and as such it is not possible to take all necessary measurements before changing the state of the system. In the following, we show how these shortcomings are addressed in our focus optimization theory.

Focus matrix

Focusing depends on the distance between each detection plane and each illumination plane. We can compute these distances with the following matrix:

$$M = \begin{pmatrix} +1 & 0 & -1 & 0 \\ +1 & 0 & 0 & +1 \\ 0 & +1 & +1 & 0 \\ 0 & +1 & 0 & -1 \end{pmatrix} \quad \text{(Eq. 45)}$$

The signs of the entries depend on the orientations of the axes (see **Supplementary Fig. 8a**). In practice, it is possible that different units are used for D_1, D_2, I_1 and I_2. If this is the case, a single unit is chosen and some entries in matrix M will have values that differ from +1 or –1. Moreover, variables D_1, D_2, I_1 and I_2 have *a priori* undefined zero positions because they directly translate into actuator (e.g. piezo positioner or galvanometer scanner) commands. It follows that the distances computed by M also have undefined offsets – a physical zero distance does not necessarily correspond to a numerical zero. We will discuss below how the formalism can handle these under-determinacies. In fact, the primary purpose of the following theory is to be able to reason about the focused state of the microscope in the absence of prior system calibration.

Focus state

The matrix M computes from the state vector S the focus state vector F:

$$\begin{pmatrix} F_{1,1} \\ F_{1,2} \\ F_{2,1} \\ F_{2,2} \end{pmatrix} = F = MS \quad \text{(Eq. 46)}$$

Since the matrix M is rank-deficient of rank 3, it follows that different system states S correspond to the same focus state F. Intuitively, this can be understood by noting the focusing invariance when translating all planes in the same physical direction by the same amount. Formally, the system state S can be translated by any vector K in the kernel $Ker(M)$ of M:

$$F = M(S + K) \quad \text{(Eq. 47)}$$

Nature Biotechnology: doi:10.1038/nbt.3708

In the case of the multi-view microscope described here the kernel can be generated as follows:

$$Ker(M) = \left\{ k \begin{pmatrix} 1 \\ -1 \\ 1 \\ -1 \end{pmatrix} \middle| k \epsilon \mathbb{R} \right\} \quad \text{(Eq. 48)}$$

In practice, since the state variables have limited ranges, the range of k is also limited.

Focusing by pseudo-inverting the focus matrix

Focusing the system means finding the optimal focus vector F such that all detection and illumination planes coincide. Each component $F_{u,v}$ of vector F is related to an image $J_{u,v}$ acquired with detector D_u, from which a focus value $f(J_{u,v})$ can be computed. Hence for each focus state F we can compute the following vector (by acquiring images and computing the focus value of each image):

$$\begin{pmatrix} \varphi_{1,1} \\ \varphi_{1,2} \\ \varphi_{2,1} \\ \varphi_{2,2} \end{pmatrix} = \varphi = \begin{pmatrix} f(J_{1,1}) \\ f(J_{1,2}) \\ f(J_{2,1}) \\ f(J_{2,2}) \end{pmatrix} \quad \text{(Eq. 49)}$$

For simplicity, we write $\varphi = f(F)$. The search for the optimum is achieved by independently varying each component $F_{u,v}$ of vector F until the maximum of each $\varphi_{u,v}$ is attained. Each $F_{u,v}$ can be varied by changing the position of the corresponding detection plane D_u or I_v (see first two columns of focus matrix M). However, in practice it is better to maintain the light sheets stationary in order to improve the comparability of the acquired images. We thus vary $F_{u,v}$ by varying D_u. Corrections determined by varying D_u instead or I_v are valid for small displacements because we assume locality and continuity of corrections. Considering that we start from an *a priori* unfocussed focus state F and find by this method a new better focus state F', we have:

$$\Delta F = F - F' = M(S - S') = M\Delta S \quad \text{(Eq. 50)}$$

ΔF is the correction vector to the current focus state that achieves the highest focus quality and ΔS is the equivalent correction vector of the system state. Determining the system correction ΔS based on the focus state corrections ΔF requires to pseudo-invert the focus matrix M.

Nature Biotechnology: doi:10.1038/nbt.3708

The Moore-Penrose pseudo-inverse[22] of M is:

$$M^{+} = \frac{1}{8}\begin{pmatrix} +3 & +3 & +1 & +1 \\ +1 & +1 & +3 & +3 \\ -3 & +1 & +3 & -1 \\ -1 & +3 & +1 & -3 \end{pmatrix} \quad \text{(Eq. 51)}$$

The Moore-Penrose pseudo inverse returns the minimal L_2 norm solution ΔS of the system $\Delta F = M\Delta S$ for a given ΔF:

$$\Delta S = M^{+}\Delta F \quad \text{(Eq. 52)}$$

The system can then be moved to a better-focused state S' by applying: $S' = S + \Delta S$. This formalism guarantees that the correction is mathematically well-defined. This addresses point (i) mentioned above in our discussion of manual focusing. Furthermore, we will see below that we can easily find solutions that satisfy other constraints and meet other minimization goals.

Constraining solutions

In order to guarantee that the system does not drift over time, one can anchor the system by requiring one of the system's variables D_1, D_2, I_1, or I_2 to be fixed. This can be achieved by adding to ΔS an appropriately chosen vector $\Delta K \in Ker(M)$ such that the chosen component of ΔS becomes zero. Since ΔK belongs to $Ker(M)$ this new correction is still a solution to the system $\Delta F = M\Delta S$. This is similar to what could be achieved using the naïve manual approach. However, we can also decide to maintain a fixed center of mass of the system instead. Since all degrees of freedom considered here are along the same axis, and since the kernel $Ker(M)$ is of rank one, it follows that the center of mass can be parameterized by a single dimension obtained with the following product:

$$c = \begin{pmatrix} 1 \\ -1 \\ 1 \\ -1 \end{pmatrix}^{\mathrm{T}} S \quad \text{(Eq. 53)}$$

The alternating signs originate from the different axis orientations of D_1, D_2, I_1, and I_2 (see **Supplementary Fig. 6a**). One can then adjust the correction ΔS by adding a $\Delta K \in Ker(M)$ such that the center of mass of the system remains invariant. This capability addresses point (ii) mentioned previously when discussing manual focusing.

Nature Biotechnology: doi:10.1038/nbt.3708

Focusing reduced systems

In those cases where only one detection arm and/or one illumination arm is needed, the corrections ΔS can be found by first setting the corresponding components of the focus correction vector ΔF to zero and computing the state corrections ΔS.

Fast and robust search for the optimal ΔF

We have seen that ΔS can be determined from ΔF and that ΔF is found by searching for the $F'_{u,v}$ that maximize the corresponding $\varphi'_{u,v}$. In practice we find the optima $F'_{u,v}$ that maximize $\varphi'_{u,v}$ by sampling m values of $F'_{u,v}$ around the initial values $F_{u,v}$:

$$F^k_{u,v} = F_{u,v} + \left(\frac{2k - m + 1}{m - 1}\right) r \qquad \text{(Eq. 54)}$$

r is the search radius and $k \in [0, \dots, m-1]$. In practice, it is useful to pick an odd number of samples m so that $\frac{2k-m+1}{m-1}$ can be zero, thus offering the possibility of no correction to the system. The optima $F'_{u,v}$ are then:

$$F'_{u,v} = \underset{F^k_{u,v}}{\operatorname{argmax}} \varphi^k_{u,v} \qquad \text{(Eq. 55)}$$

$\varphi^k_{u,v} = f(J^k_{u,v})$ and $J^k_{u,v}$ is the image acquired on detector u using light sheet v. This simple ordered and batched sequential approach is faster than performing Fibonacci search, Golden section search or Brent's method because of the preferred modes of operation of the microscope's hardware and electronics: The camera and low-level control electronics perform much faster when instructed to acquire a deterministic, predefined sequence of images, and mechanical considerations require sequentially ordered commands. To improve robustness for low numbers of samples ($m \leq 10$) we normalize the focus values:

$$\hat{\varphi}^k_{u,v}. = \frac{\varphi^k_{u,v} - \varphi^{min}_{u,v}}{\varphi^{max}_{u,v} - \varphi^{min}_{u,v}} \qquad \text{(Eq. 56)}$$

Here, $\varphi^{min}_{u,v} = \min_k \varphi^k_{u,v}$ and $\varphi^{max}_{u,v} = \max_k \varphi^k_{u,v}$. We then apply a standard Gaussian fit or our more robust *argmax* algorithm to find $F'_{u,v}$.

Gaussian fit

Computing the argmax given k points of $\varphi^k_{u,v} = f(J^k_{u,v})$ is a trivial problem. The simplest approach is to fit a Gaussian curve $\phi_k = \alpha e^{-\frac{(k-\mu)^2}{\sigma^2}}$ by optimizing the choice of α, μ, and σ by means of the Levenberg–Marquardt algorithm[23]. As discussed above, this Gaussian prior was

Nature Biotechnology: doi:10.1038/nbt.3708

found empirically to be a good model for the shape of the focus curve. Polynomial models are plagued by their natural tendency to oscillate and other Gaussian-like distributions such as Lorentz-Cauchy or Voigt do not perform well in practice and do not contribute anything more than added complexity. We use the MINPACK based implementation in the *Apache Commons Math* library (*https://commons.apache.org/proper/commons-math*) with an initial step bound factor of 100, a cost relative tolerance of 10^{-10}, a parameters relative tolerance of 10^{-10}, and an orthogonality tolerance of 10^{-10}. The optima $F'_{u,v}$ are then obtained by the following formula:

$$F'_{u,v} = F_{u,v} + \left(\frac{2\mu_{u,v} - m + 1}{m - 1}\right) r \qquad \text{(Eq. 57)}$$

While this approach performs well in many cases, we also observed that it can lack robustness in imaging scenarios suffering from a low signal-to-noise ratio.

Robust argmax algorithm

We need to consider that argmax potentially has to be computed thousands of times during a time-lapse imaging experiment. In cases when the signal-to-noise ratio of the images is very low such as for pan-neural marker expression onset, this leads to noisy focus measurements $\varphi^k_{u,v}$, which in turn leads to noisy $F'_{u,v}$ values that ultimately degrade the overall stability of the system. To address this problem we developed a robust argmax fitter algorithm that uses an ensemble approach.

Any straight-forward approach to fitting a curve to data points $\varphi^k_{u,v} = f(J^k_{u,v})$ and for finding the argmax is vulnerable to certain conditions. For example, Gaussian curve fitting works well with symmetric unimodal curves but is generally unsuited if the response is biased and asymmetric (non-null skewness). In this case, a 3rd or 4th order polynomial might be a better choice, but polynomials are notoriously bad interpolants that have a natural tendency to over-fit and catastrophically oscillate, especially in the presence of noise. Better approaches are e.g. spline interpolation or Loess filtering approaches, but again, there will be cases in which these fail, too. Our solution is to estimate the argmax by leveraging many different approaches simultaneously. In the following we assume that we search for the argmax of $y = f(x)$. We compute the following 11 estimates in parallel:

1. *Three point quadratic fit:* This algorithm takes just three points (min, average, and max for *x*) and fits a single parabola.
2. *Levenberg–Marquardt quadratic fit:* This algorithm fits all the points to a parabola and returns the parabola's extremum location.
3. *Levenberg–Marquardt Gaussian fit:* This algorithm fits all the points to a Gaussian and returns the Gaussian's mean.
4. *Levenberg–Marquardt quartic fit:* This algorithm fits all the points to a quartic and returns its argmax.

Nature Biotechnology: doi:10.1038/nbt.3708

5. *Spline fit:* We fit an unclamped spline to the data and determine the argmax empirically by high-resolution sampling.
6. *Random spline fit:* We select random subsets of the data, fit splines to each, and compute the median argmax across all data subsets. The objective is to achieve robustness against outliers.
7. *Loess fit:* We fit the data using the Local Regression Algorithm (Loess) and compute the argmax empirically by high-resolution resampling.
8. *Top 5 quadratic fit:* We select the 5 data points (x, y) of highest y value and fit a parabola. We return the extremum location.
9. *Center-of-mass argmax:* We compute the center of mass of the data points interpreted as a distribution.
10. *Mode:* We compute the mode of the data points interpreted as a distribution (x value for highest y value)
11. *Median:* We compute the median of the data points interpreted as a distribution.

All these rather simple algorithms run simultaneously on different processor threads and computing the median estimate combines their results into one robust estimate. It is highly unlikely that all or even many of the above argmax estimators will fail or give biased results for the same data sets. Overall, the median of all estimates gives us a more robust estimate of the ideal argmax value. For more details on this approach, please consult the *AutoPilot* source code repository.

The capability to estimate the correct argmax value even in the presence of strong noise is important. However, knowing when to 'give up' is even more important. As we will explain in more detail, knowing when a piece of information is unreliable gives us the chance to replace this information with an estimate derived from reliable, complementary measurements. We explain below how to decide when an argmax computation is reliable or not.

Estimating the probability that an argmax fit did not just occur by chance

In the worst-case scenario, we are attempting to adjust the microscope for a region of the sample devoid of significant fluorescence signal. This leads to a sequence of dark images $J_{u,v}^k$ dominated by noise and thus to a random sequence of $\varphi_{u,v}^k$ values. Most of the time, setting a threshold on the $\max_{F_{u,v}^k}(\varphi_{u,v}^k)$ will be sufficient to detect such cases and mark these measurements as unreliable. However, it is often necessary to adjust these thresholds for different types of experiments. In our experience, it is better to instead use a conservatively low DCTS threshold that excludes measurements that derive with high certainty from low quality images. Unfortunately, this leaves many borderline cases for which some signal is present but not enough to make a reliable argmax estimate. Another complementary approach is to set a threshold on the root mean square deviation (RMSD) of the data to a Gaussian fit. However, there is a fundamental difficulty in

Nature Biotechnology: doi:10.1038/nbt.3708

deciding on a threshold for the RMSD – this can be done empirically but with few guarantees. Overall, it would certainly be better if no such thresholds were needed in the first place. To solve this problem we compute the RMSD of the fit to the data. We then compute the RMSD values obtained by fitting Gaussians to hundred instances of the same data *randomized* by permutation of the $\varphi_{u,v}^{k}$ values. This allows us to make an estimate of the probability that the observed RMSD is due to chance alone. Intuitively, if the data is already random, it will be statistically undistinguishable after random permutation. However, if the data is not random – i.e. it has a unimodal Gaussian-like shape – then after permutation it will lose its structure and the fit error will be drastically different. Formally, from the point of view of classical statistical hypothesis testing, our null hypothesis is that the data is random. By random permutation we compute empirically the probability distribution of the RMSD under the null hypothesis – which allows us to compute the corresponding p-value. The p-value (p_v) is the probability of an event at least as extreme as the event we are considering (a given RMSD for true non-randomized data), assuming the truth of the *null hypothesis*. We now can apply a threshold not on an arbitrary quantity (RMSD) but on an actual probability: $1 - p_v$ which is usually well above 0.99 for good fits and can easily fall below 0.5 for highly noisy curves. In practice we choose thresholds such as 0.99 which have a well-defined interpretation: we reject measurements that have a > 1% probability of being 'hallucinated' from noisy data.

Iterative initial focusing

Before starting long term imaging sessions an initial focusing step is required. Since the optima $F'_{u,v}$ are *a priori* far from the current value $F_{u,v}$, we would have to set r and m to large values (typically $r = 60$ µm and $m = 121$) to achieve an expected error of 0.5 µm. This would be far too wasteful with respect to the available photon budget and might affect the physiology of e.g. early-stage embryos that are quite sensitive to light exposure. Instead, we use an iterative approach that incrementally narrows the search space. We typically set $m = 11$ and apply the entire focusing procedure with radii from $r = 60$ µm to $r = 3$ µm in s steps, typically using $s = 3$. This achieves a higher expected accuracy of ~ 0.25 µm (which is realizable in practice considering the benchmark performance of DCTS) for a total of only 33 samples (75% reduction of measurements).

Spatial adaptive focusing

In the absence of aberrations introduced by the sample or the embedding medium, one can assume that the determined focused state S remains valid at different depths in the specimen. However, we observed that in most specimens, such as entire fruit fly or zebrafish embryos, different corrections are required for optimal image quality at different imaging depths. To address this variability we determine the best system state at several imaging planes: $z_0, \ldots, z_{n-1}$ (for e.g. $n = 8$ see **Supplementary Fig. 8b**), store the corresponding optimal states: $S_0, \ldots, S_{n-1}$ and linearly interpolate in between and linearly extrapolate outside to obtain a state S_z at an

Nature Biotechnology: doi:10.1038/nbt.3708

arbitrary imaging depth z. We note that for not entirely transparent specimens, each detection arm can typically acquire high-quality image data only for about half of the specimen (the half the objective is facing, **Supplementary Fig. 8b**) – the respective other detection arm will generally provide better image quality for the other half of the specimen, owing to the shorter detection path length. With this in mind, let the centermost focusing planes be z_s and z_{s-1} (e.g. see **Supplementary Fig. 8b**, where $s = 4$). It follows that determining optimal states $S_{k \leq s-1}$ for the first half of the sample should only involve variables D_1, I_1 and I_2, whereas determining optimal states $S_{k \geq s}$ in the second half of the sample ($z > 0$) should only involve variables D_2, I_1 and I_2. Determining optimal state S_k for each plane z_k independently would not ensure continuity of the imaged volume in the presence of relative drifts between variables D_1 and D_2. Spatial continuity is ensured for the first half by maintaining D_1 in a fixed position and for the second half by maintaining D_2 in a fixed position. Fixing D_1 and D_2 is usually a better choice than fixing I_1 or I_2, in particular when using highly accurate piezo positioners for moving the detection objectives (in contrast to the less accurate galvanometer scanners or tip-tilt mirrors responsible for moving the light sheets). We establish a continuous and well-defined link between the two halves by carrying over light sheet positions I_1 and I_2 at plane z_{s-1} to plane z_s and by solving the system at plane z_s for D_2 by fixing both I_1 and I_2. This ensures seamless spatial continuity of the whole specimen volume.

Temporal adaptive refocusing

During long-term imaging of e.g. developing embryos, which can take up to several days, imaging quality is usually at the mercy of thermal, mechanical and electronic drifts as well as optical changes introduced by the specimen's own development. To guarantee optimal focusing throughout time-lapse experiments we thus need to be able to adjust S^z at successive time points. The system state variable $S^{t,z}$ becomes a function of time (t) and depth (z). Performing an entire refocusing sequence involving e.g. 8 reference planes typically requires on the order of 80 image acquisitions. Given an average computational cost of 240 ms per image (including acquisition and processing), refocusing the whole system would require approximately 19 seconds, which may not be acceptable depending on the available time budget. For example, when imaging *Drosophila* embryonic development for the purpose of cell tracking we would typically aim for a temporal resolution of 30 seconds in order to ensure that cells do not move by more than half a cell diameter from one time point to the next. When using motorized stages to move the specimen for volumetric imaging in this scenario[21], there may not be more than 5 seconds of idle time (i.e. time not spent on primary image acquisition) between time points that can be utilized for AutoPilot measurements. The solution to this problem is to distribute the measurements required for refocusing over multiple time points. Our quanta of observation – the measurement that cannot practically be broken into smaller measurements – is the measurement of $\varphi_{u,v}^k$ for a given wavelength and depth. From previous work[24] we know that the acquisition duty cycle is often up to 90%. This gives us less than 10% of time available to perform image quality measurements. For typical acquisition settings in developmental time-lapse imaging, this

Nature Biotechnology: doi:10.1038/nbt.3708

translates to a time budget of 3 to 6 seconds between two time points available to acquire m images, compute the image quality metrics and determine the optimum parameter setting. Once all information is available to correct the system state at depth z, a new value $S^{t+1,z}$ is computed, thus updating the previous value $S^{t,z}$. **Supplementary Fig. 8c** shows the experiment timeline and illustrates how image quality measurements can conceptually be distributed in time. We note that in the case of high-speed functional imaging[25] it is typically not possible to perform image quality measurements without impacting the temporal resolution of the imaging experiment (simply because one would often run the acquisition at the maximum imaging speed the microscope is capable of, thus leaving no time for image quality measurements). However, these types of recordings are usually so short that they only require initial focusing and do not benefit significantly from temporal refocusing.

Robust and fast recovery from system perturbations

In addition to handling sample-induced image perturbations, an automated microscope for adaptive imaging must also be able to quickly recover from system-induced image perturbations. In order to systematically test the capabilities of our framework to this end, we induced external perturbations while recording a 4-hour time-lapse of germ band retraction and dorsal closure in a nuclear labeled (His2Av-RFP) *Drosophila melanogaster* embryo (**Supplementary Video 1**). During this experiment, we manually shifted (at the hardware level) the zero offsets of piezo actuators defining detection objective positions and tip/tilt mirrors defining light sheet offsets. Importantly, the computational framework is unaware of the execution, timing and magnitude of these perturbations since the perturbations were manually induced downstream of the software and electronics layers (by adjusting baseline voltages through the respective knobs on the analog controllers).

A complete four-view 3D image data set of the *Drosophila* embryo (comprising 515×1186×111 voxels per image stack) was acquired once every 30 seconds. Every 4 minutes a full correction cycle for 4 uniformly spaced reference planes was completed. Depending on when perturbations occurred relative to the phase of the correction cycle, single planes and views could be corrected within as little as 30 seconds. To ensure that the whole system does not drift with respect to the sample over time, we locked the position of the first detection objective (D_1) and allowed corrections only to the other degrees of freedom. We triggered 9 different types of perturbations, each involving a subset of the four main degrees of freedom of the microscope: the positions of the two detection objectives (D_1 and D_2) and the offsets of the two light sheets (I_1 and I_2). **Supplementary Fig. 10a** provides an overview of the 9 perturbations, including the corresponding degrees of freedom affected by each perturbation and the amplitude of the perturbation. Perturbations #1 to #6 are instantaneous changes of individual degrees of freedom (D_1, D_2, I_1, I_2) and pairs of degrees of freedom (D_1 and D_2, I_1 and I_2). Perturbations #7 and #8 are two slow ramps (misaligning the system at a rate of 1 µm/min), involving first I_2 and then D_1. The final perturbation #9 is a strong (8 µm) instantaneous change of I_2 and D_1 simultaneously that brings the system back to the initial baseline configuration prior to perturbation #1. This last

Nature Biotechnology: doi:10.1038/nbt.3708

perturbation is so strong that it is very unlikely to occur in a 'normal experiment' performed with the biological specimen alone. However, we included this test as well in order to seriously challenge the system and evaluate its robustness under extreme conditions.
In order to monitor the quality of the image data recorded by the microscope, we compute for each acquired volume a volumetric quality metric based on our best performing focus metric (DCTS, see **Supplementary Methods 2**). **Supplementary Fig. 10a** shows that embryonic development leads to a positive longitudinal trend in the volumetric focus quality metric, which is due to the increase in nuclei density and the corresponding increase in fine details and high frequency textures in the imaging volume over time. More importantly, this visualization also shows how each perturbation leads to a temporary dip in the volumetric focus quality metric. **Supplementary Fig. 10b** shows the changes automatically applied by the system to the four degrees of freedom at reference plane z_3. We intentionally selected reference plane z_3 for this demonstration because images at this plane are linked to the unconstrained degree of freedom D_2 (which makes the data readout at this location particularly useful for evaluating system robustness). Panels (c), (d) and (e) in **Supplementary Fig. 10** show how image quality at plane z_3 is affected by three example perturbations #4, #5 and #9. As shown in panel (a), perturbation #4 leads to a very small dip in the volumetric image quality metric, which is further confirmed by the almost imperceptible degradation of image quality following the perturbation shown in **Supplementary Fig. 10c**. Perturbation #5 involves both detection objectives and is fully compensated at plane z_3 within 2 time points (1 minute) and throughout the entire volume within 10 time points (a period close to the length of the full-system correction cycle (see **Supplementary Fig. 10a**). In contrast, the exceptionally strong perturbation #9 (amplitude: 8 μm) requires two full correction cycles to be fully corrected throughout the specimen volume. As shown in **Supplementary Fig. 10a,e** and **Supplementary Video 1** our system is capable of successfully recovering even under extreme conditions, such as when confronted with strong external perturbations of its properly focused state. Notably, during this same test experiment the system also successfully handled sample-induced perturbations by following and adjusting to the development of the live embryo. We conclude that if our system succeeds under these extreme conditions it will likely maintain optimal image quality also under the normal, slow and progressive drifts occurring in time-lapse imaging of living organisms.

On-demand spatio-temporal focusing

The expression of fluorescent markers is not necessarily constant in space or time, e.g. when imaging fluorescently tagged transcription factors or individually labeled populations of cells that move within the developing embryo. Thus, there is not always enough fluorescent signal (i.e. information) at a given time t and reference plane z_k to determine the best system state $S^{t,z}$. A spatio-temporal adaptive microscope has to be robust to lack of signal either in time or space. Despite the high sensitivity of the DCTS image quality metric (see **Supplementary Fig. 4c** and **Supplementary Fig. 6c**), focusing in the absence of a sufficient amount of fluorescent signal introduces the risk of system oscillations due to noise. To address this challenge, we

Nature Biotechnology: doi:10.1038/nbt.3708

experimented with two strategies to decide whether a plane is devoid of signal: (i) we set an absolute focus value threshold f_{min}, and (ii) we set an upper-bound for the error of the Gaussian fit. If, based on this definition, we find that a reference plane z_k is *empty* the new state S'_k is set to the average $S_k^{t+1} = \frac{1}{3}(S_{k-1}^t + S_k^t + S_{k+1}^t)$, where S_{k-1}^t and S_{k+1}^t are the previously determined focused states from neighboring planes (if $k-1<0$ or $k+1>n-1$ then S_k^t is used instead). It follows that reference planes that do not provide enough fluorescent signal will follow the behavior of their neighboring planes until the local signal becomes strong enough to determine a better local optimum.

Drift correction

A common sample preparation strategy in light-sheet microscopy is based on sample embedding in low-density agarose gels. These gels offer excellent imaging quality but they can also introduce a tendency of sample drift in long-term imaging sessions. In extreme cases, these drifts can jeopardize the recording itself if parts of the specimen move outside of the imaged volume. In addition, the position of the planes z_k relative to the embryo may change because of these drifts, which can in principle affect the quality of the spatio-temporal focusing. To address this problem we implemented three-dimensional specimen tracking techniques that maintain the specimen stationary within the imaged volume.

Nature Biotechnology: doi:10.1038/nbt.3708

Part IV | General Optimization Theory for Spatiotemporally Adaptive Imaging

The basis of the general optimization theory for spatiotemporally adaptive imaging is the realization that the inverse problem formulated in the basis of the focus matrix M can be extended so that a single potentially large linear inversion problem can represent all observations, linear parameter relationships and constraints pertaining to all degrees of freedom for all reference z-planes and all colors. The optimization is performed simultaneously for all degrees of freedom, thus reducing the propagation of noise from individual observations. This makes it possible to accurately compensate for chromatic aberrations in multi-color imaging and to introduce sophisticated parameter anchoring and bridging schemes.

The microscope's state variables

In the following we assume – without loss of generality – that spatiotemporally adaptive imaging is performed for a multi-view light-sheet microscope comprising two detection arms and two illumination arms. The microscope's state vector now contains the values for all degrees of freedom for all reference planes and all color channels:

$$F = \begin{pmatrix} D_1 \\ D_2 \\ I_1 \\ I_2 \\ Y_1 \\ Y_2 \\ \alpha_1 \\ \alpha_2 \\ \beta_1 \\ \beta_2 \\ \\ \dots \end{pmatrix} \qquad \text{(Eq. 58)}$$

The degrees of freedom D_1, D_2, I_1, I_2 are the same variables previously described. The new state variables Y_1, Y_2 correspond to the translation of light sheets along their respective illumination axes, and α_1, α_2, and β_1, β_2 correspond to the two angular degrees of freedom of each light sheet (see **Fig. 5a**). For every color channel and for every plane the state vector S^t contains entries for each of the 10 degrees of freedom. For example, for a two-color, three-plane configuration, the state vector S would be of length 60.

Decoupling state variables

The fundamental difficulty in adding the angular degrees of freedom α_1 and α_2 as well as β_1 and β_2 is their coupling with I_1 and I_2 and indirectly D_1 and D_2. Indeed, since the rotation axes of

Nature Biotechnology: doi:10.1038/nbt.3708

the light sheets are not necessarily matched to the geometrical center of a given optical section of the specimen, a change of the angular degrees of freedom can also lead to a defocus of the light sheets relative to the detection focal planes. A simple calibration scheme can be utilized to identify the parameters required to shift the rotation point of a light sheet to a specific point within the sample:

$$I' = I - d_\alpha \tan(\alpha) - d_b \tan(\beta) \qquad \text{(Eq. 59)}$$

Here, $\binom{d_\alpha}{d_\beta}$ is the vector that displaces the light-sheet's rotation point. **Supplementary Fig. 2c** illustrates how translating the light sheet by $-d_\theta \tan(\theta)$ along the z-axis (where θ is either α or β) effectively shifts the position of the rotation axis by d_θ along the y-axis. This transformation ensures orthogonality of the image quality metric with respect to the positions and angles of the light sheets. In the following we assume that for each light sheet the control variables I, α and β have been decoupled by such a transformation. The optimization of the variables Y, α and β is largely independent of the main variables D and I. It follows that each of these degrees of freedom can be optimized as an independent, one-dimensional optimization problem. For simplicity we thus ignore the new, additional variables in the following exposition. A detailed explanation of the implementation of α and β measurements is provided in Part V.

Constraint graph

In a manner reminiscent of factor graphs in Bayesian probability theory, we can represent the optimization problem as a constraint graph in which the nodes are state variables (individual entries of the state vector S) and the edges are constraints on these variables. **Supplementary Fig. 9a** provides an example of a constraint graph for a two-color, three-plane configuration with a single bridging plane (z_1) and the same center of mass for both color channels. In this example, there are three types of constraints: defocus constraints (F) that are dependent on defocus measurements and can thus vary in time, equality constraints (=) that enforce sample depth invariance of the positions of the detection objectives, and center of mass equality constraints (C) that ensure that the mid-point between the two detection objectives is the same for all color channels. For simplicity we omitted constraints that are required for anchoring the system or handling missing or unreliable defocus information. In the following we discuss in detail the three constraints shown in **Supplementary Fig. 9a** as well as other useful constraints.

Defocus constraints

The most important constraints are defocus constraints that link detection objectives positions (D_1, D_2) to light sheet positions (I_1, I_2):

$$\Delta F_{u,v} = \Delta D_u - \Delta I_v \qquad \text{(Eq. 60)}$$

Nature Biotechnology: doi:10.1038/nbt.3708

The sign of the difference is chosen so that $\Delta D_u \, \Delta F_{u,v} > 0$, which allows measuring the defocus $\Delta F_{u,v}$ by changing D_u while keeping I_v constant.

Equality constraints

This other very basic constraint arises e.g. when it is necessary for the positions of the detection objectives (D_1 and D_2) to be invariant with imaging depth (z):

$$0 = \Delta D_u^z - \Delta D_u^{z\prime} \qquad \text{(Eq. 61)}$$

This signifies that any change ΔD_u^z to D_u^z must be accompanied by the same change to $D_u^{z\prime}$. Assuming that D_u^z and $D_u^{z\prime}$ are initially equal it follows that D_u^z and $D_u^{z\prime}$ will remain equal after corrections are applied. The differential aspect of these constraints can be removed by replacing 0 with a correction term obtained by observing the current values of $D_u^{t,z}$ and $D_u^{t,z\prime}$:

$$-\left(D_u^{t,z} - D_u^{t,z\prime}\right) = \Delta D_u^z - \Delta D_u^{z\prime} \qquad \text{(Eq. 62)}$$

This ensures that the corrections ΔD_u^z and $\Delta D_u^{z\prime}$ are such that $D_u^{t+1,z} = D_u^{t+1,z\prime}$, even if this is not the case initially.

Center of mass equality constraints

Detection objectives suffer from chromatic aberrations that cause the working distance to slightly vary from one wavelength to another. For example, for the Nikon 16x/0.8 objectives used in some of our experiments, the focal plane shifts by about 0.8 μm when imaging GFP vs. RFP. Since the SiMView-type multi-view light-sheet microscopy arrangement used in our study employs two detection objectives that face each other, different wavelengths require different relative distances between the two objectives. Ideally, the center of mass of the two objectives should be stationary as it coincides with the focal planes. This constraint can be expressed as follows:

$$0 = \Delta D_1^{\lambda_1} + \Delta D_2^{\lambda_1} - \Delta D_1^{\lambda_2} - \Delta D_2^{\lambda_2} \qquad \text{(Eq. 63)}$$

Similarly, this differential constraint can be made integral:

$$-\left(D_1^{\lambda_1} + D_2^{\lambda_1} - D_1^{\lambda_2} - D_2^{\lambda_2}\right) = \Delta D_1^{\lambda_1} + \Delta D_2^{\lambda_1} - \Delta D_1^{\lambda_2} - \Delta D_2^{\lambda_2} \qquad \text{(Eq. 64)}$$

For simplicity in our notation, we omit t in $D_1^{\lambda_1}$, $D_2^{\lambda_1}$, $D_1^{\lambda_2}$, $D_2^{\lambda_2}$.

Nature Biotechnology: doi:10.1038/nbt.3708

Anchoring constraints

The matrix M in **Supplementary Fig. 9a** does not have full rank. There remains one unconstrained degree of freedom: the center of mass of the entire system can be translated while still maintaining proper instrument alignment.
To anchor the system and prevent drift over multiple correction rounds, one can constrain the center of mass of the detection objectives to remain constant:

$$0 = \Delta D_1 + \Delta D_2 \quad \text{(Eq. 65)}$$

Again, in integral form this can be expressed as follows:

$$-(D_1 + D_2) = \Delta D_1 + \Delta D_2 \quad \text{(Eq. 66)}$$

The corresponding constraint is shown in **Supplementary Fig. 9c**.

Filling-in missing information with substitution constraints

We previously discussed those cases in which fluorescent signals may be (sometimes or even permanently) low or nonexistent for certain color channels or reference planes in which the respective fluorescent markers are not present. In this situation image quality measurements are not necessarily reliable. In the interest of system robustness, it is thus preferable to use neighboring planes or complementary color channels as proxies. In this way one can e.g. substitute missing defocus observations by interpolating neighboring light-sheet positions. This can be done in practice by simple averaging, for example:

$$0 = -2\Delta I_v^{z_k} + \Delta I_v^{z_{k-1}} + \Delta I_v^{z_{k+1}} \quad \text{(Eq. 67)}$$

If this is the only constraint involving $\Delta I_v^{z_k}$ the value of $I_v^{z_k}$ will follow the average variation of its neighbors, but it will not necessarily be equal to the average value of its neighbors. Alternatively, we can use the integral form:

$$-\left(-2I_v^{z_k} + I_v^{z_{k-1}} + I_v^{z_{k+1}}\right) = -2\Delta I_v^{z_k} + \Delta I_v^{z_{k-1}} + \Delta I_v^{z_{k+1}} \quad \text{(Eq. 68)}$$

In this case, the value of $I_v^{z_k}$ will be the average of $I_v^{z_{k-1}}$ and $I_v^{z_{k+1}}$after corrections are applied even if this is not the case initially. The corresponding constraint is shown in **Supplementary Fig. 9c**.

From constraint graph to the generalized focus matrix

Each constraint in the graph is a linear equation involving a subset of entries in S and the corresponding entry in F. It follows that each constraint can be encoded as a row in matrix M. **Supplementary Fig. 9b** shows the matrix M corresponding to the constraint graph in

Nature Biotechnology: doi:10.1038/nbt.3708

Supplementary Fig. 9a. The different types of constraints are implicitly grouped together in matrix M by means of ordering the entries in F.

Generalized focus matrix

The generalized focus matrix explicitly relates the vector of defocus observations ΔF to the state vector correction ΔS:

$$\Delta F = M \Delta S \qquad \text{(Eq. 69)}$$

In contrast to the basic approach (special optimization theory), the state vector S now contains the state information for all colors and planes, and ΔF contains defocus measurements and correction terms for integral constraints.

Obtaining the optimal correction vector

Corrections ΔS of the state vector S are computed by pseudo-inverting the focus matrix M and computing ΔS given ΔF:

$$\Delta S = M^{+} \Delta F \qquad \text{(Eq. 70)}$$

As discussed in Part III this solution corresponds to the least-squares solution (L_2 norm). This means that the vector ΔS of minimal energy (L_2 norm) is returned. This is the simplest approach to obtaining ΔS. We formulate two more sophisticated and powerful approaches below.

L1 minimization based solver

The approach described previously is best if M is of full rank or is over-constrained. If M is not of full rank – for example if the system is not anchored – the problem is ill-posed, as there are potentially many different solutions ΔS. In this case it is advantageous to search for the solution ΔS of minimal L_1 length that favors sparse correction vectors ΔS. Intuitively, this approach modifies the least number of degrees of freedom to achieve optimal focus.

Optimal bounded corrections

Despite all our efforts to limit the propagation of noise from the measurements to the actual corrections, it remains necessary in practice to limit the correction amplitude of certain degrees of freedom more than others (for example for detection planes $D_u^{t,z}$ versus light sheet offsets $I_v^{t,z}$). Limiting corrections after optimization is not an option because it might lead to an improperly aligned system. Our solution to this problem consists of integrating the bounds into a more general optimization problem.

Nature Biotechnology: doi:10.1038/nbt.3708

We solve the following constrained quadratic programming problem:

$$\begin{aligned} &\underset{\Delta X}{\operatorname{argmax}} \|\mathrm{M}\Delta S - \Delta F\|^2 \\ &\quad -L_i < \Delta S_i < L_i \qquad \text{for all } i \\ &-\Delta F_i < (M\Delta S)_i < \Delta F_i \end{aligned} \tag{Eq. 71}$$

The L_i are the components of the limits vector L that limit corrections for each degree of freedom. The values ΔS_i are the components of the state correction vector ΔS, and $(M\Delta S)_i$ are the components for the vector $M\Delta S$. The first set of inequalities limits the corrections for each degree of freedom. The second set ensures that when a constraint from the constraint graph is already satisfied, $(\Delta F)_i = 0$, it will remain satisfied, $(M\Delta S)_i = 0$. Another way to understand the role of these inequalities is as *sparsity-inducing inequalities* that avoid propagation of corrections throughout the constraint graph by favoring local corrections for local problems (but not local solutions to global problems).

Robust hybrid solver

In practice, we use a robust hybrid solver that combines the three solvers described above. While the quadratic programming based solver (QP solver) produces the most accurate results, it requires a semi-definite matrix M and is thus fragile if exposed to missing information – e.g. when focusing fails at certain planes or in certain imaging channels. To mitigate this problem, we detect when the QP solver fails and fall back to the L1 solver, which is still able to provide bounded results but in a less accurate manner. If the L1 solver itself fails, we finally fall back to an L2 solver that cannot fail but offers the lowest quality for state corrections. It should be noted that there are additional reasons why the more advanced solvers could fail – for example, the optimization routine of the QP solver can also fail internally as a result of numerical instabilities. The general philosophy applied here for ensuring robustness without sacrificing quality is to first try the advanced, higher-quality but more brittle algorithms and then fall back to simpler, lower-quality but also more robust algorithms if needed.

Scheduling observations and corrections

A correction cycle consists of (i) acquiring all defocus measurements ΔF and (ii) computing the correction vector ΔS and applying these corrections. Defocus measurements are obtained as described in Part III.

Instant local defocus corrections

In extreme cases, a correction cycle for several color channels and many reference planes can take up to a few minutes to complete. In particular, there is a delay between the defocus measurements and the application of corrections (the expected delay is half a correction cycle). This means that on average 1.5 correction cycles elapse until a system perturbation is corrected.

Nature Biotechnology: doi:10.1038/nbt.3708

However, we can apply defocus corrections for the light sheets immediately after observing them, while keeping the last corrected system state unchanged as a reference for subsequent observations and corrections. Thereby, we do not affect the normal global correction cycle but at the same time correct defocus locally as quickly as possible. An important point is that these fast local corrections can only modify I_1 and I_2 but cannot be allowed to modify the values D_1 and D_2. This can be understood from the constraint graph (see for example **Supplementary Fig. 9a**), in which the variables for I_1 and I_2 are 'leaf nodes' and can thus be optimized locally as a first approximation.

Nature Biotechnology: doi:10.1038/nbt.3708

Part V | Analysis of Three-Dimensional Light-Sheet Geometry

In Parts III and IV we discussed adjustments of non-angular degrees of freedoms (D, I, Y) by means of sequential line searches. Here, we will explain how the two angular light-sheet degrees of freedom α and β can be reliably determined. Line searches are inappropriate for α and β because changing the light-sheet angles also changes the section of the sample that is illuminated. In this scenario, it would then be necessary to compare the quality of images that originate from different underlying fluorophore distributions, which results in an ill-posed problem. In the following, we will provide details on the image analysis algorithm we developed for extracting light-sheet geometry parameters directly from a single focus stack – the same stacks used for optimizing D and I. This approach thus avoids changing the light-sheet angles for determining the 3D light-sheet geometry, thus overcoming the problem outlined above, and has the additional advantage of minimizing the number of images that need to be acquired to optimize the system state, thus minimizing the impact on the specimen's photon budget.

Light-sheet geometry alpha and beta angles

As explained previously, one key feature of the implementation of our light-sheet microscope for spatiotemporally adaptive imaging is the ability to digitally control light-sheet geometry (translation along two axes and rotation around two axes) relative to the detection focal planes. As shown in **Supplementary Fig. 8a** there are thus four primary degrees of freedom for each light sheet: (I, Y, α, β). **Fig. 5** illustrates in more detail the relationship between the two angles, the sample and the detection planes.

Why optimize angles alpha and beta?

Traditionally, the light-sheet angle alpha is adjusted during system alignment of a light sheet microscope (if this degree of freedom has been considered in the design of the microscope). While adjusting this degree of freedom needs to be done properly, the angle alpha is not expected to drift substantially over time nor to be primarily responsible for serious imaging artifacts during an experiment. However, for large specimens and/or complex specimen geometries (with refractive index distributions that differ from the mounting medium) we can expect to encounter aberrations and light refraction that – among other effects – lead to an angular mismatch of light-sheet plane and detection focal plane. In contrast to the angle alpha, there is usually a much stronger case for adjusting the angle beta in a depth-dependent manner. For example, for typical spherical or ellipsoidal samples (such as zebrafish or *Drosophila* embryos), the light-sheet incidence angle relative to the medium-to-sample-interface varies from −90 degrees to +90 degrees as we move the imaging plane from one end of the specimen to its other end. When entering the sample the light sheet is thus refracted by an amount that depends on the position of the image plane (see illustration on **Fig. 5f**). Because of this differential path deflection of the light-sheet plane different image planes in the sample require different angular focus adjustments to restore optimal image quality. This consideration shows that, in practice,

Nature Biotechnology: doi:10.1038/nbt.3708

there is no substitute for an angular adjustment since no focus translation adjustment can fully correct for the inevitable refraction of the light sheet.

Angle analysis algorithm

Fig. 5d illustrates our algorithm used to determine light-sheet parameters (z, α, β), which include the two light-sheet angles as well as the offset position *z* of best focus quality (thus fully defining the 3D geometry of the light-sheet plane). The value z considered here corresponds to the position of the light sheet relative to the current position of the detection focal plane (unlike *I*, which describes the absolute position of the light sheet). The input to the algorithm is the standard focus stack S acquired for refocusing purposes. This stack consists of several images S_k (9 or 11 images in practice). The first step is then to crop the images and divide the cropped stack into sub-stacks $S_{i,j}$. For each sub-stack $S_{i,j}$ we compute the DCTS of each image $DCTS(S_{k,i,j})$ and determine the optimal focus depth $z_{i,j}$ for each sub-stack (i,j) individually. For some sub-stacks it may not be possible to determine reliable focus information because of statistically non-significant fitting (e.g. as a result of lack of signal or poor image quality in a remote location of the stack with exceptionally long illumination and detection path lengths) – the corresponding data points are discarded. We also perform additional filtering of data points to remove outliers both in terms of their geometric isolation and in terms of their maximal DCTS value per sub-stack. The next step is to use the data points collected $(x_{i,j}, y_{i,j}, z_{i,j})$ to find the most likely plane passing through these points. This plane corresponds to the light-sheet plane itself and can in principle be found by applying a simple least square regression. However, since outliers can still remain among the data points even after careful filtering, we instead use a robust linear fit estimator capable of distinguishing inliers from outliers. The final result is a 2D plane fit of the form:

$$z = ax + by + c \qquad \text{(Eq. 72)}$$

We can then extract the two angles as follows:

$$\alpha = \operatorname{atan}(b) \qquad \text{(Eq. 73)}$$

$$\beta = \operatorname{atan}(a) \qquad \text{(Eq. 74)}$$

Robust light-sheet plane fitting

Robust model estimation is a very well-studied problem in computer vision. We recommend in particular the review by Stewart[26] for a wider exposition discussing available approaches to this end. In the following we will outline two approaches to robust estimation based on ideas from statistical hypothesis testing. The key feature of these approaches is that they are parameter-less, i.e. no parameter needs to be adjusted based on a noise or outlier model. This is an essential feature for any algorithm utilized for the decision-making process in a microscopy framework

Nature Biotechnology: doi:10.1038/nbt.3708

for automated and robust adaptive imaging – once an experiment has started it is unlikely that the user will have time and sufficient information to further adjust parameters.

Theory of robust model estimation

The problem can be formulated as follows. We start with a set of n vectors X_i which constitute our data points:

$$P = \{X_i | i \in [0, n]\} \quad \text{(Eq. 75)}$$

In addition, we have a function f: $S \longrightarrow \mathbb{R}^+$ that defines the loss function of a model. For example if the model is a least-squares linear fit, the function f applied on a subset S of data points would return the sum of square deviations of the data points in S to the best least-squares fit. Searching for the subset S that minimizes f would not give any meaningful result: in the case of a 1D linear fit all pairs of points lead to a sum of square deviations of zero. Instead, we reformulate the problem from a statistical point of view: assuming that outliers follow a normal distribution, and given a subset S, what is the p-value for observing the value $f(S)$? In other words, what is the probability of observing a value of f *equally or more* extreme than $f(S)$? Computing these p-values can be done empirically, which can lead to very accurate estimates when appropriate randomization schemes are applied. However, the disadvantage of empirical methods is that they require expensive sampling that can negatively affect performance. Instead we rely on the fact that the sum of squared deviations for k points of dimension d follows the well-characterized Chi-squared distribution Ξ^2_{k-d}, where $k - d$ are the number of degrees of freedom of the distribution. The above assumes that the data points X_i have been normalized so that their mean is 0 and their standard deviation is 1. For example, if we consider our original problem of fitting a 2D plane through k points, then $d = 3$ since the points are embedded in $\mathbb{R}^3$. For $k < 3$ the fit is undefined; for $k = 3$ there is exactly one fit and the distribution of sum of squared deviation is singular (Dirac at zero); for $k = 4$ we have one degree of freedom – the fourth point introduces one degree of freedom which corresponds to distribution X^2_1. We can compute the p-value with the following integral:

$$p_v(S) = \int_{f(S)}^{\infty} \Xi^2_{k-d}(\zeta) d\zeta \quad \text{(Eq. 76)}$$

From this p-value we can compute the quantity $p(S) = 1 - p_v(S)$ which we re-interpret as the probability that the fit is *not due to chance alone*. In the following we will use this quantity as a score for comparing different inlier candidates S for model f. The original problem can be formulated as the search for the inlier set I that maximizes (S):

$$I = \underset{S}{\operatorname{argmax}}\, p(S) \quad \text{(Eq. 77)}$$

Nature Biotechnology: doi:10.1038/nbt.3708

Because there are exponentially many subsets, we need to use a heuristic sampling approach followed by move-based local refinements. First we initialize our seed set as $S = \{X_i\}$ with a single randomly chosen point. We then add points iteratively to S: we pick a point in S and add its closest neighboring point in P. We repeat this until a minimal number of points m have been added to S. This heuristic favors the creation of seed sets that are clustered in space. The intuition behind this heuristic is that spatially clustered points are more likely to belong to the inlier set than a random subset. Next we refine this set by checking if single points can be added or removed to increase the value of $p(S)$. This local search leads to a local minimum and thus a candidate set S_k. We repeat this procedure q times to obtain a collection of candidate sets $\{S_k | k \in [1, q]\}$. The final inlier set is found as:

$$I = \underset{S_k}{\operatorname{argmax}}\{p(S_k) | k \in [1, q]\} \qquad \text{(Eq. 78)}$$

Multiple model fits can be found by repeatedly subtracting the inlier sets $P \setminus I$ and applying the above procedure until no further inliers sets are found above a certain probability threshold.

Ensemble estimation for plane fitting

An alternative approach is used if initial filtering is sufficiently accurate that we can assume that the data points are mostly inliers. In this case we can use a Thiel-Sen type estimator to fit a 2D plane through the data points in $\mathbb{R}^3$. We repeatedly pick 6 points randomly from the set S, fit a plane using least squares, and determine the median plane – obtained by computing the median parameters for all fitted planes. This rather simple approach is surprisingly competitive both in terms of speed and robustness.

Angle analysis benchmark

To validate our algorithm for computing the light sheet angles alpha and beta, we collected a benchmark dataset of focus stacks acquired at two depths in the embryo (50 µm relative to the surface facing detection arm 1 as well as 50 µm relative to the surface facing detection arm 2). For each depth several focus stacks were acquired while varying the angles alpha and beta: $\alpha, \beta \in \{-2, -1, -0.5, -0.25, 0.25, 0.5, 1, 2\}$. The angles were changed manually using the microscope control software. The sample used for collecting these stacks was a nuclear labeled *D. melanogaster* embryo. As shown in **Supplementary Fig. 11a**, the imposed and measured alpha angles are correlated and the average errors are below a quarter of a degree (0.14º for α and 0.21º for β). Importantly, the linear fit is the same for the two planes indicating that there is no depth-dependent alpha deflection of the light sheet. This result is in good agreement with the expected behavior for a specimen with mirror-symmetrical shape along the axis defined by an alpha angle of 0. In contrast, **Supplementary Fig. 11b** shows that for two diametrically opposed planes within the embryo and an imposed beta angle of 0, measured beta angles exhibit identical

Nature Biotechnology: doi:10.1038/nbt.3708

amplitudes but opposite signs for these two planes. Moreover, we observe the same linear relationship between imposed and observed angles for the beta degree of freedom. Overall, these results validate our algorithm for determining the effective 3D light sheet orientation within the sample and confirm that the sample itself influences the beta angle in good qualitative agreement with expectations arising from specimen geometry.

Galvanometer scanner calibration

We use two pairs of two-axis galvanometer scanners per illumination arm to control the 3D propagation of each light sheet in space (providing digital access to degrees of freedom *A*, *B* and *I*; the fourth degree of freedom, *Y*, is controlled by the piezo positioners the illumination objectives are mounted on). In the absence of prior calibration the imposed and measured angles are not necessarily identical but can be related by an affine transformation (see note on **Supplementary Fig. 11a**). An automated procedure can be devised to use the observed angle deflections and adjust the calibration parameters.

Measuring angular deflection in an embryo

We measured the α and β angular deflections caused by the optical properties of a *D. melanogaster* embryo surrounded by water. The results presented in **Supplementary Fig. 17** show that while the α-deflection is almost constant for each combination of light sheet and camera (with good agreement of results obtained by the two cameras for the same light sheet), the β-deflection follows a considerably more complex pattern. On the one hand, as illustrated in **Fig. 5**, refraction of the light-sheet is the dominant effect necessitating compensatory β-deflections where the light-sheet incidence angle relative to the surface of the embryo is large. On the other hand, detection focal planes become increasingly curved with increasing depth of image planes inside the embryo. For intermediate depths (measured relative to the detection arm), both effects are relatively weak, which results in the smallest combined deflection observed across the embryo. In the following, we provide a simple ray optics model that quantifies these phenomena and yields theoretical estimates of optimal adaptive imaging settings that are in good agreement with experimental measurements.

Ray optics model for interpreting experimentally observed β-deflections

The depth-dependency of the β-deflection observed in **Supplementary Fig. 17** and illustrated in **Fig. 5** can be modeled as the sum of two contributing effects. In the following we assume for simplicity a cylindrical geometry of the sample (using parameters x, z and θ as defined in **Supplementary Fig. 18a**), which serves as a first-order approximation of the shape of the *Drosophila* embryo imaged in this experiment.

Nature Biotechnology: doi:10.1038/nbt.3708

First, we need to consider refraction of the incident light sheet, which introduces an angular deviation of β_i with respect to the original beam path (**Supplementary Fig. 18a**) that can be modeled using Snell's law:

$$\beta_i(z_i) = \sin^{-1}\frac{\kappa z_i}{r} - \sin^{-1}\frac{z_i}{r} \qquad \text{(Eq. 79)}$$

$z_i \in [-r, +r]$ is the offset position of the incident light sheet along the detection axis (with $z_i = 0$ corresponding to the center of the embryo, $z_i = r$ corresponding to the front surface of the embryo relative to the detection arm and $z_i = -r$ corresponding to the back surface of the embryo relative to the detection arm), r is the radius of the cylinder, and $\kappa = \frac{n_m}{n_e}$ is the ratio of refractive indices of mounting matrix (n_m) and sample (n_e). Considering the geometry and optical properties of *Drosophila* embryos, let us then assume a radius $r = 100$ µm, a refractive index of $n_m = 1.339$ for the mounting matrix[27] (1% agarose) and a refractive index of $n_e = 1.35$ for the sample itself (using the typical refractive index of cytosol as an approximation[28]). We thus obtain a ratio $\kappa = \frac{1.339}{1.35}$, which results in the following deflection curve $\beta_i(z_i)$:

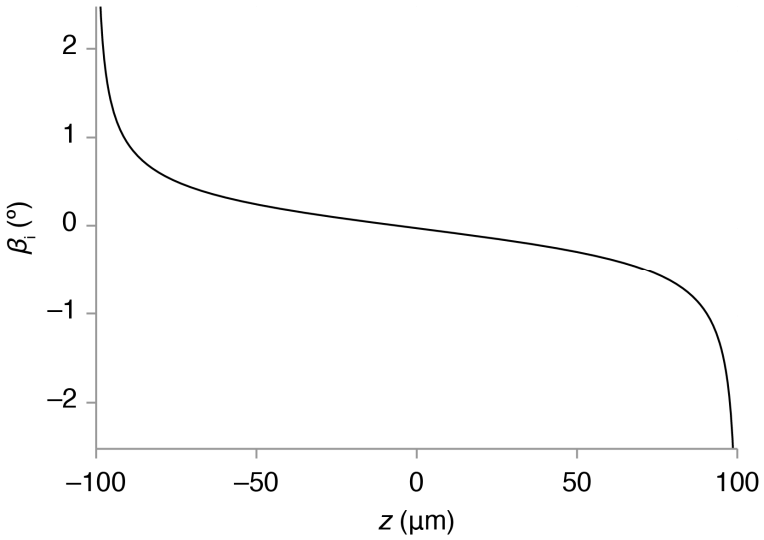

Second, we need to consider the bending of the detection focal plane deep inside the embryo (**Supplementary Fig. 18b**), which is also an effect that arises from the small difference between n_m and n_e. The geometrical length of the optical detection path, i.e. the distance between the plane defined by the objective's front aperture and a point located on the detection focal plane, depends on the lateral offset x of the point relative to the center of the embryo, resulting in a curvature of the detection focal plane.

Let us assume that the detection focal plane is positioned at $z = z_f$, using the mounting matrix surrounding the embryo as a reference location (**Supplementary Fig. 18b**). The optical path

Nature Biotechnology: doi:10.1038/nbt.3708

length is invariant, i.e. it is identical for focus locations inside the embryo ($0 \leq x \leq r$) and focus locations outside the embryo ($r < x$):

$$n_m(r - z_f) = n_m\left(r - \sqrt{r^2 - x^2}\right) + n_e\left(\sqrt{r^2 - x^2} - z'\right) \quad \text{(Eq. 80)}$$

It follows that:

$$z'(x, z_f) = \kappa z_f + (1 - \kappa)\sqrt{r^2 - x^2} \quad \text{(Eq. 81)}$$

The partial derivative of $z'(x, z_f)$ along x is:

$$\frac{\partial z'}{\partial x} = (\kappa - 1)\frac{x}{\sqrt{r^2 - x^2}} \quad \text{(Eq. 82)}$$

Note that $z' = z_f$ at the coordinate where the focal plane intersects with the surface of the specimen ($x^2 = r^2 - {z_f}^2$). In this particular location the partial derivative has the following value:

$$\left.\frac{\partial z'}{\partial x}\right|_{x^2 = r^2 - {z_f}^2} = (\kappa - 1)\sqrt{\frac{r^2}{{z_f}^2} - 1} \quad \text{(Eq. 83)}$$

Eq. 83 provides the slope of the tangent to the curved focal plane at the interface between sample and surrounding medium. The slope of the curved focal plane reaches its maximum at this point. This value thus represents an upper bound for the apparent deflection angle β_d caused by the bending of the detection focal plane:

$$\beta_d < \tan^{-1}\left((\kappa - 1)\sqrt{\frac{r^2}{{z_f}^2} - 1}\right) \quad \text{(Eq. 84)}$$

Nature Biotechnology: doi:10.1038/nbt.3708

Assuming the same refractive index ratio κ and same radius r as above, we obtain:

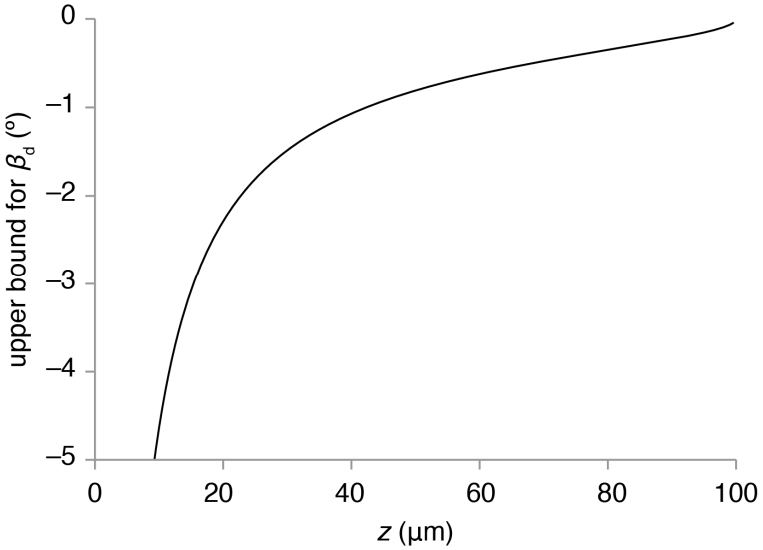

In practice, it is unlikely that this steep slope can manifest itself as an experimental observable, considering that it occurs in a theoretically infinitely small region within the sample. Instead, we can derive an experimentally more relevant prediction if we consider that each light sheet can only illuminate approximately half of the embryo[21] and that high-resolution imaging is limited to approximately the first 1/8th of the embryo's cross-section as a result of light scattering and absorption[29]. To this end, we can determine the slope of the line connecting the intersection point P_1 between the detection focal plane and the embryo's surface (on the side of the embryo facing the light sheet) and the point P_2 on the detection focal plane located at an x-depth corresponding to 1/8th of the x-length of the embryo's cross-section. The vectors pointing to these points P_1 and P_2 are as follows:

$$\overrightarrow{p_1} = \begin{pmatrix} \sqrt{r^2 - {z_f}^2} \\ z_f \end{pmatrix} \quad \text{(Eq. 85)}$$

$$\overrightarrow{p_2} = \begin{pmatrix} \frac{3}{4}\sqrt{r^2 - {z_f}^2} \\ \kappa z_f + (1-\kappa)\sqrt{\frac{7}{16}r^2 + \frac{9}{16}{z_f}^2} \end{pmatrix} \quad \text{(Eq. 86)}$$

Nature Biotechnology: doi:10.1038/nbt.3708

We can thus compute the slope of the line connecting these two points as an approximation of the angle β_d:

$$\beta_d \simeq \tan^{-1}\left((\kappa - 1)\frac{\left(4z_f - \sqrt{7r^2 + 9{z_f}^2}\right)}{\sqrt{r^2 - {z_f}^2}} \right) \qquad \text{(Eq. 87)}$$

Note that this formula is only valid for positive values of z_f. Due to the mirror symmetry underlying the imaging arrangement, the sign of β_d in Eq. 87 needs to be reversed for negative values of z_f.

Assuming again the same refractive index ratio κ and same radius r as above, this yields the following spatial dependency of β_d:

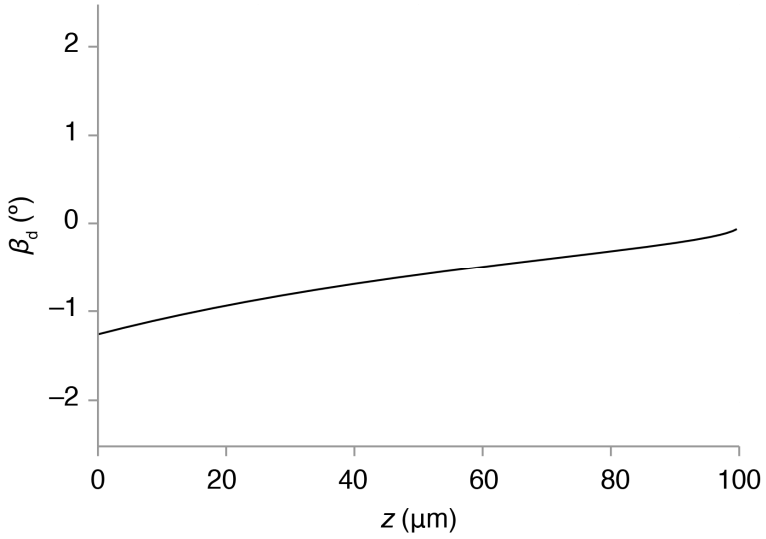

If we combine the β-deflection resulting from refraction in the illumination path with the β-deflection resulting from the lensing effect in the detection path, we obtain the following analytical result (assuming that $z = z_i = z_f$):

$$\begin{aligned} \beta(z) &\simeq \beta_i + \beta_d \\ &\simeq \sin^{-1}\frac{\kappa z}{r} - \sin^{-1}\frac{z}{r} \\ &\quad + (\operatorname{sgn} z)\tan^{-1}\left((\kappa - 1)\frac{\left(4z_f - \sqrt{7r^2 + 9{z_f}^2}\right)}{\sqrt{r^2 - {z_f}^2}} \right) \end{aligned} \qquad \text{(Eq. 88)}$$

Nature Biotechnology: doi:10.1038/nbt.3708

For $\kappa = \frac{1.339}{1.35}$, this yields the following quantitative result:

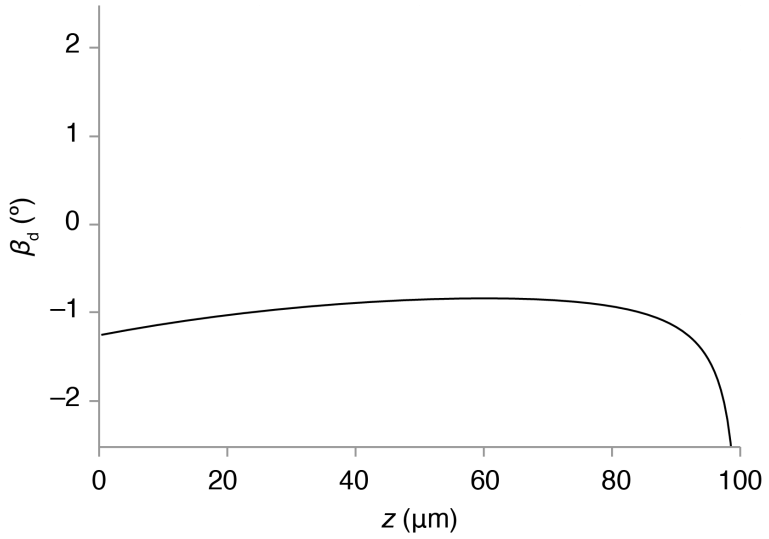

Note that the minimal absolute deflection is $\beta_{min,abs} = 0.82$. The minimal deflection angle represents a parameter that is straight-forward to measure experimentally and thus lends itself well to a comparison of theoretical model and experimental results. As shown in **Supplementary Fig. 18**, the predicted value of $\beta_{min,abs} = 0.82$ is reasonably close to the minimal apparent deflection of roughly $\beta_{min,abs} \simeq 0.5$ observed in the experimental data.

To conclude this section, let us consider two additional scenarios, in which the ratio of refractive indices of mounting matrix (n_m) and sample (n_e) is higher or lower, respectively, than the ratio considered in the data-driven example provided above.

For $\kappa = \frac{1.339}{1.36}$, the theoretical spatial dependency of β is as follows:

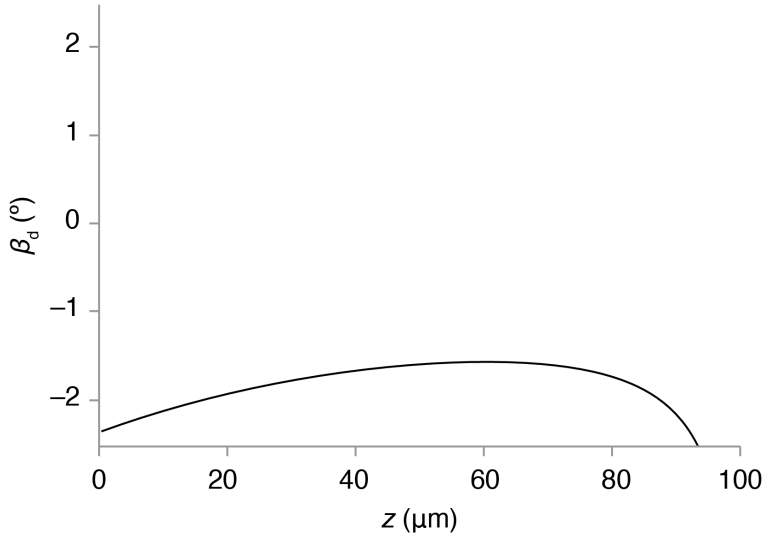

Nature Biotechnology: doi:10.1038/nbt.3708

The minimal absolute deflection $\beta_{min,abs}$ in this scenario is larger than 1.5 and thus substantially larger than the minimal β-deflection observed in our experimental data.
If we instead assume a value of $\kappa = \frac{1.339}{1.34}$, we obtain:

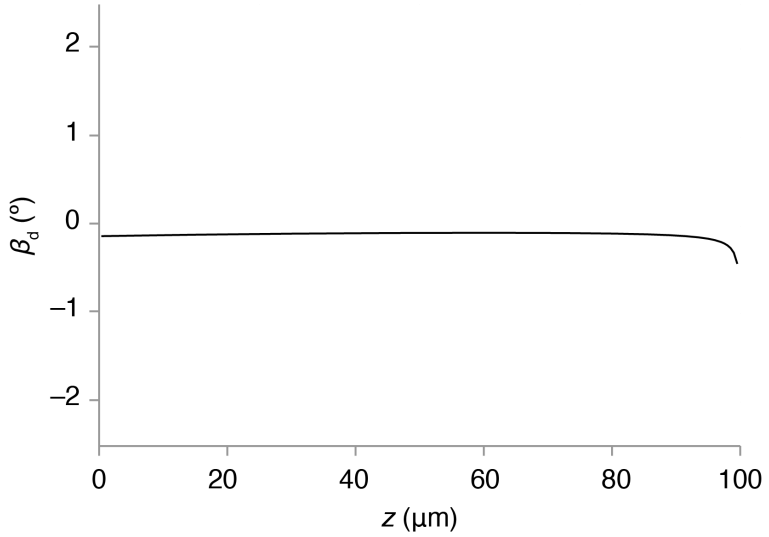

In this case, the minimal absolute deflection $\beta_{min,abs}$ is smaller than 0.1 and thus substantially smaller than the deflection observed experimentally. The initial estimate of $\kappa = \frac{1.339}{1.35}$ suggested by literature[27, 28] thus leads to the best agreement between experiment and theoretical prediction of the minimal β-deflection angle. Finally, we note that the relatively simple model described here, which approximates optical effects using ray optics (considering only the chief ray and assuming a cylindrical shape of the embryo) and assumes a uniform refractive index throughout the specimen, is already sufficient to explain the main features observed in the shape of the experimentally measured $\beta(z)$ function. Independently of the value assigned to κ, the theoretical model is in good qualitative agreement with experimental data with respect to the sign of the second derivative and point symmetry of $\beta(z)$.

Potential of AutoPilot measurements in informing geometrical corrections of image space

Without the corrections applied by the AutoPilot framework, the geometry of image space is distorted owing to the specimen lensing effect and light-sheet refraction at the surface of the specimen, as discussed above; moreover, image quality is reduced owing to the loss of co-planarity of light-sheet and detection planes. The AutoPilot framework addresses the second phenomenon by recovering co-planarity; the geometry of the image space remains slightly distorted. While we account for possible geometrical distortions to some extent in our multi-view fusion pipeline (by aligning and fusing multiple views such that data continuity between views is optimized within the constraints of an affine model), each specimen view itself suffers from a slight non-linear geometric distortion. The measurements performed by the AutoPilot framework

Nature Biotechnology: doi:10.1038/nbt.3708

offer valuable information about these distortions. This knowledge could in theory be used to "straighten" the image stacks.

We should note that distortions of the geometry of image space are on average on the order of 0.4-1.0 μm across the specimens studied in this work and are thus likely smaller than the natural variance of the locations of biological structures across individuals. For most quantitative applications, these residual distortions are thus likely not of significant practical importance. However, if very precise geometrical measurements in living samples are required – for example when imaging and spatially registering very large (yet sufficiently transparent) samples such as chemically cleared mouse brains – a post-processing step that attempts to recover the true geometry of the sample as precisely as possible may be helpful.

Nature Biotechnology: doi:10.1038/nbt.3708

Part VI | Quantifying Improvements in Spatial Resolution and Image Quality

In this section we will provide an overview of the methods used to quantify the improvements in image quality and spatial resolution achieved by spatiotemporally adaptive imaging. In the absence of fluorescent beads or other fiducials that serve as point sources, quantifying resolution is an ill-posed problem because both the local point spread function (PSF) and the true biological structure underlying the image are unknown. Introducing fluorescent beads into the sample – or for that matter any other structure of known size – reduces the indeterminacy and thus permits estimating the PSF. Unfortunately, it is usually not possible to introduce and distribute such fiducials systematically throughout the living specimen without affecting sample health, particular in long-term live imaging experiments. However, we do not need to measure absolute resolution in order to arrive at an estimate of the relative improvements achieved by spatiotemporally adaptive imaging; instead, we will focus on a strategy that allows us to compare two images of the same biological structure that were acquired in different microscope states, and quantify the relative improvement in spatial resolution in one image vs. the other. In general, such comparative estimates are necessarily lower bounds. When comparing two images of structures that exhibit only a restricted range of spatial frequencies, the potential resolution improvement made possible by spatiotemporally adaptive imaging cannot be fully observed and quantified. For example, fluorescently labeled cell nuclei are not sub-resolution-sized objects and their boundaries are not infinitely sharp. Yet, despite the fact that the estimates obtained with the methods described below represent lower bounds, we will see that the results suggest substantial improvements in spatial resolution by a factor of typically at least 2-5 in *Drosophila* and zebrafish embryos imaged with spatiotemporally adaptive microscopy. Finally, we discuss a strategy for measuring improvements in signal strength in adaptively corrected images.

Estimating a lower bound for the ratio of OTF support radii

Let us assume that we have two registered images I and I' of the same biological structure, which were acquired with an adaptively corrected system and an uncorrected system, respectively. We can then comparatively analyze the Fourier spectra of these images in order to quantify differences in quality/resolution between the two images. Although we do not have experimental access to the optical transfer function (OTF) of the microscope *in vivo* without imaging fluorescent beads *in situ*, we can obtain a lower-bound estimate for the ratio of support radii of the OTFs by determining and comparing the effective cut-off frequencies characterizing the frequency content of each image, as described below.

First we compute the Fourier power spectra of both images, $\mathcal{F}^2(I)$ and $\mathcal{F}^2(I')$. Next, we compute the background power $\mathcal{B}(I)$, which is the base level of the power spectrum outside of the diffraction-limited band-pass of the microscope. This base level is often non-zero because microscopic images usually exhibit some level of noise.

Nature Biotechnology: doi:10.1038/nbt.3708

$\mathcal{B}(I)$ can be determined by computing the median value of the power spectrum outside the band pass of the microscope:

$$\mathcal{B}(I) = med\{\mathcal{F}^2(I)_{x,y} | x^2 + y^2 > \rho^2\} \quad \text{(Eq. 89)}$$

In Eq. 89, ρ is the cut-off frequency corresponding to the diffraction-limited resolution of the microscope. We then compute the radial projections $\mathcal{R}(I)$ and $\mathcal{R}(I')$ of the two-dimensional Fourier power spectra after removing the background power $\mathcal{B}(I)$:

$$\mathcal{R}(I)(r) = \int_0^{2\pi} (\mathcal{F}^2(I) - \mathcal{B}(I))_{(r\cos\theta, r\sin\theta)}\, d\theta \quad \text{(Eq. 90)}$$

We define the cut-off radius as the radius at which the background-corrected, radially-projected power spectrum falls below a threshold corresponding to a fraction α of the maximum function value:

$$\mathcal{C}_\alpha(I) = \max\left\{r \middle| \mathcal{R}(I)(r) > \left(\alpha \max_r\{\mathcal{R}(I)(r)\}\right)\right\} \quad \text{(Eq. 91)}$$

We used a value of $\alpha = 0.01$ for the quantifications presented in this study. In the next step, we can now determine the ratio of the cut-off radii $\mathcal{C}_\alpha(I)/\mathcal{C}_\alpha(I')$ for our images I and I'. Assuming that I is the 'better' image obtained with the adaptively corrected system and that I' is the 'worse' image obtained with the uncorrected system, we typically expect to find:

$$\frac{\mathcal{C}_\alpha(I)}{\mathcal{C}_\alpha(I')} > 1 \quad \text{(Eq. 92)}$$

The ratio defined in Eq. 92 is a lower-bound estimate of the ratio of OTF support radii for the adaptively corrected (image I) and uncorrected (image I') systems. It should be noted that this lower-bound estimate is fairly conservative because it considers the image as a whole, including regions of the image that may only contain low-frequency structures and that are not relevant for estimating resolution limits. An estimate that better reflects the full improvement in spatial resolution would require manual selection of fine (i.e. high-frequency) structures in the image data and comparatively analyze only these sub-regions of the original images I and I'. This approach is explained in more detail in the next section.

Estimating a lower bound for the ratio of PSF sizes using the boundaries of cell nuclei

Complementing the analysis described above, we sought to obtain more accurate estimates of the resolution improvement in images of heterogeneous biological structures obtained with adaptive

Nature Biotechnology: doi:10.1038/nbt.3708

imaging. The results of this analysis are provided in **Supplementary Figs. 14** and **15** for both *Drosophila* and zebrafish embryonic development.

As discussed above, one would ideally want to use point sources to estimate resolution. In a biological context, this would require delivering fluorescent beads or other types of nanoparticles to the specimen using a technique that ensures systematic and uniform coverage of the specimen. This is usually not possible or advisable in long-term imaging experiments with living specimens, such as developing embryos. As an alternative strategy, however, we can avoid the introduction of such artificial fiducials and instead solve this problem computationally, by taking advantage of biological structures with high spatial frequencies, such as edges, in our fluorescent images. For example, the boundaries of fluorescently labeled cell nuclei are often sharply delimited and yield sharp edges in the image data. Intuitively, given two images I and I' of the same sample region acquired with adaptively corrected and uncorrected systems, respectively, we can estimate a lower bound for the improvement in resolution by comparing the sharpness of these edges between the two images. Here, we quantify this improvement by computing the ratio of the two slopes at the inflection point of the edge measured along an intensity profile traversing the nucleus boundary (see examples in **Supplementary Figs. 14** and **15**). In the next section, we show that the ratio of these slopes is in fact equal to the inverse size ratio of point spread functions (PSFs) that would have been obtained by imaging point sources in the same specimen location.

Estimating the ratio of PSF sizes using edge responses

First, let us consider a 1D object consisting of a single Heaviside step function at $x = 0$. We represent this object with the function f:

$$f(x) = H(x) = \begin{cases} 0 & x < 0 \\ 1 & x \geq 0 \end{cases} \quad \text{(Eq. 93)}$$

Now let us consider normalized Gaussian blurring kernels of the form:

$$g_\sigma(x) = \frac{1}{\sigma\sqrt{2\pi}} e^{-\frac{x^2}{2\sigma^2}} \quad \text{(Eq. 94)}$$

For simplicity we can think of these $g_\sigma(x)$ as our approximate 1D point spread functions. Imaging the object function f leads to an image function I obtained by convolving g_σ with f:

$$I(x) = (g_\sigma * f)(x) \quad \text{(Eq. 95)}$$

Nature Biotechnology: doi:10.1038/nbt.3708

Let us now consider the slope of the image at position $x = 0$. The derivative of a convolution can be computed in two different ways:

$$\frac{dI}{dx} = \frac{dg_\sigma}{dx} * f = g_\sigma * \frac{df}{dx} \quad \text{(Eq. 96)}$$

The derivative of the step function is simply Dirac's delta function:

$$\frac{df}{dx} = \delta \quad \text{(Eq. 97)}$$

Since the convolution with Dirac's delta function is an identity operator on distributions (Schwartz distributions), we obtain:

$$\frac{dI}{dx} = g_\sigma * \frac{df}{dx} = g_\sigma \quad \text{(Eq. 98)}$$

The slope of I at $x = 0$ is therefore:

$$\frac{dI}{dx}(0) = \frac{1}{\sigma\sqrt{2\pi}} \quad \text{(Eq. 99)}$$

If we now consider two images, I and I', which were created with two different values of sigma, σ and σ', the ratio of their slopes at the edge $x = 0$ is:

$$\frac{\frac{dI}{dx}(0)}{\frac{dI'}{dx}(0)} = \frac{\frac{1}{\sigma\sqrt{2\pi}}}{\frac{1}{\sigma'\sqrt{2\pi}}} = \frac{\sigma'}{\sigma} \quad \text{(Eq. 100)}$$

Resolution estimates are often quantified as the FWHM of the PSF, which is proportional to sigma:

$$FHWM = 2\sqrt{2\ln 2}\,\sigma \quad \text{(Eq. 101)}$$

In conclusion, the ratio of FWHM PSF sizes typically computed by comparing point responses in the respective image data can hereby be estimated using edge responses instead.

Nature Biotechnology: doi:10.1038/nbt.3708

In fact, assuming identical imaging conditions, the slope ratio at an edge is equal to the inverse FWHM PSF size ratio associated with a point object:

$$\frac{\frac{dI}{dx}(0)}{\frac{dI'}{dx}(0)} = \frac{FHWM'}{FHWM} \qquad \text{(Eq. 102)}$$

At a more abstract level, we can view this approach as a differential version of the point source approach for estimating and comparing image resolution.

For additional robustness, one can take the maximum local slopes in I and I' in order to compensate for imperfect registration and, thus, translation of the images with respect to each other. As explained above, these ratios are lower bound estimates since cell boundaries and other biological edge-like structures are not necessarily infinitely sharp. In practice, the true ratios (and thus the true improvements in resolution) are slightly higher than those estimated with the conservative strategy outlined here.

Finally, since the images suffer from shot noise and we would like to prevent this noise from adversely affecting the estimation of the profile derivatives, we filter the intensity profiles with a 1D smoothing kernel [0.25, 0.5, 0.25]. This data treatment reduces sensor noise at a spatial scale below the effective PSF support diameter (which we estimate to be 3 pixels for the particular optical configuration used). Since the support of this smoothing kernel is the same as the PSF support, the smoothing operation only marginally affects the estimation of resolution improvements. Moreover, any possible bias arising from smoothing would manifest itself as an under-estimation of the resolution improvement and thus maintain the conservative character of our quantification.

Comparing signal strength

Using the same line profiles as those utilized for the computations described in the previous section (**Supplementary Figs. 14** and **15**), we can also measure signal strength in both adaptively corrected and uncorrected images and compute the corresponding signal strength ratios. Given two profiles (i.e. 1D images) I and I', we compute the signal strength ratio (SSR) for signal amplitudes in corrected versus uncorrected images as follows:

$$SSR = \frac{(\max I) - b}{(\max I') - b} \qquad \text{(Eq. 103)}$$

In Eq. 103, $b = \min(\min I, \min I')$ represents an estimate of the background level. Using the *Drosophila* data set shown in **Supplementary Fig. 14** we obtain an average SSR of 1.57, a median SSR of 1.50, and a maximum SSR of 2.03. Similarly, for the zebrafish data set shown in **Supplementary Fig. 15** we obtain an average SSR of 2.06, a median SSR of 1.50, and a maximum SSR of 4.78.

Nature Biotechnology: doi:10.1038/nbt.3708

Reconstruction of uncorrected image data from AutoPilot logs

In addition to the primary volumetric time-lapse image data, we typically also store "AutoPilot logs" in our experiments, which contain all images acquired during microscope system optimization. These images (and specifically the defocus image sequences) can be used to reconstruct an uncorrected version of the time-lapse image data at the location of each reference plane: since we save the parameters of the initial system state, all subsequent microscope state corrections and the defocus image sequences (i.e. the images recorded for a set of finely-sampled offsets between light sheets and detection focal planes), we can automatically retrieve the image from each of these sequences that corresponds to the respective non-optimized microscope state. We note that this procedure usually overestimates the quality of the uncorrected image data in late stages of a time-lapse experiment, since the magnitude of state corrections relative to the initial microscope state at time point zero will eventually exceed the local parameter search radius of the defocus stacks (typically 4 μm) in many specimen regions. The advantage of reconstructing uncorrected image data from AutoPilot logs is that an artificial reduction of temporal resolution of the imaging experiment is avoided. This represent a contrast to the alternative strategy of using an interleaved imaging protocol, for which time points with odd and even indices are acquired with and without AutoPilot corrections, respectively (see e.g. **Supplementary Videos 6**, **7** and **9**).

Nature Biotechnology: doi:10.1038/nbt.3708

Supplementary Figures

Supplementary Figure 1 | Light-sheet microscope design for spatiotemporally adaptive imaging

Computer model of the multi-view microscope for spatiotemporally adaptive imaging. The microscope consists of two illumination arms for light-sheet illumination and two detection arms for wide-field fluorescence detection. These four arms follow an orthogonal SiMView-type arrangement and meet at the sample chamber located in the center of the microscope. Those components that are used to control certain types of degrees of freedom (DOFs) relevant for the adaptive imaging framework are shown in a color code that identifies the respective DOFs. Each illumination arm is equipped with galvanometer scanners for light-sheet formation, positioning and pivoting (DOFs: light-sheet offsets I_1 and I_2, light-sheet angles α_1, α_2, β_1 and β_2) shown in green and blue. Both illumination objectives are mounted on piezo positioners shown in red (DOFs: light-sheet axial positions Y_1 and Y_2) and both detection objectives are mounted on piezo positioners shown in yellow (DOFs: detection focal plane positions D_1 and D_2). Together, these ten digitally accessible DOFs enable full, automated control of three-dimensional positions and angular orientations of light-sheets and three-dimensional positions of detection focal planes in sample space. The microscope and the exposed DOFs are controlled by an automated software layer for spatiotemporally adaptive imaging, which monitors and constantly optimizes image quality in space and time.

We note that the galvanometer scanners for light-sheet positioning and scanning (LG1, LG2) were temporarily replaced by PI S-334 piezo tip/tilt mirrors for the perturbation experiment shown in **Supplementary Video 1**. The latter components offer the same functionality as the galvanometer scanners but provide additional analog offset inputs that simplify the introduction of "hidden" system perturbations such as those utilized in our perturbation experiment. In the absence of this particular requirement, however, we recommend the use of galvanometer scanners because of their better temperature stability and faster line repetition rates.

Nature Biotechnology: doi:10.1038/nbt.3708

Supplementary Figure 1 | Light-sheet microscope design for spatiotemporally adaptive imaging

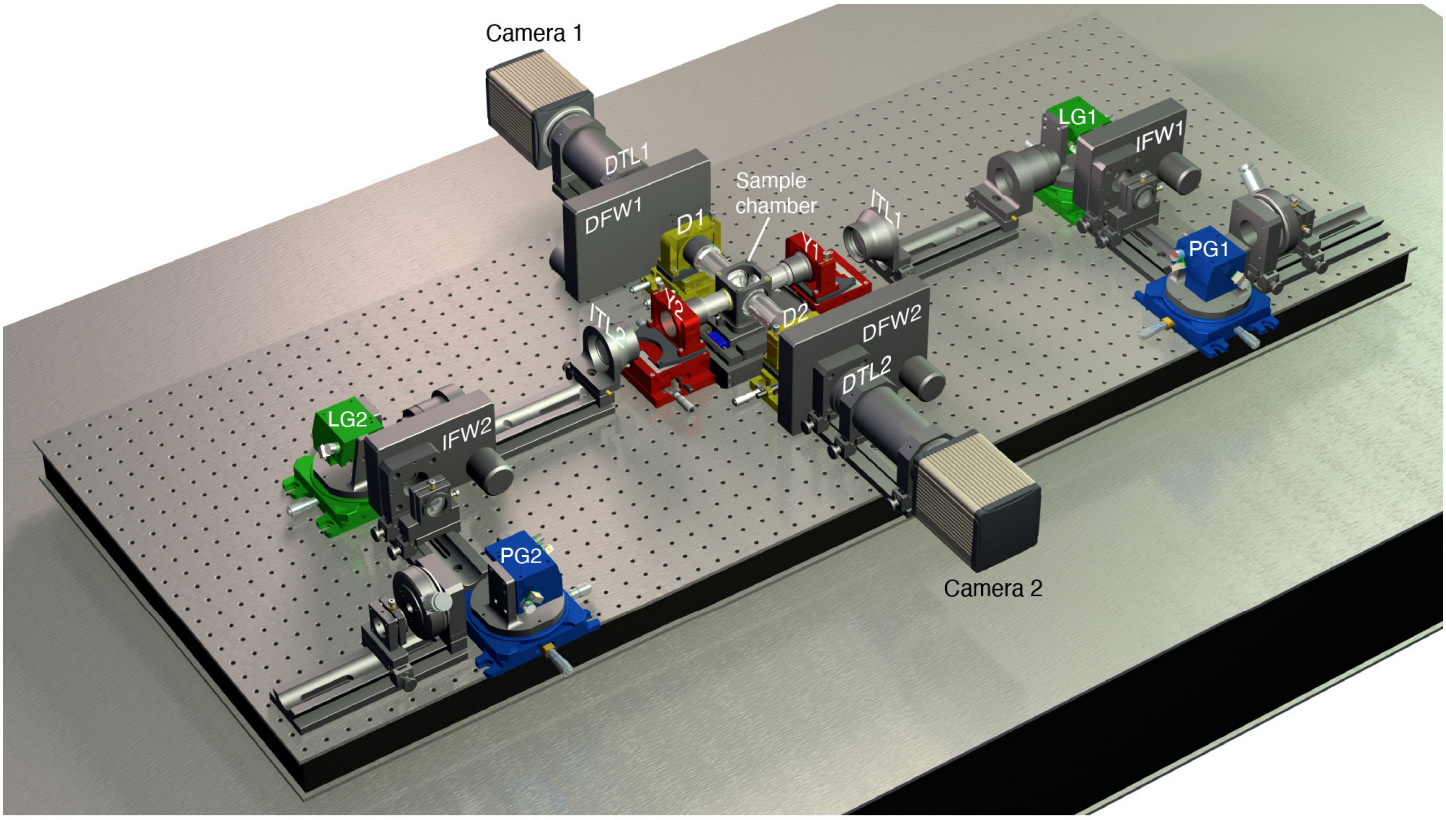

Nature Biotechnology: doi:10.1038/nbt.3708

Supplementary Figure 2 | Digital control of three-dimensional light-sheet orientation

Illustration of the optical design of the microscope sub-system responsible for controlling light-sheet angle β in each illumination arm (only one arm is shown for simplicity). Please see **Supplementary Methods 1** for a detailed discussion and the mathematical description of this degree of freedom.

(**a**) Optical configuration: the pivot galvanometer scanner is positioned between two relay lenses, at a distance of one focal length to each lens, such that the combined system introduces a parallel displacement of the laser beam relative to the optical axis that is converted by downstream optical components into a pivot motion in sample space (light-sheet angle β). The pivoted beam, shown in red, is displaced laterally (along z) relative to the on-axis beam, shown in blue, after the light-sheet galvanometer scanner. While the pivot galvanometer scanner is responsible for controlling the light-sheet angle β, the light-sheet galvanometer scanner controls light-sheet angle α and light-sheet offset I. In order to reduce the footprint of the microscope, dual-axis galvanometer scanners are used in the design of the illumination arms.

(**b**) Pivoted and on-axis beams shown in red and blue, respectively, at the front aperture of the 2nd relay lens. The pivoted beam is displaced along X (θ_x) by the vertical tilting mirror (V) in the pivot galvanometer scanner, and displaced along Z (θ_z) by the lateral tilting mirror (L) in the pivot galvanometer scanner. Cumulatively, θ_x and θ_z result in the angular displacement of the pivot-beam by γ with respect to the on-axis beam at V. The orientation of the pivot-plane, illustrated in shaded red, flips by $(90° - \eta)$ as it exits the dual-axis light-sheet galvanometer scanner, where η is the angle between the shafts of the two scanning mirrors in the light-sheet galvanometer scanner. Note that the drawing is not to scale.

(**c**) The position of the rotation axis (in the context of both α and β) can be changed by translating the light sheet using the degree of freedom I. Here we illustrate this idea for a generic angle θ, but it naturally applies without loss of generality to both α and β.

Nature Biotechnology: doi:10.1038/nbt.3708

Supplementary Figure 2 | Digital control of three-dimensional light-sheet orientation

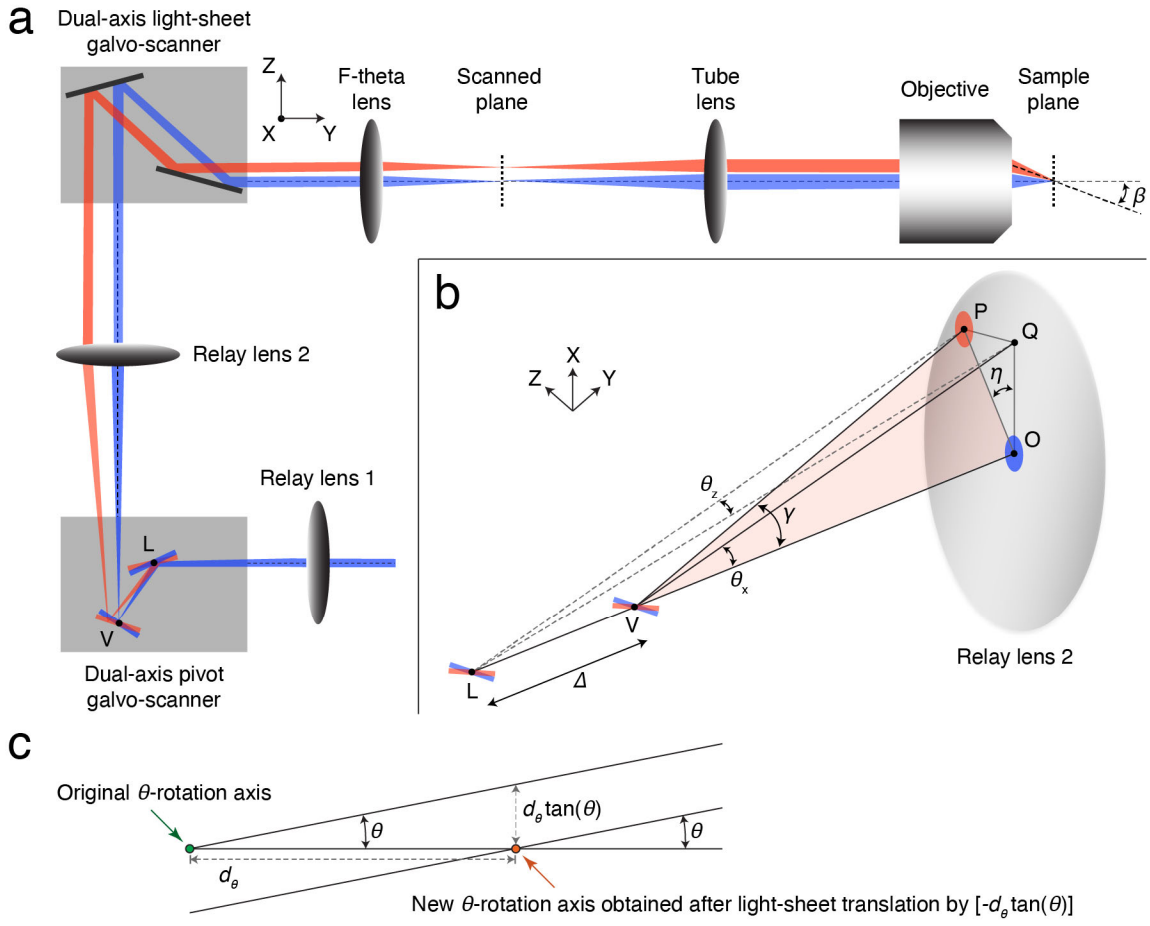

Nature Biotechnology: doi:10.1038/nbt.3708

Supplementary Figure 3 | Side-by-side comparison of focus metrics

Normalized focus curves for the four classes of image quality metrics applied to the four noiseless focus stacks (**Supplementary Fig. 4a**). While most image quality metrics have a concave tent-like response, the following do not: *Normalized Haar wavelet transform Shannon entropy (NHWTSE), Kurthosis (K), Kurtosis of differences (KD), Shannon entropy of histogram (EH)*. Some image quality metrics (e.g. *NHWTSE, K, KD*) have an inverted response on some focus stacks (see arrow marked "*i*"). Other image quality metrics (e.g. *NHWTSE, K*) have a non-unimodal response, reminiscent of a second-order differential response (see arrows marked "*2nd*"). Finally, the focus curves produced by the *EH* metric are noisy, with many local maxima and minima (see arrow marked "*n*").

Nature Biotechnology: doi:10.1038/nbt.3708

Supplementary Figure 3 | Side-by-side comparison of focus metrics

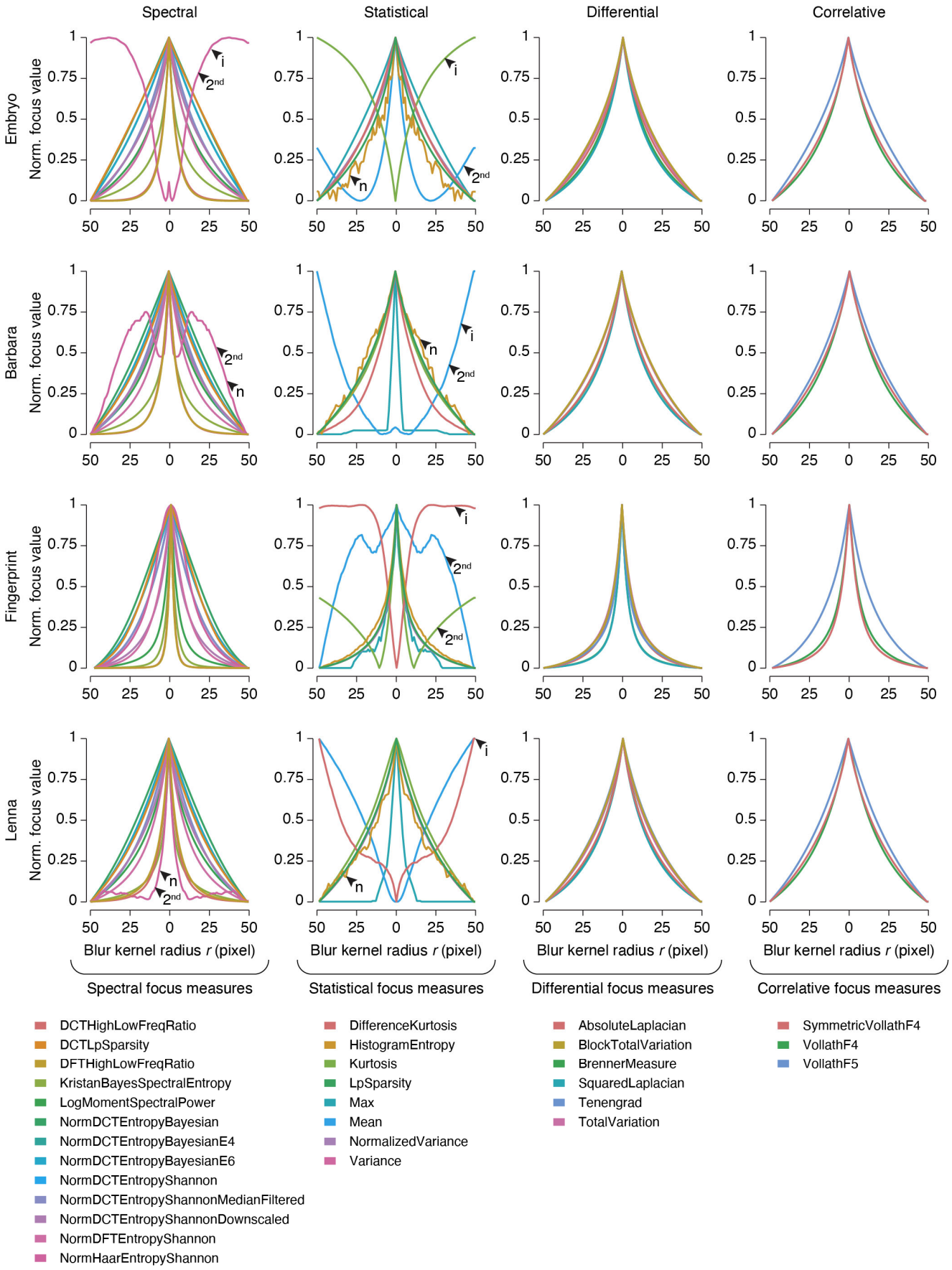

Nature Biotechnology: doi:10.1038/nbt.3708

Supplementary Figure 4 | Synthetic benchmarks for evaluating focus metrics

(**a**) The synthetic benchmark is based on 24 focus stacks derived from 4 images "Lenna", "Fingerprint", "Barbara", and "Embryo". The last image ("Embryo") is a light-sheet microscopy recording of Drosophila embryo. For each image we created one noiseless focus stack as well as five additional focus stacks with noise levels 10%, 20%, 30%, 40% and 50%.

(**b**) Normalized focus curves produced by the four best measures (see **Supplementary Table 1**) for all six "Embryo"-based focus stacks. The plots are not mirror symmetrical with respect to $r = 0$ because image noise is applied independently for each computation and data point. The use of a mirrored axis for radius r is motivated by our intent to reproduce the familiar symmetrical appearance of focus curves for the purpose of this visualization.

(**c**) Example images for three "Embryo"-based focus stacks (10%, 30% and 50% noise levels). Note that, at a noise level of 50%, it is difficult for the human observer to assess the difference in focus quality of these images. Yet, although the corresponding focus quality curves computed by the DCT-based focus metrics are very noisy, they have a distinct maximum.

Nature Biotechnology: doi:10.1038/nbt.3708

Supplementary Figure 4 | Synthetic benchmarks for evaluating focus metrics

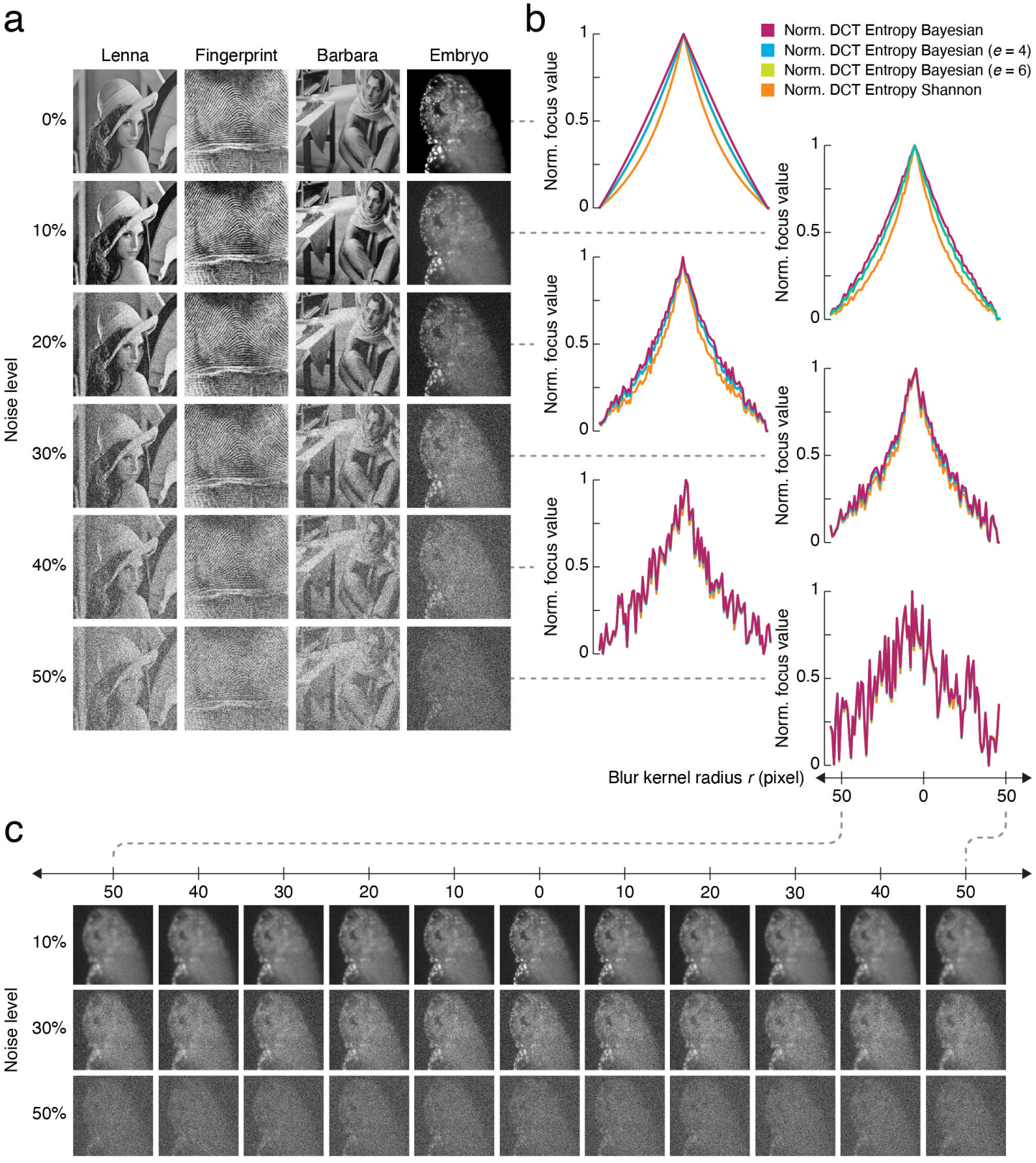

Nature Biotechnology: doi:10.1038/nbt.3708

Supplementary Figure 5 | Application of DCTS focus metric to light-sheet image data

Demonstration of application of the DCTS focus metric to a focus stack acquired for an image plane recorded in a *Drosophila* embryo. The focus stack covers the defocus range −25 µm to +25 µm in steps of 1 µm.

(**a**) Five example images (−20 µm, −10 µm, 0 µm, 10 µm and 20 µm defocus) taken from the focus stack.

(**b**) Close-up of a small image region shown for multiple focus settings within +/- 7 µm of the optimal focus.

(**c**) Corresponding focus curve produced by the DCTS image quality metric.

Scale bars, 50 µm (a), 20 µm (b).

Nature Biotechnology: doi:10.1038/nbt.3708

Supplementary Figure 5 | Application of DCTS focus metric to light-sheet image data

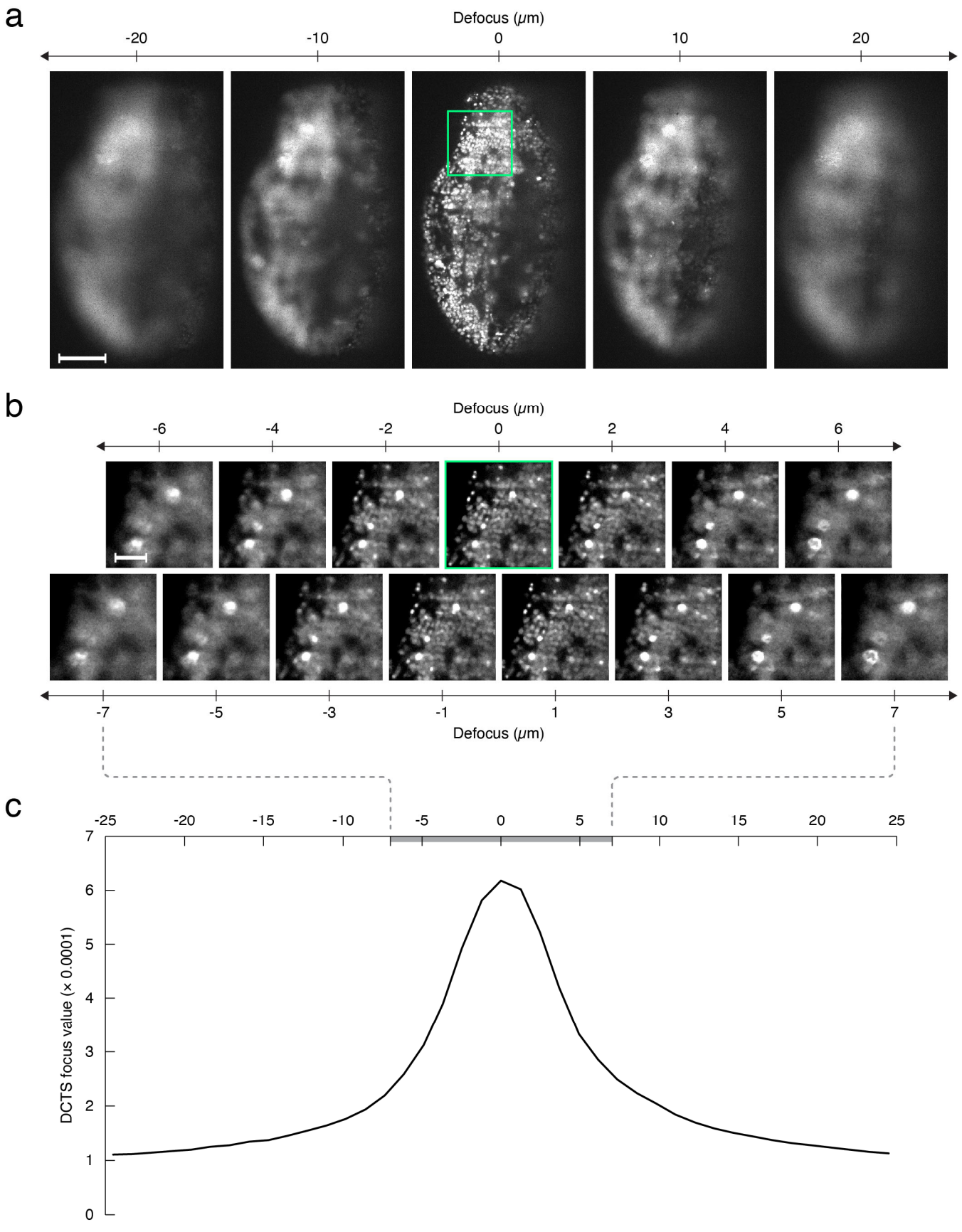

Nature Biotechnology: doi:10.1038/nbt.3708

Supplementary Figure 6 | Recovering focus information for image data with challenging properties

Application of the DCTS focus metric to three difficult examples from the light-sheet focus stack benchmark.

In example 1 (top, "strong light scattering"), the DCTS focus metric was applied to an image acquired deep inside a nuclei-labeled *Drosophila* embryo (depth of 100 µm, corresponding to the geometrical center of the embryo). In this scenario, image quality is severely degraded by light scattering both in the illumination and detection process. Only the left half of the image contains features the microscope is capable of resolving at reasonably high quality. The challenge in this particular scenario is that only a very small fraction of the signal in the image does not suffer from light scattering and that the vast majority of the collected signal thus does not carry information useful for assessing focus quality. Therefore the focus metric has very little usable signal to achieve perfect focusing and permit optimal imaging of those regions that are not strongly degraded by light scattering. Enlarged views of small regions in the image plane (green and magenta rectangles indicated on the full image shown to the left) are shown for several defocus settings (optimal focus setting, 1 µm defocus, 2 µm defocus and 3 µm defocus). A defocus of 1 µm is hardly noticeable by eye but is sufficient to blur the space between cells relative to the image representing the optimal focus setting (see arrows indicating either the existence or lack of a gap between neighboring cells). The focus curve for the entire image plane is shown to the right.

In example 2 (middle, "low signal-to-noise ratio), the DCTS focus metric was applied to an image of a nuclei-labeled *Drosophila* embryo acquired with low laser power (resulting in high noise). Also in this case, a small amount of defocus is sufficient to blur nuclei boundaries (see arrows).

In example 3 (bottom, "autofluorescence"), the DCTS focus metric was applied to an image of an unlabeled *Drosophila* embryo, which contains auto-fluorescence as the only signal source. Very few structures (primarily the vitelline membrane, see arrows) can be used for focusing. Nevertheless, the DCTS focus curve for this image is remarkably monotonous and noise-free.

For clarity, the focus curves are normalized from their original range [min,max] to the normalized range [0,1].

Scale bars, 50 µm (full image, green enlarged views), 10 µm (magenta enlarged views).

Nature Biotechnology: doi:10.1038/nbt.3708

Supplementary Figure 6 | Recovering focus information for image data with challenging properties

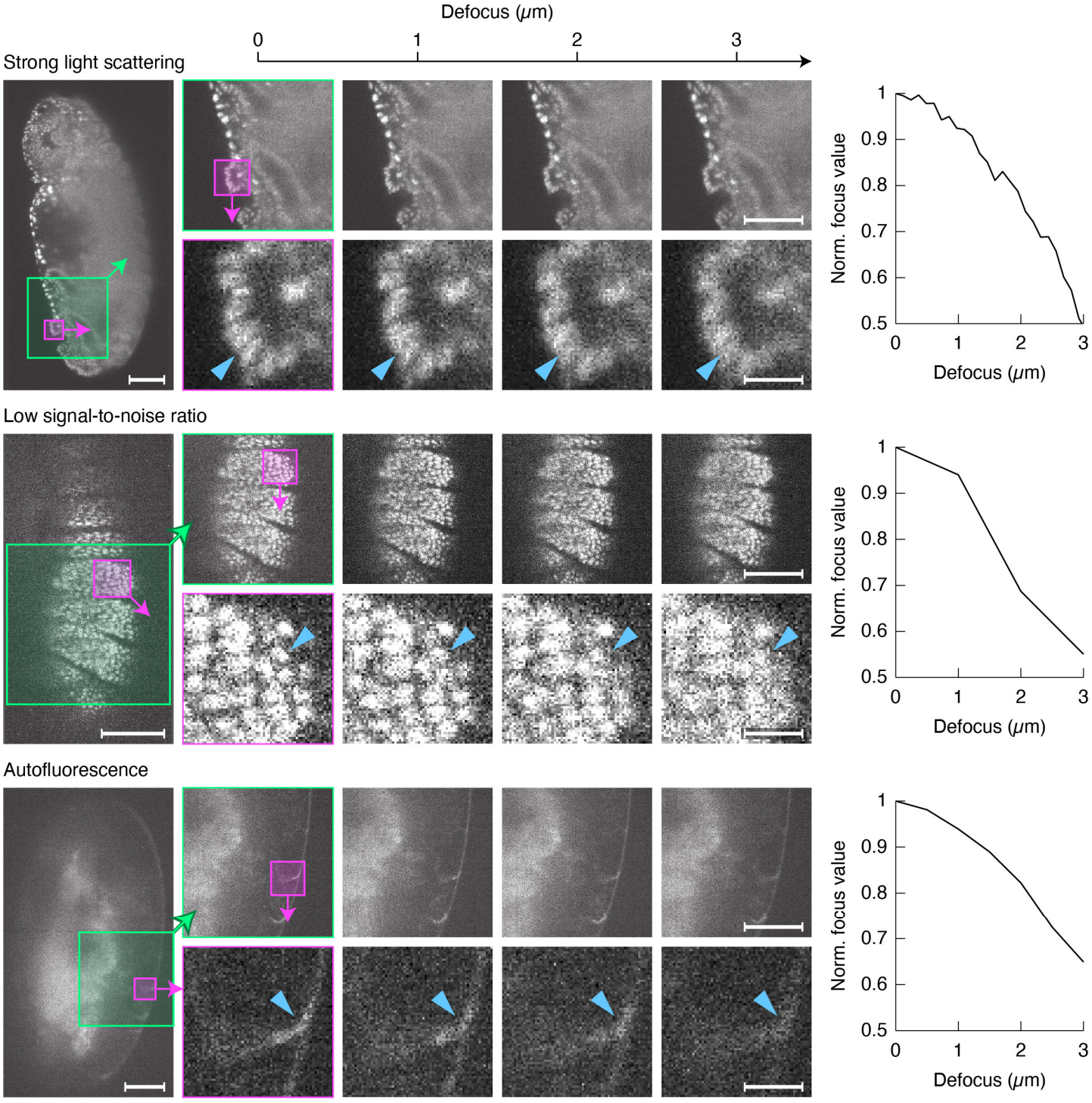

Nature Biotechnology: doi:10.1038/nbt.3708

Supplementary Figure 7 | Minimizing focus metric errors by using low-pass filtering

Effect of low-pass filtering on the median error of the best spectral image quality metric (Normalized DCT Shannon entropy).

(**a**) Median error as a function of low-pass filter diameter for the focus stacks included in the synthetic benchmark. The optimal low-pass filtering diameter is 6 pixels.

(**b**) Median error as a function of low-pass filter diameter for the focus stacks included in the light-sheet microscopy benchmark. The optimal low-pass filtering diameter is 3 pixels.

Nature Biotechnology: doi:10.1038/nbt.3708

Supplementary Figure 7 | Minimizing focus metric errors by using low-pass filtering

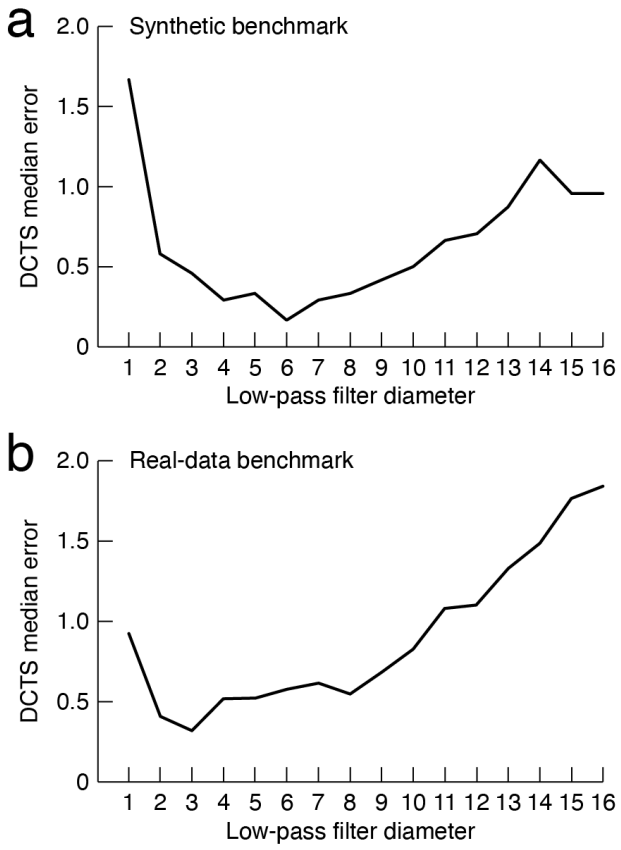

Nature Biotechnology: doi:10.1038/nbt.3708

Supplementary Figure 8 | Degrees of freedom and workflow of spatiotemporally adaptive imaging

(**a**) Schematic illustration of the ten state variables relevant for spatiotemporally adaptive imaging: D_1, D_2, I_1, I_2, Y_1, Y_2, α_1, α_2, β_1, β_2 (shown with their relative orientations).

(**b**) The framework for spatiotemporally adaptive imaging monitors and optimizes image quality in reference planes distributed throughout the three-dimensional imaging volume (labeled z_0 to z_7 in the example here). When imaging large, partially opaque specimens some of these reference planes are mainly relevant for the first detection arm (associated with D_1), whereas others are mainly relevant for the second detection arm (associated with D_2). A subset of reference planes typically located near the center of the specimen (also called "sync planes", labeled z_{s-1} and z_s in the example here) is associated with both detection arms and the related degrees of freedom are subject to a set of constraints that differs from those used in the rest of the volume. Measurements performed at these planes are used to ensure spatial continuity throughout the imaging volume.

(**c**) Conceptual illustration of the process workflow in spatiotemporally adaptive imaging. In order to minimize photo-bleaching, photo-toxicity and impact on temporal resolution in the imaging experiment, image acquisition related to AutoPilot measurements is kept to a minimum and distributed in time, using the microscope's idle time after acquiring the primary image data associated with each time point in a time-lapse experiment. When a full measurement cycle has been completed, the control framework computes and applies a global update to the microscope system state, thereby maintaining optimal image quality and adapting to spatiotemporal optical changes in time-lapse imaging.

Nature Biotechnology: doi:10.1038/nbt.3708

Supplementary Figure 8 | Degrees of freedom and workflow of spatiotemporally adaptive imaging

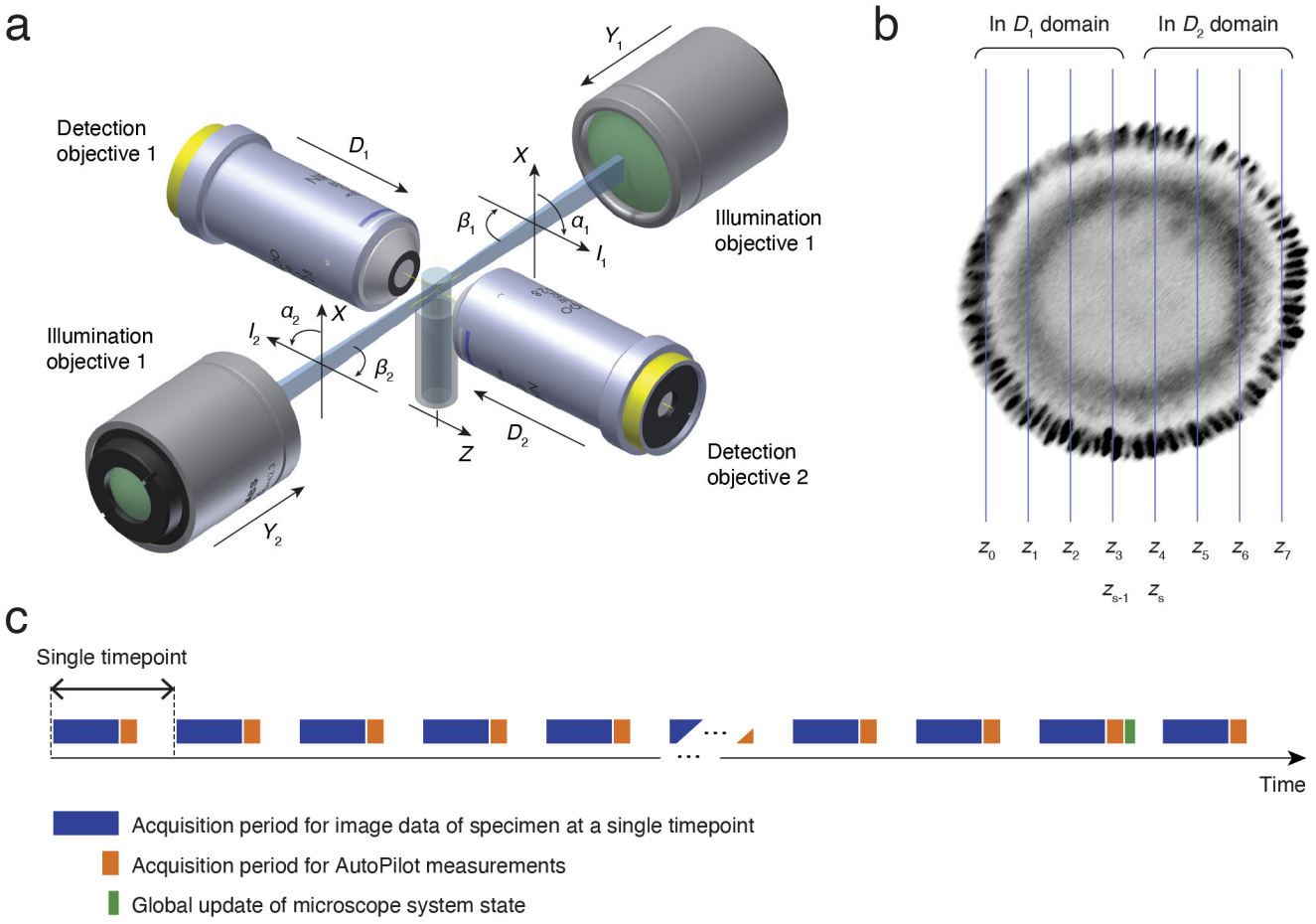

Nature Biotechnology: doi:10.1038/nbt.3708

Supplementary Figure 9 | General optimization theory for spatiotemporally adaptive imaging

Illustration of key concepts underlying the general optimization theory for spatiotemporally adaptive imaging. For simplicity and readability, these illustrations consider only four (D_1, D_2, I_1 and I_2) out of the in total ten degrees of freedom (D_1, D_2, I_1, I_2, Y_1, Y_2, α_1, α_2, β_1 and β_2) used in our framework for spatiotemporally adaptive imaging.

(**a**) Constraint graph representation of the focusing constraints for D_1, D_2, I_1 and I_2 in a two-color (λ_0 and λ_1), three-plane (z_0, z_1 and z_2) configuration. Variables representing light-sheet offset positions (I_1 and I_2) are linked via defocus measurements observed relative to the detection objective positions (D_1 and D_2). Since the piezo positioners attached to the detection objectives are the most precise spatial measurement devices in the microscope and thus serve as spatial references, the detection objectives are maintained at constant positions for all reference planes (z_0, z_1 and z_2) in a given color channel (λ_0 and λ_1). The two color channels are linked by the requirement that the center of mass of the positions of the detection objectives (but not their individual, absolute positions) are the same for different color channels.

(**b**) The focusing constraints can be compiled into a single matrix that describes the linear relationships between the state variable S and the defocus and constraint violation observations F. The values $F_{u,v}$ are defocus measurements and the values V_k constraint violation correction terms.

(**c**) Illustration of the system anchoring constraint (fixed center of mass of the positions of the detection objectives), which is required to prevent drift of the center of mass of the system. For clarity and simplicity, this constraint is omitted in panel (a).

(**d**) If the fluorescence signal is weak or nonexistent in any reference plane and at any time during the experiment (e.g. in a sample region that does not or not yet express a genetically encoded fluorescence marker, or in a sample region that is not yet occupied by cells but will become populated later in the course of a large-scale cell movement event) the image quality metric responds below a pre-defined threshold and special substitution constraints are used to approximate the missing information. In the example shown here, light-sheet offset positions are set to the value at one neighboring plane. In practice, we set the value to the average values of the neighboring reference planes unless the plane considered is the first or last reference plane.

Nature Biotechnology: doi:10.1038/nbt.3708

Supplementary Figure 9 | Generalized optimization theory for spatiotemporally adaptive imaging

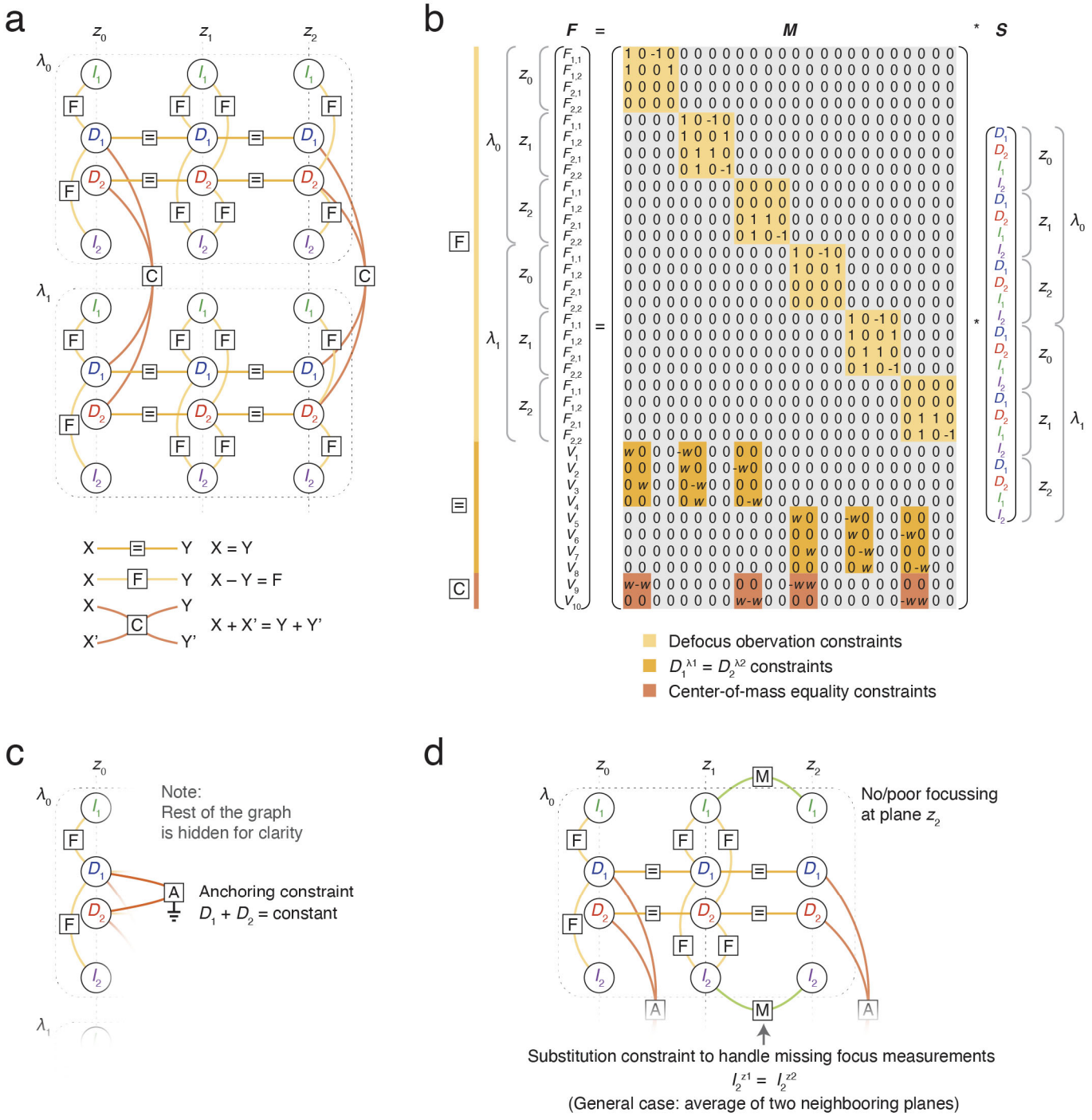

Nature Biotechnology: doi:10.1038/nbt.3708

Supplementary Figure 10 | Online perturbation benchmark of adaptive imaging performance

(**a**) Volumetric DCTS focus value shown as a function of time during an adaptive live imaging experiment of *Drosophila* embryogenesis, in which perturbations of detection objective positions and light-sheet offsets were introduced manually. Each of the 9 perturbations introduces a temporary dip in focus quality (blue bars), which is subsequently restored through appropriate countermeasures initiated by the automated framework for spatiotemporally adaptive imaging.

(**b**) Four degrees of freedom of the microscope (D_1, D_2, I_1, I_2) shown as a function of time for reference plane z_2. All corrections visualized in this plot are measured relative to the position value of D_1. We note that D_1 was set to a constant value in this experiment (serving as the "anchor" of the system, in contrast to D_2, I_1 and I_2 which were allowed to undergo corrections) to simplify the interpretation of the system response without affecting the practical value of this benchmark experiment.

(**c**) Maximum-intensity projection (left) and time series of an enlarged view of a small region of the embryo directly before and shortly after the fourth perturbation (right). The image sequence highlights the quadrant of the sample illuminated by objective O_4 and imaged with objective O_2. Optimal focus quality is restored within 0.5 min for the shown quadrant and within 2 min for the entire volume (see (a)).

(**d**) As in panel (c) but for the fifth perturbation. The image sequence highlights the quadrant of the sample illuminated by objective O_4 and imaged with objective O_2. Optimal focus quality is restored within 1 min for the shown quadrant and within 4 min for the entire volume (see (a)).

(**e**) As in panel (c) but for the ninth perturbation, which is the most severe system perturbation included in this benchmark. The two image sequences highlight regions in the quadrant of the sample illuminated by objective O_4 (right) and O_3 (left) and imaged with objective O_1.

Image sequences for quadrants illuminated by objective O_4 (right) and O_3 (left) and imaged from objective O_1. The simultaneous shifts of D_1 and I_2 by 8 μm each in the same direction cancel each other out for the quadrant illuminated by O_3 and imaged by O_1. Recovery from the fairly dramatic loss of focus quality seen in the image data for the quadrant illuminated by O_4 and imaged by O_1 takes 16 time points locally and 22 time points for the entire volume (see (a)).

Scale bars, 50 μm (full images in c-e), 20 μm (enlarged views in c-e).

Nature Biotechnology: doi:10.1038/nbt.3708

Supplementary Figure 10 | Online perturbation benchmark of adaptive imaging performance

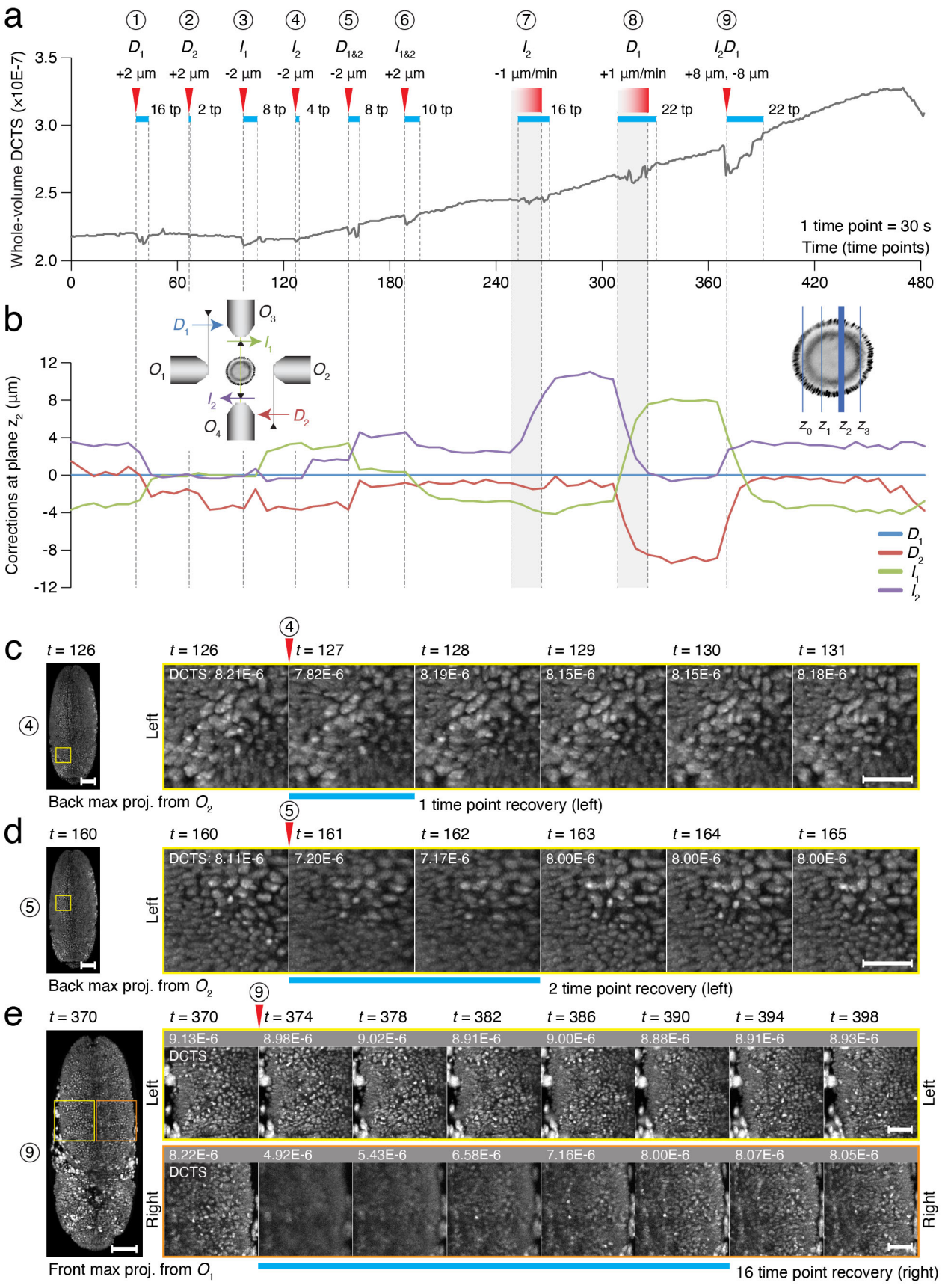

Nature Biotechnology: doi:10.1038/nbt.3708

Supplementary Figure 11 | Analysis and system calibration of light-sheet angles alpha and beta

In order to calibrate our system and evaluate the accuracy of our methodological framework in determining the three-dimensional geometry of the light-sheet *in vivo* (measuring light-sheet angles alpha and beta), we (1) systematically imposed various light-sheet angles alpha and beta while imaging a *Drosophila melanogaster* embryo and (2) measured these angles from the acquired image data using our algorithm for robust image-based estimation of three-dimensional light-sheet geometry. The two graphs provided in this figure show the relationship between imposed and measured alpha and beta angles as a function of imaging depth in the sample (considering the two depths indicated in the cartoon to the bottom right).

Left: As expected from the ellipsoidal symmetry of the specimen, the light-sheet angle α does not depend on imaging depth (or, in other words, on the geometrical location where the light sheet enters the specimen). For simplicity, data points are plotted without a depth-dependent color code in this case. The average absolute residual error for the linear regression is 0.14º (R^2 = 0.954). Right: By contrast, the effective light-sheet angle β depends on imaging depth, leading to a ~2-degree difference in measured beta angles for the two diametrically opposed reference locations in the specimen. This behavior matches theoretical expectations (as discussed in detail in **Supplementary Methods 5**), specifically it is quantitatively and qualitatively in good agreement with the combined effects of (i) the difference in refraction angle of the incident light sheet at the two respective entry points to the specimen and (ii) the difference in bending angle of the detection focal plane at the respective depths in the specimen. The average absolute residual error for the linear regression is 0.21º (R^2 = 0.958 and 0.908 for data sets shown in orange and green, respectively). Overall, we observe an affine relationship between imposed and measured angles, which can be used to calibrate the system.

Nature Biotechnology: doi:10.1038/nbt.3708

Supplementary Figure 11 | Analysis and system calibration of light-sheet angles alpha and beta

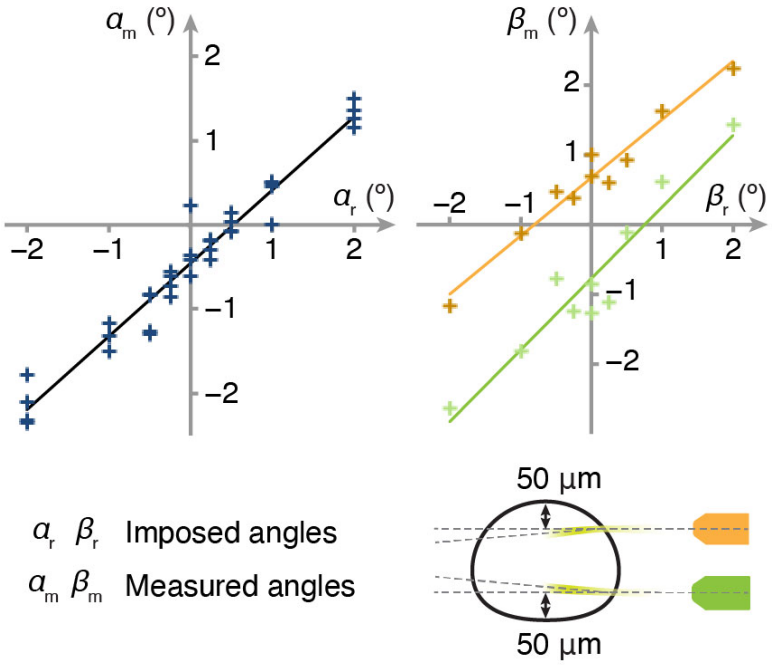

Nature Biotechnology: doi:10.1038/nbt.3708

Supplementary Figure 12 | Whole-brain functional imaging using the adaptive imaging framework

(**a**) Rapid spatial adaptation of the microscope to the brain of a larval zebrafish just before the onset of a whole-brain functional imaging experiment using calcium indicators. Illustration of the time line of system optimization: three rounds of system optimization are performed with successively finer system parameter resolution, starting with 4 μm steps, followed by 2.4 μm steps, and finally using 0.8 μm steps. Each optimization round is performed globally for all degrees of freedoms and all reference planes inside the fish brain.

(**b**) Example curves showing the focus-dependency of the image quality metric for light sheet 2 at reference plane z_4 during consecutive rounds of microscope system state optimization.

(**c**) Example images demonstrating improvement in image quality in the course of microscope system state optimization. Starting with a microscope in a state of misalignment, the automated adaptive imaging framework fully recovers high spatial resolution throughout the specimen volume within 40 seconds, as demonstrated at the example of the optic tectum region shown in the enlarged view to the right (before = image quality prior to the first iteration of system optimization, after = image quality after the third iteration of system optimization).

(**d**) Experimental analysis of optimal microscope parameter settings during whole-brain functional imaging using the AutoPilot framework. Left: optimal spatiotemporal adaptation of the offset of light sheet 2 in five different spatial reference locations, using one full system update every 10 min. Right: optimal light-sheet angles α and β determined as a function of depth at the beginning of the functional imaging experiment. In order to minimize time spent on AutoPilot measurements and maximize the effectiveness of AutoPilot corrections, only the core set of AutoPilot system parameters (D_i, I_i) are optimized during high-speed functional imaging. This approach corrects for the most important perturbations of the optical conditions (focusing on spatiotemporally adaptive light-sheet offset corrections) and reserves 98% of instrument time for sustained high-speed, whole-brain image acquisition.

Scale bars, 50 μm (magenta panels in c), 20 μm (green panels in c).

Nature Biotechnology: doi:10.1038/nbt.3708

Supplementary Figure 12 | Whole-brain functional imaging using the adaptive imaging framework

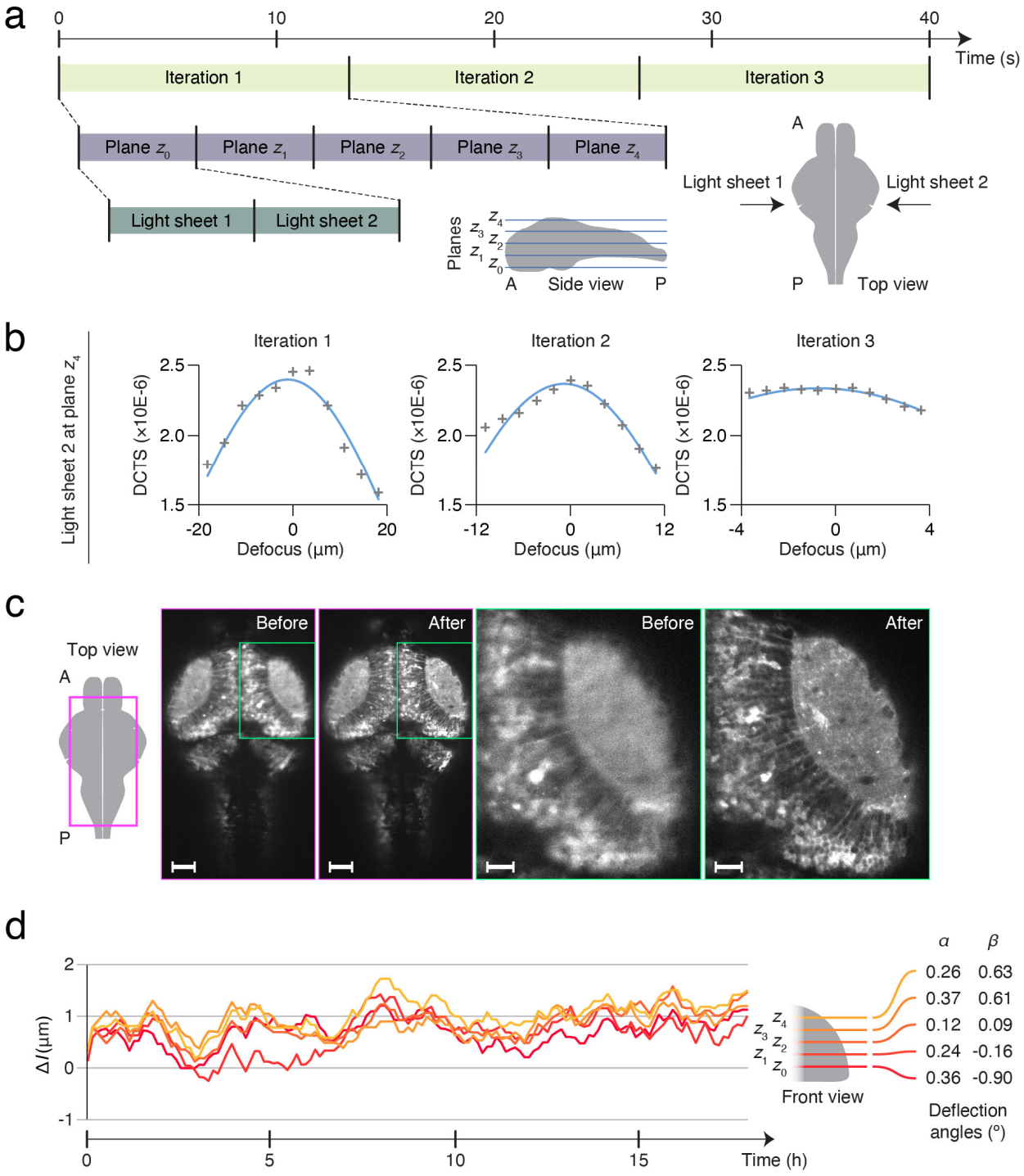

Nature Biotechnology: doi:10.1038/nbt.3708

Supplementary Figure 13 | Spatiotemporally adaptive imaging of *Drosophila* embryonic development

Time-course of whole-volume DCTS focus metric and microscope system parameters during spatiotemporally adaptive imaging of Drosophila embryonic development.

(**a**) Volumetric (whole-animal) DCTS focus value as a function of time, annotated with developmental phases during *D. melanogaster* embryonic development. Note that in contrast to the systematic DCTS measurements performed locally on focus stacks to optimize the system state, the whole-volume DCTS values reported here inform about changes in image content caused by the progression of embryonic development rather than about the quality of the system alignment itself.

(**b**) Temporal corrections of the degrees of freedom D_1, D_2, I_1 and I_2 at the reference planes z_0 to z_5. Note that corrections required for maintaining optimal image quality throughout the embryo vary both in time and space. No changes are applied to D_1, since this degree of freedom is used to anchor the system and prevent parameter drift over time.

Nature Biotechnology: doi:10.1038/nbt.3708

Supplementary Figure 13 | Spatiotemporally adaptive imaging of Drosophila embryonic development

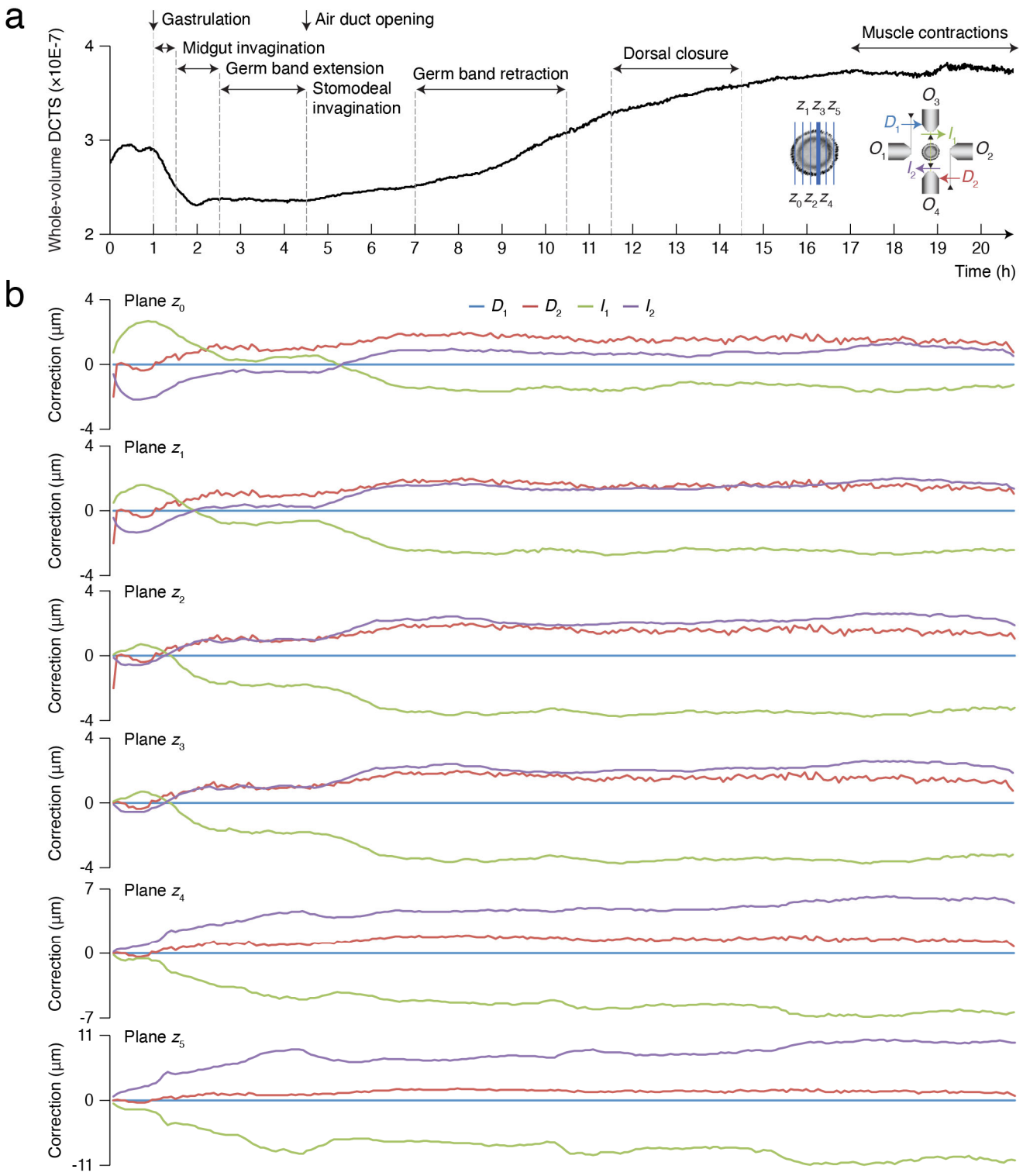

Nature Biotechnology: doi:10.1038/nbt.3708

Supplementary Figure 14 | Improved resolution and signal strength in *Drosophila* embryos

In order to quantify improvements in spatial resolution and signal strength obtained with adaptive imaging, we comparatively analyzed images recorded in adaptively corrected (first column) and uncorrected (second column) microscope states, respectively, in a *Drosophila* embryo at 21 hours after egg laying. Since the biological specimen does not contain true point sources of fluorescence, we determined differences in resolution from line profiles crossing boundaries of fluorescently labeled cell nuclei (third column). These nuclei boundaries represent relatively sharp edges in the images (in particular compared to the theoretical, diffraction-limited resolution the microscope is capable of in a best-case scenario) and can be used to obtain lower-bound estimates of the ratios of point-spread function sizes in corrected and uncorrected microscope states (quantitative results shown in fourth column, see **Supplementary Methods 6** for methodological details and a mathematical derivation). Since this computation yields lower-bound estimates, the improvements in spatial resolution achieved by adaptive imaging are at least as large as the factors shown in the fourth column of this figure.

We provide three representative examples each at three different imaging depths (see schematic illustrations to the left showing a top view of the *Drosophila* embryo and indicating the respective locations of the image planes in dark green). The panels next to the images acquired in adaptively corrected and uncorrected microscope states (first and second columns) show intensity profiles and derivatives of the intensity profiles (third and fourth columns) corresponding to the light green lines on the image panels. The resolution improvements observed in the image data are confirmed by the sharper edges and higher derivatives measured along the respective intensity profiles. The average increase in resolution across all imaging depths and data points is 2.36, the median increase is 2.11, and the maximum increase is 3.75 (fourth column). As a direct result of microscope adaptation to the optical properties of the specimen, signal strength is improved as well. The average increase in signal strength is 1.57, the median increase is 1.50, and the maximum increase is 2.03 (third column). We note that the profiles were chosen to intersect cell nuclei boundaries at a right angle because the estimation of the improvement in spatial resolution is most accurate when analyzing features with sharp boundaries in the image data (**Supplementary Methods 6**).

Scale bars, 5 μm.

Nature Biotechnology: doi:10.1038/nbt.3708

Supplementary Figure 14 | Improved resolution and signal strength in *Drosophila* embryos

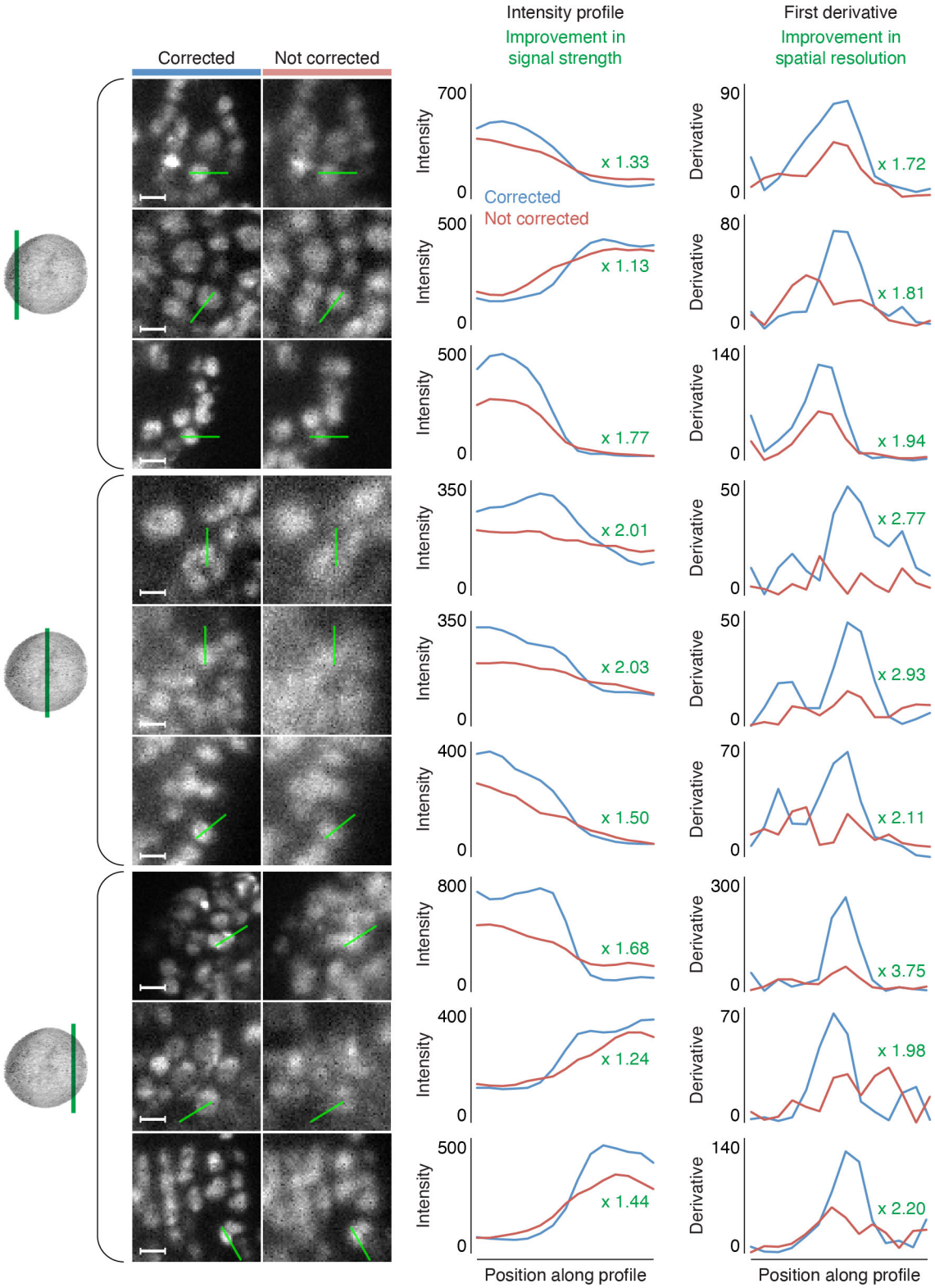

Nature Biotechnology: doi:10.1038/nbt.3708

Supplementary Figure 15 | Improving resolution and signal strength in zebrafish embryos

Similar to the analysis shown in **Supplementary Fig. 14**, we quantified improvements in spatial resolution and signal strength obtained with adaptive imaging also for our live imaging experiments in developing zebrafish embryos. We comparatively analyzed images recorded in adaptively corrected (first column) and uncorrected (second column) microscope states, respectively, in a zebrafish embryo at the end of epiboly. Please see **Supplementary Fig. 14** and **Supplementary Methods 6** for a description of this analysis and for details on the computation of increases in spatial resolution from the ratio of maxima in the first derivatives of line profiles across sharp edges in the image data.

We provide two representative examples each at five different imaging depths (see schematic illustrations to the left showing a side view of the zebrafish embryo and indicating the respective locations of the image planes in dark green). The panels next to the images acquired in adaptively corrected and uncorrected microscope states (first and second columns) show intensity profiles and derivatives of the intensity profiles (third and fourth columns) corresponding to the light green lines on the image panels. The resolution improvements observed in the image data are confirmed by the sharper edges and higher derivatives measured along the respective intensity profiles. The average increase in resolution across all imaging depths and data points is 3.03, the median increase is 2.83, and the maximum increase is 5.86 (fourth column). As a direct result of microscope adaptation to the optical properties of the specimen, signal strength is improved as well. The average increase in signal strength is 2.06, the median increase is 1.50, and the maximum increase is 4.78 (third column). We note that the profiles were chosen to intersect cell nuclei boundaries at a right angle because the estimation of the improvement in spatial resolution is most accurate if the true boundary is as sharp as possible (**Supplementary Methods 6**).

Scale bars, 5 μm.

Nature Biotechnology: doi:10.1038/nbt.3708

Supplementary Figure 15 | Improving resolution and signal strength in zebrafish embryos

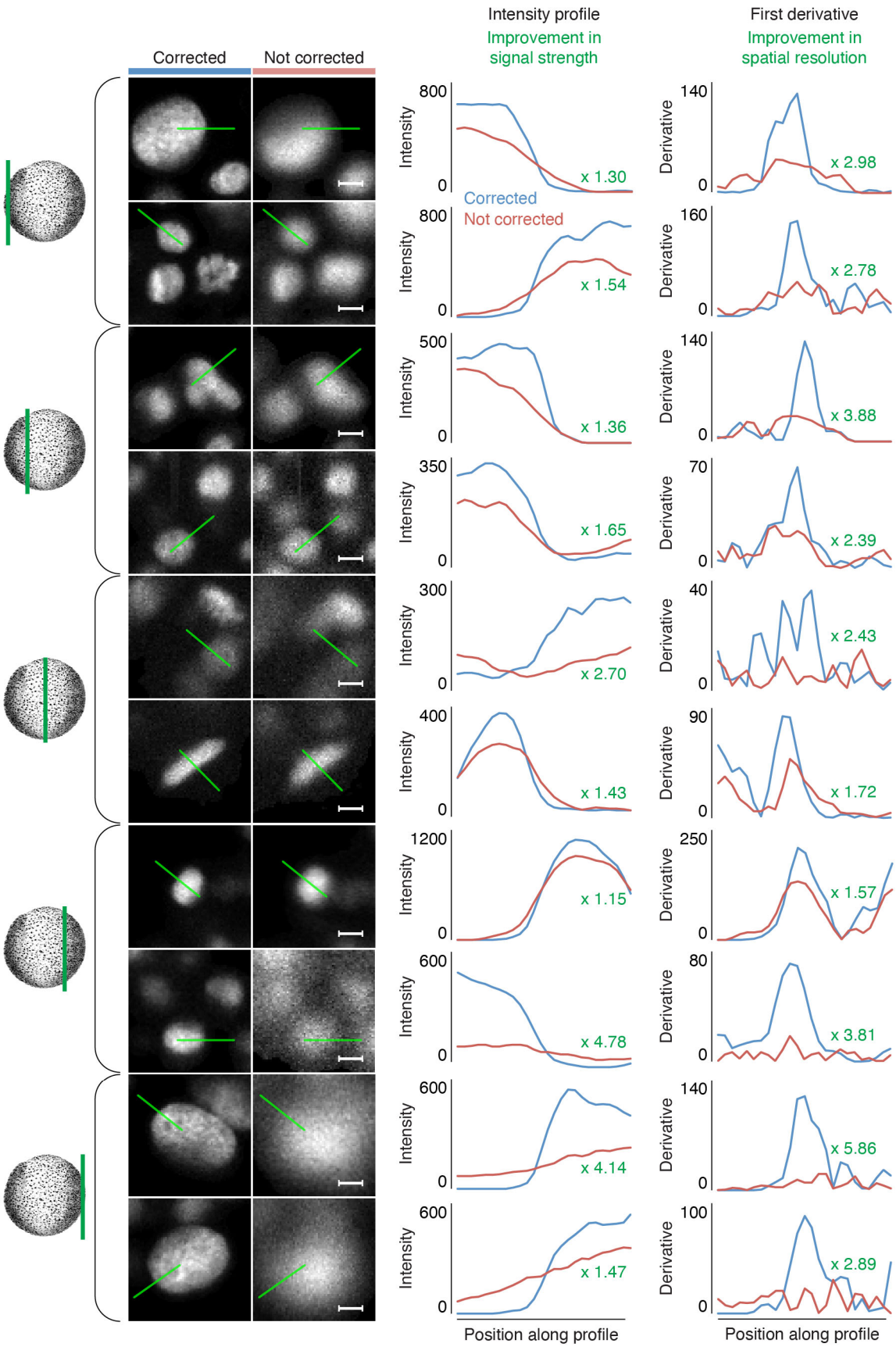

Nature Biotechnology: doi:10.1038/nbt.3708

Supplementary Figure 16 | Adaptive axial positioning of the light-sheet waist

The framework for spatiotemporally adaptive imaging digitally controls the degrees of freedom Y_1 and Y_2, which enable adaptation of the axial position of the light-sheet waist to local geometrical and optical properties of the sample.

By adjusting the axial position of the light sheet to the geometry and fluorescence signal distribution of the sample, the waist of the light sheet can be positioned to optimize axial resolution across the optical section. This is demonstrated in this figure at the example of a nuclei-labeled *Drosophila melanogaster* embryo with a diameter of 200 μm (**a**). Each of the microscope's two light sheets is responsible for imaging one lateral half of the embryo in high quality and is thus engineered with a Rayleigh length of 50 μm (resulting in an effective field-of-view of 100 μm per light sheet; for simplicity only the light sheet from one illumination arm is shown in panel (a). The optimal axial position of the light-sheet waist varies with the location of image plane (**b**) and is estimated by determining the position at which the DCTS metric is highest. Example DCTS curves are shown for three different depths in the embryo (**c**, **d**, **e**). Image contrast and spatial resolution are substantially improved by optimizing the axial position of the light-sheet waist (**f**), restoring cellular resolution in many regions of the embryo (**g**). The comparison of image quality for an optimized waist position vs. a sub-optimal waist position shown in panel (f) considers a microscope design that is not capable of adapting light-sheet waist positions as a function of imaging depth (resulting in deviations up to 50 μm from the optimal position across the *Drosophila* embryo).

Scale bars, 10 μm (f).

Nature Biotechnology: doi:10.1038/nbt.3708

Supplementary Figure 16 | Adaptive axial positioning of the light-sheet waist

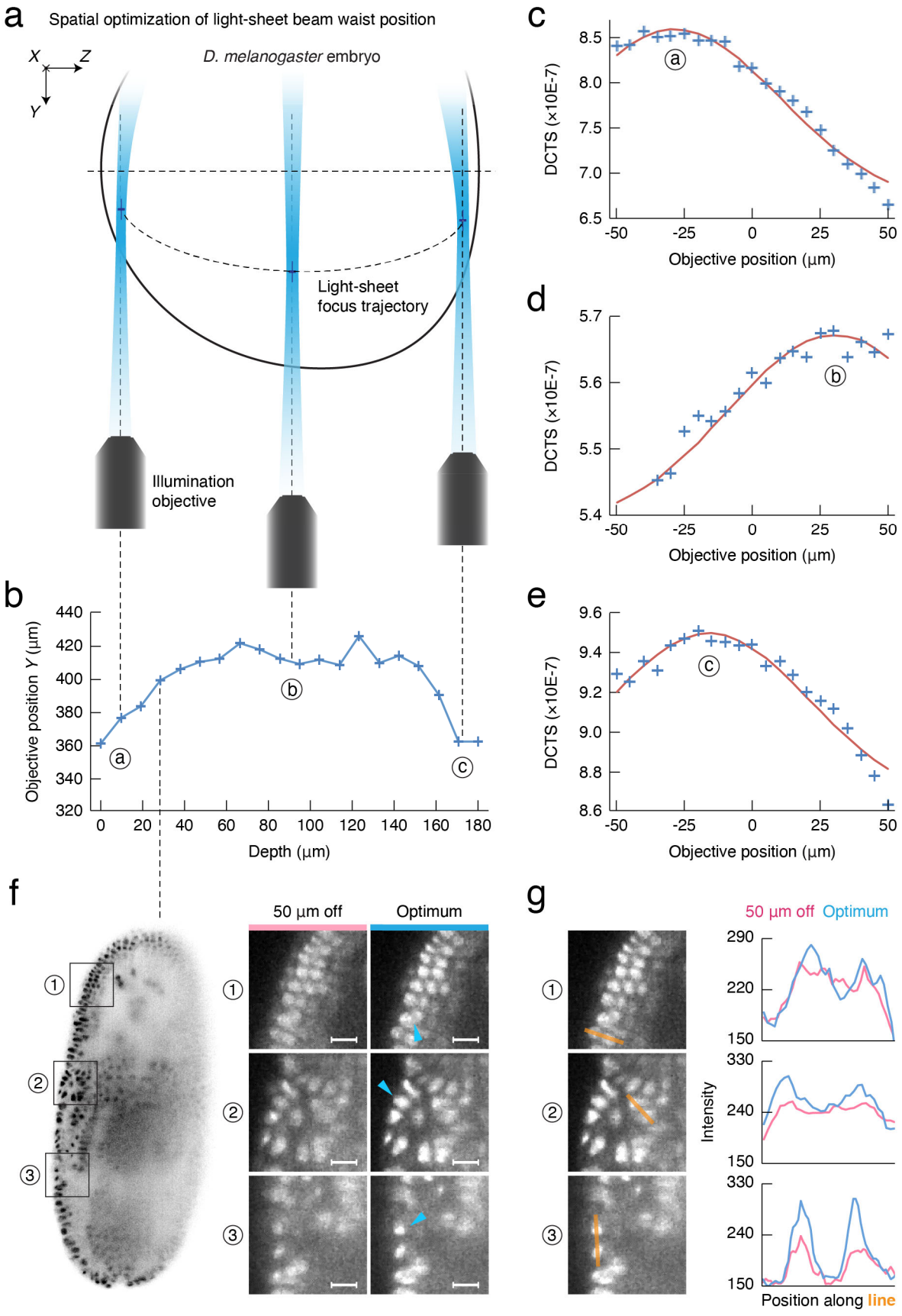

Nature Biotechnology: doi:10.1038/nbt.3708

Supplementary Figure 17 | Spatial dependency of light-sheet angle beta in a *Drosophila* embryo

Light-sheet angles α and β measured as a function of depth in a live *Drosophila melanogaster* embryo. Angle measurements are provided separately for each of the two light sheets (light sheet 1 and 2) and relative to each of the two detection systems (camera 1 and 2). Three-dimensional light-sheet orientation was determined at 18 different depths, using 18 reference planes with a pair-wise spacing of 10 µm. The total size of the embryo along the dimension defined by the detection axes is 200 µm.

As expected from the ellipsoidal symmetry of the embryo, the deflection angle α is effectively constant in space for each pairwise combination of light sheet and detection arm. The graphs also show that the initial (manual) α setting of light sheet 2 deviated by 0.4° from an optimal alignment. This mismatch was automatically detected and corrected by the framework for spatiotemporally adaptive imaging. In contrast to the angle α, the light-sheet angle β strongly depends on imaging depth and exhibits mirror-symmetrical behavior along the two detection paths. Considering the mismatch in average refractive index between embryo and surrounding medium, the depth-dependency of β observed in these graphs can be qualitatively and quantitatively understood with a ray optics model of the light path through specimen and medium (see **Supplementary Methods 5** for details on this model and the two main optical effects that modulate β).

Nature Biotechnology: doi:10.1038/nbt.3708

Supplementary Figure 17 | Spatial dependency of light-sheet angle beta in a *Drosophila* embryo

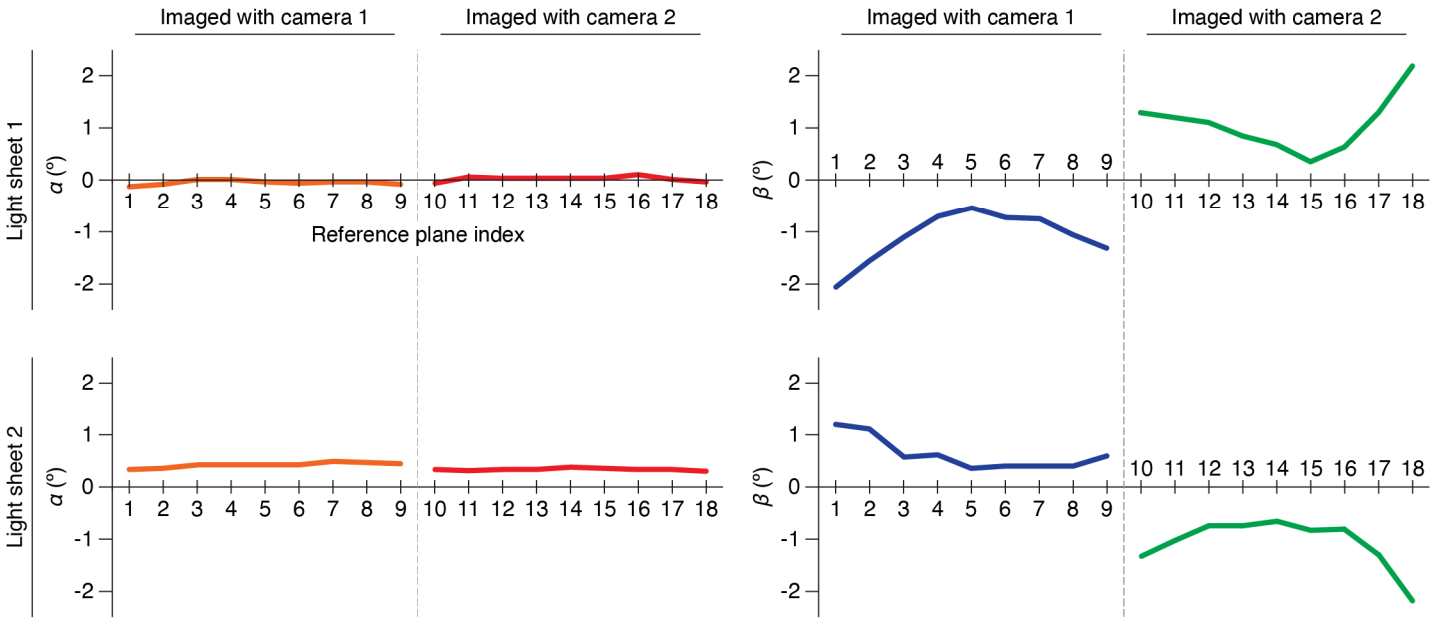

Nature Biotechnology: doi:10.1038/nbt.3708

Supplementary Figure 18 | Modeling spatial variance of light-sheet angle beta in a *Drosophila* embryo

A simple ray optics model qualitatively and quantitatively recapitulates the main features of the experimentally measured β-deflection curves shown in **Supplementary Fig. 17**. The illustrations and modeling results shown here accompany the section "Ray optics model for interpreting experimentally observed β-deflections" in **Supplementary Methods 5** describing the ray optics model and related optical effects relevant for light-sheet microscopy in detail.

Briefly, the model (applied here to a *Drosophila* embryo) considers the refraction of the light sheets at the interface between medium/matrix and embryo (**a**) as well as the curvature of the detection focal plane caused by differences in refractive indices of embryo and surrounding medium/matrix (resulting in the embryo acting as a lens in the detection path) (**b**). The effects of light-sheet refraction (**c**) and focal plane curvature (**d**) are quantitatively modeled assuming average refractive indices of n_e = 1.35 for the embryo[28] and n_m = 1.339 for the mounting matrix[27]. When considering both effects and the resulting spatially-varying β-deflection of light sheets relative to detection focal planes (**e**), we obtain a theoretical β-deflection curve that is in good qualitative and quantitative agreement with our experimental measurements (**f**) reported in **Supplementary Fig. 17**.

Nature Biotechnology: doi:10.1038/nbt.3708

Supplementary Figure 18 | Modeling spatial variance of light-sheet angle beta in *Drosophila*

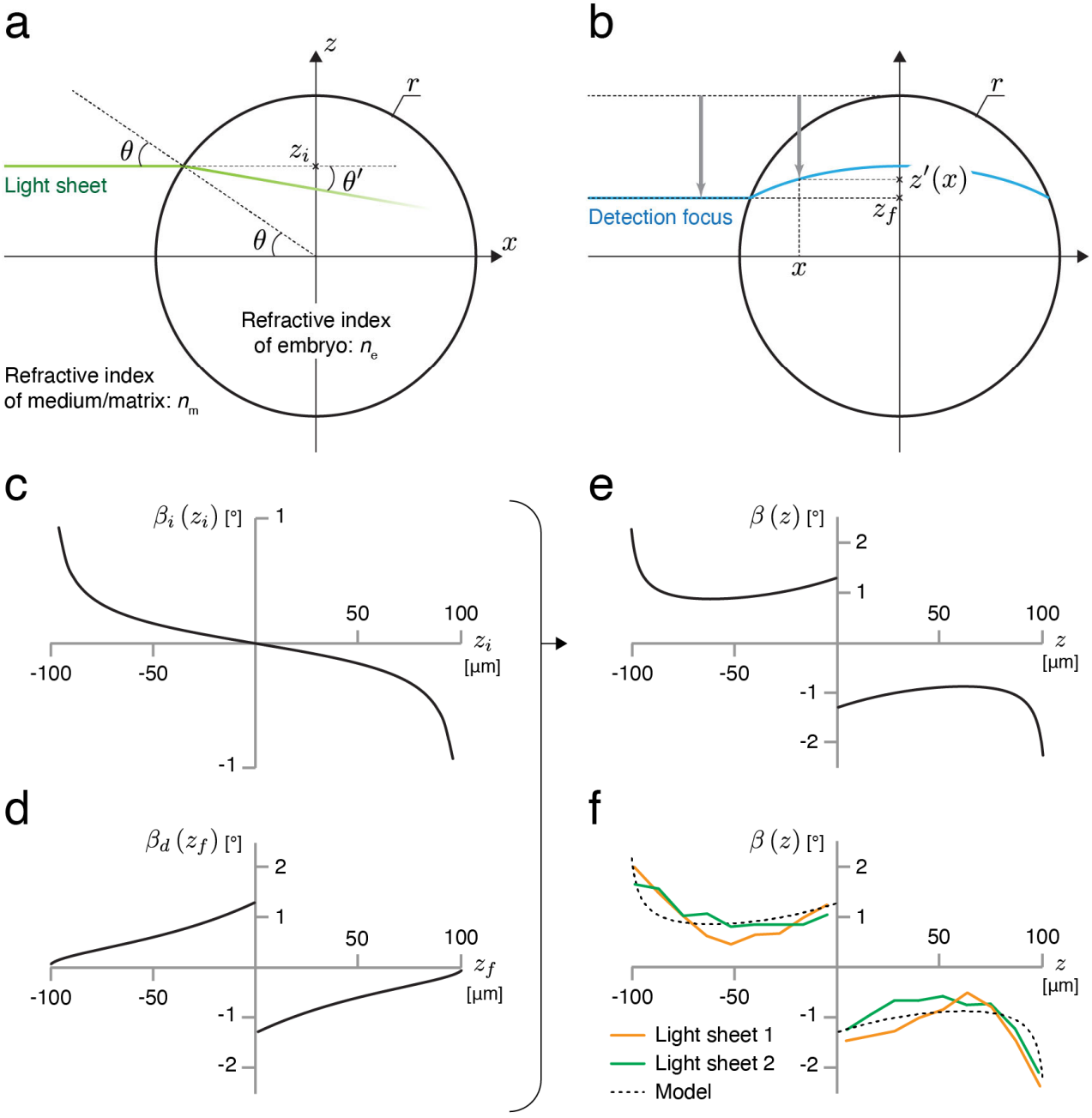

Nature Biotechnology: doi:10.1038/nbt.3708

Supplementary Figure 19 | Physiology controls for adaptive imaging of zebrafish embryogenesis

Physiology controls for spatiotemporally adaptive long-term imaging of zebrafish embryonic development, showing the specimen used for the imaging experiment (a) side-by-side with a control specimen that was not exposed to laser light (b). Both zebrafish larvae were imaged two days after the live imaging experiment performed with the primary specimen, using an Olympus MVX10 microscope for monitoring specimen physiology and normal development.

Nature Biotechnology: doi:10.1038/nbt.3708

Supplementary Figure 19 | Physiology controls for adaptive imaging of zebrafish embryogenesis

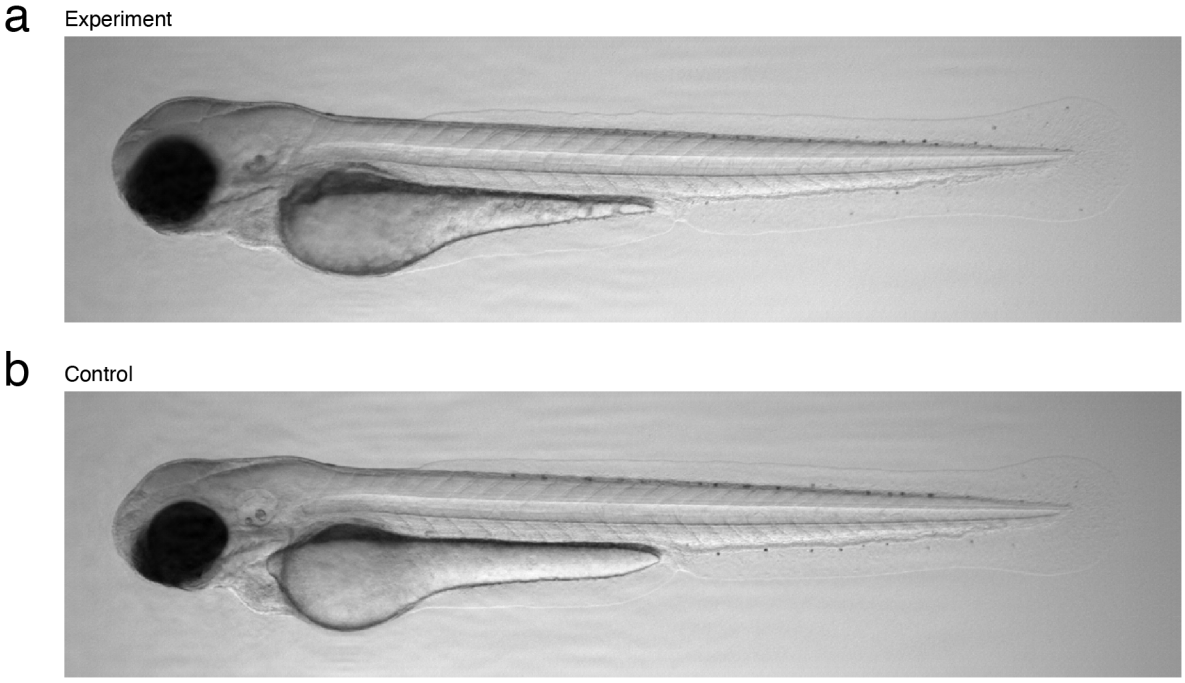

Nature Biotechnology: doi:10.1038/nbt.3708

Supplementary Tables

Supplementary Table 1 | Synthetic performance benchmarks for evaluating focus metrics

Benchmark evaluation of 30 image quality metrics on 24 synthetic focus stacks, which were derived from 4 test images using noise levels of 0%, 10%, 20%, 30%, 40% and 50% of the average pixel intensity. The error is defined as the distance between the plane index i_o in the stack corresponding to optimal focus quality ($i_o = 50$) and the plane index i_m at which the image quality metric attains its maximum. The distance is measured in standard deviations of the blur kernel in pixels. Half of the image quality metrics achieve an error below half a pixel. The low-pass filtering radius was set to $r_p = 1.5$ pixels. *R*-score and DLE are defined in **Supplementary Methods 2**.

Class	Image quality metric	Median error	Mean error	Max error	Median *R*-score	Median DLE	Median processing time (ns / p)
Spectral	Normalized DCT Shannon entropy	0	0.16	1	21.83	38%	10
Spectral	Normalized DCT generalized Bayesian entropy ($e = 4$)	0	0.16	1	16.4	39%	12
Spectral	Normalized DCT generalized Bayesian entropy ($e = 6$)	0	0.16	1	16.4	39%	13
Spectral	Normalized DCT Bayesian entropy	0	0.16	1	15.2	39%	9
Spectral	Lp sparsity of DCT	0	0.16	2	28.66	53%	10
Differential	Brenner measure	0	0.20	3	29.66	47%	4
Differential	Total variation	0	0.20	3	29.16	53%	4
Spectral	High/low freq. DFT power ratio	0	0.20	2	30.25	53%	19
Differential	Block total variation	0	0.20	3	28.83	53%	5
Spectral	Logarithmic moment spectral power	0	0.33	5	29	43%	22
Spectral	Normalized DFT Shannon entropy	0	0.37	5	25.5	43%	21
Differential	Tenengrad	0	0.41	5	27.83	50%	4
Correlative	Symmetric Vollath F4	0	0.45	3	30.5	54%	4
Differential	Squared Laplacian	0	0.5	11	30	50%	4
Spectral	Normalized DCT Shannon entropy (downscaled)	0	0.66	5	30	52%	7
Statistic	Lp sparsity	0	0.75	4	27.16	55%	17
Differential	Absolute Laplacian	0	1	16	32	55%	4
Spectral	Normalized DCT Shannon entropy (median filtered)	0	1.04	17	24	45%	26
Correlative	Vollath F4	0	1.04	9	26.83	60%	4

Nature Biotechnology: doi:10.1038/nbt.3708

Supplementary Table 1 (Continued)

Class	Image quality metric	Median error	Mean error	Max error	Median *R*-score	Median DLE	Median processing time (ns / p)
Spectral	High/low freq. DCT power ratio	0	1.62	33	24.83	56%	11
Statistic	Shannon Entropy of histogram	0	1.70	32	28.5	61%	4
Statistic	Variance	0	1.83	32	26.83	56%	4
Statistic	Normalized variance	0	1.83	32	26.83	56%	4
Correlative	Vollath F5	0	1.91	23	16.46	59%	4
Spectral	Kristan's 8x8 DCT Bayes spectral entropy	0	6	44	36.75	61%	4
Statistic	Mean	1	13.5	49	24.5	64%	4
Statistic	Kurtosis	3	14	49	25.5	63%	4
Statistic	Kurtosis of differences	3.5	9.45	49	31.5	61%	4
Statistic	Maximum	9.5	16.75	48	38.5	63%	4
Spectral	Normalized Haar wavelet transform Shannon entropy	37.5	31.70	49	25.9	64%	69

Nature Biotechnology: doi:10.1038/nbt.3708

Supplementary Table 2 | Dependency of synthetic focus metric performance on low-pass filtering

Performance dependence of the best spectral image quality metric (Normalized DCT Shannon entropy) on low-pass filter settings, evaluated using the synthetic benchmark data. The optimal radius of the low-pass filter is $r_p = 1.5$ pixels.

Low-pass filter diameter	Median error	Mean error	Max error	Median *R*-score	Median DLE
1	0.00	1.67	19.00	45.75	61%
2	0.00	0.58	10.00	46.00	51%
3	0.00	0.46	10.00	46.50	47%
4	0.00	0.29	5.00	23.96	48%
5	0.00	0.33	5.00	23.00	44%
6	0.00	0.17	1.00	21.83	38%
7	0.00	0.29	2.00	16.10	46%
8	0.00	0.33	2.00	15.80	46%
9	0.00	0.42	2.00	15.60	49%
10	0.00	0.50	2.00	14.67	53%
11	0.50	0.67	3.00	12.29	55%
12	0.00	0.71	3.00	13.15	58%
13	0.00	0.88	4.00	14.08	58%
14	1.00	1.17	8.00	14.42	60%
15	1.00	0.96	4.00	13.07	59%
16	1.00	0.96	4.00	14.83	61%

Nature Biotechnology: doi:10.1038/nbt.3708

Supplementary Table 3 | Real-data performance benchmarks for evaluating focus metrics

Benchmark evaluation of 30 image quality metrics on 66 light-sheet focus stacks. The table is sorted by descending median, then descending mean, and then ascending median *R*-score. The low-pass filtering radius is set to $r_p = 1.5$ pixels. See **Supplementary Table 1** and **Supplementary Methods 2** for parameter definitions.

Class	Image quality metric	Median error	Mean error	Max error	Median *R*-score	Median DLE	Median processing time (ns / p)
Spectral	Normalized DCT Shannon entropy	0.00	0.32	5.00	7.35	19%	27
Spectral	Normalized DCT generalized Bayesian entropy ($e = 6$)	0.00	0.33	5.00	6.24	16%	39
Spectral	Normalized DCT generalized Bayesian entropy ($e = 4$)	0.00	0.33	5.00	6.19	17%	38
Spectral	Normalized DCT Bayesian entropy	0.00	0.33	5.00	5.11	16%	24
Spectral	Normalized DCT Shannon entropy (median filtered)	0.06	0.59	6.15	7.36	24%	45
Spectral	Normalized DFT Shannon entropy	0.16	0.53	5.00	7.50	26%	33
Differential	Tenengrad	0.25	0.61	4.80	7.00	16%	5
Correlative	Vollath F4	0.31	1.01	10.00	7.88	37%	4
Spectral	Logarithmic moment spectral power	0.31	1.27	7.75	8.00	17%	35
Spectral	Lp sparsity of DCT	0.38	0.77	10.54	6.17	29%	27
Correlative	Symmetric Vollath F4	0.43	1.02	7.90	7.50	32%	5
Differential	Brenner measure	0.49	0.94	9.66	7.38	28%	5
Spectral	Normalized DCT Shannon entropy (downscaled)	0.50	0.82	9.66	6.69	20%	15
Differential	Squared Laplacian	0.50	0.98	14.93	7.17	38%	5
Differential	Total variation	0.50	1.17	9.66	6.68	28%	5
Differential	Block total variation	0.50	1.26	9.66	6.64	24%	8
Differential	Absolute Laplacian	0.81	1.53	18.50	9.30	48%	5
Statistic	Lp sparsity	0.99	2.13	12.00	7.06	35%	57
Spectral	High/low freq. DFT power ratio	1.10	9.30	42.45	10.25	53%	27
Spectral	High/low freq. DCT power ratio	1.33	9.23	42.45	9.25	55%	26
Correlative	Vollath F5	1.63	2.43	12.00	6.89	36%	5
Statistic	Variance	1.69	2.78	16.50	7.17	40%	4

Nature Biotechnology: doi:10.1038/nbt.3708

Supplementary Table 3 (Continued)

Class	Image quality metric	Median error	Mean error	Max error	Median *R*-score	Median DLE	Median processing time (ns / p)
Statistic	Normalized variance	1.69	2.78	16.50	7.17	40%	4
Spectral	Kristan's 8x8 DCT Bayes spectral entropy	1.88	7.22	42.45	12.00	54%	5
Statistic	Maximum	2.00	3.64	21.07	8.00	47%	4
Statistic	Kurtosis of differences	3.88	7.45	50.59	10.00	51%	5
Statistic	Mean	7.50	9.74	50.59	11.39	54%	4
Spectral	Normalized Haar wavelet transform Shannon entropy	8.63	12.08	42.45	9.90	54%	116
Statistic	Kurtosis	9.33	11.57	52.22	9.33	47%	5
Statistic	Shannon entropy of histogram	10.00	12.21	42.45	8.39	49%	5

Nature Biotechnology: doi:10.1038/nbt.3708

Supplementary Table 4 | Dependency of real-data focus metric performance on low-pass filtering

Performance dependence of the best spectral image quality metric (Normalized DCT Shannon entropy) on low-pass filter settings, evaluated using the light-sheet benchmark data. The optimal low-pass filtering radius is $r_p = 1.5$ pixels.

Low-pass filter diameter	Median error	Mean error	Max error	Median *R*-score	Median DLE
1	0.50	0.94	5.00	9.00	36%
2	0.06	0.42	5.00	8.00	24%
3	0.00	0.32	5.00	7.35	19%
4	0.00	0.52	9.66	6.40	16%
5	0.00	0.53	9.66	6.00	15%
6	0.25	0.58	7.02	5.92	14%
7	0.25	0.62	7.90	5.57	14%
8	0.25	0.55	4.39	5.46	16%
9	0.37	0.69	7.90	5.00	15%
10	0.50	0.84	7.90	5.00	17%
11	0.88	1.10	7.90	4.58	17%
12	0.88	1.12	7.90	4.59	17%
13	0.88	1.35	7.90	4.36	18%
14	1.00	1.51	7.90	4.58	19%
15	1.38	1.79	6.25	4.52	22%
16	1.17	1.87	6.25	4.37	24%

Nature Biotechnology: doi:10.1038/nbt.3708

Supplementary Table 5 | Protocol for adaptive imaging in the system perturbation benchmark

Overview of experiment settings and parameter configuration used for spatiotemporally adaptive imaging in the system perturbation benchmark visualized in **Supplementary Video 1** and **Supplementary Fig. 10**.

Parameter	Setting
Specimen	*Drosophila* embryo
Genotype	w; His2Av-mRFP1; +
Embedding	1.0% SeaPlaque agarose in water
Illumination	561 nm, Olympus 4x/0.28 objectives
Detection	561 nm long-pass filters, Nikon 16x/0.8 objectives
Temporal resolution	30 seconds
Time-lapse duration	4 hours
Lateral pixel size	0.406 µm
Z-step size	2.031 µm
Number of reference planes	4
Spacing of reference planes	40 µm, 40 µm, 40 µm
Correction mode	Special optimization theory
Image quality metric	DCTS
Min. focus value	-∞
Max. D_2 correction	∞
Max. I_1, I_2 correction	∞
Search radius	4 µm
Number of samples	7

Nature Biotechnology: doi:10.1038/nbt.3708

Supplementary Table 6 | Protocol for adaptive imaging of *Drosophila* embryonic development

Overview of experiment settings and parameter configuration used for spatiotemporally adaptive imaging of *D. melanogaster* embryonic development (**Supplementary Videos 2-4**, **Fig. 2** and **Supplementary Figs. 13** and **14**).

Parameter	Setting
Specimen	*Drosophila* embryo
Genotype	w; His2Av-mRFP1; +
Embedding	1.0% SeaPlaque agarose in water
Illumination	561 nm, Nikon 10x/0.3 objectives
Detection	561 nm long-pass filters, Nikon 16x/0.8 objectives
Temporal resolution	30 seconds
Time-lapse duration	21 hours
Lateral pixel size	0.406 μm
Z-step size	2.031 μm
Number of reference planes	6
Spacing of reference planes	30 μm, 30 μm, 40 μm, 30 μm, 30 μm
Correction mode	Special optimization theory
Image quality metric	DCTS
Min. focus value	3×10^{-4}
Max. D_2 correction	0.5 μm
Max. I_1, I_2 correction	1.5 μm
Search radius	4 μm
Number of samples	7

Nature Biotechnology: doi:10.1038/nbt.3708

Supplementary Table 7 | Protocol for adaptive imaging of zebrafish embryonic development

Overview of experiment settings and parameter configuration used for spatiotemporally adaptive imaging of zebrafish embryonic development (**Supplementary Video 5** and **Fig. 3a-d**).

Parameter	Setting
Specimen	Zebrafish embryo
Genotype	*Tg(β-actin:H2B-eGFP)*
Embedding	0.3% agarose in 0.3x Danieau's solution Teflon tube supported by 3 mm glass capillary
Illumination	488 nm, Olympus 5x/0.1 objectives
Detection	525/50 nm band-pass filters, Nikon 16x/0.8 objectives
Temporal resolution	100 seconds
Time-lapse duration	12 hours
Lateral pixel size	0.406 µm
Z-step size	3.250 µm
Number of reference planes	7
Spacing of reference planes	80 µm, 90 µm, 140 µm, 140 µm, 110 µm, 80 µm
Correction mode	Special optimization theory
Image quality metric	DCTS
Min. focus value	2.146×10^{-5}
Max. D_2 correction	0.4 µm
Max. I_1, I_2 correction	0.7 µm
Search radius	6 µm
Number of samples	9

Nature Biotechnology: doi:10.1038/nbt.3708

Supplementary Table 8 | Protocol for interleaved imaging of zebrafish embryonic development

Overview of experiment settings and parameter configuration used for spatiotemporally adaptive imaging of zebrafish embryonic development with interleaved acquisition of adaptively corrected and uncorrected image stacks (**Supplementary Videos 6** and **7**, **Fig. 3e** and **Supplementary Fig. 15**).

Parameter	Setting
Specimen	Zebrafish embryo
Genotype	*Tg(β-actin:H2B-eGFP)*
Embedding	0.3% agarose in 0.3x Danieau's solution Teflon tube supported by 3 mm glass capillary
Illumination	488 nm, Olympus 5x/0.1 objectives
Detection	525/50 nm band-pass filters, Nikon 16x/0.8 objectives
Temporal resolution	180 seconds
Time-lapse duration	6.1 hours
Lateral pixel size	0.406 µm
Z-step size	3.250 µm
Number of reference planes	7
Spacing of reference planes	80 µm, 100 µm, 120 µm, 120 µm, 100 µm, 80 µm
Correction mode	General optimization theory
Image quality metric	DCTS
Min. focus value	2.146×10^{-5}
Max. D_2 correction	0.5 µm
Max. I_1, I_2 correction	1.5 µm
Search radius	4 µm
Number of samples	9

Nature Biotechnology: doi:10.1038/nbt.3708

Supplementary Table 9 | Protocol for adaptive two-color imaging of nervous system development

Overview of experiment settings and parameter configuration used for spatiotemporally adaptive two-color imaging of nervous system development (**Supplementary Video 8** and **Fig. 4**).

Parameter	Setting
Specimen	*Drosophila* embryo
Genotype	w; His2Av-mRFP1; deadpanEE-Gal4 × w/y; His2Av-mRFP1; 10XUAS-IVS-myr::GFP
Embedding	1.0% SeaPlaque agarose, 2 mm glass capillary
Illumination	488 nm, 561 nm; Nikon 10x/0.3 objectives
Detection	525/50 nm band-pass and 561 nm long-pass filters Nikon 16x/0.8 objectives
Temporal resolution	60 seconds
Time-lapse duration	20 hours
Lateral pixel size	0.406 µm
Z-step size	2.031 µm
Number of reference planes	7
Spacing of reference planes	10 µm, 20 µm, 30 µm, 40 µm, 30 µm, 20 µm, 10 µm
Correction mode	General optimization theory
Image quality metric	DCTS
Min. argmax probability	0.60
Max. D_2 correction	0.5 µm
Max. I_1, I_2 correction	1.5 µm
Search radius	4 µm
Number of samples	7

Nature Biotechnology: doi:10.1038/nbt.3708

Supplementary Table 10 | Protocol for adaptive whole-brain functional imaging

Overview of experiment settings and parameter configuration used for adaptive zebrafish whole-brain functional imaging (**Supplementary Video 9** and **Fig. 6**).

Parameter	Setting
Specimen	Zebrafish larva
Genotype	*Tg(elavl3:GCaMP6f)*
Embedding	1.0% Sigma Type VII agarose, 2 mm glass capillary
Illumination	488 nm, Nikon 10x/0.3 objectives
Detection	525/50 nm band-pass filters, Nikon 16x/0.8 objectives
Temporal resolution	0.75 seconds (includes acquisition of corrected and uncorrected image data, i.e. one whole-brain volume was acquired every 0.375 s)
Time-lapse duration	20 hours
Lateral pixel size	0.406 µm
Z-step size	7 µm
Number of reference planes	7
Spacing of reference planes	20 µm, 30 µm, 30 µm, 30 µm, 30 µm, 20 µm
Correction mode	General optimization theory
Image quality metric	DCTS
Min. focus value	8×10^{-5}
Min. argmax probability	0.80
Max. I_1, I_2 correction	2 µm
Search radius	6 µm
Number of samples	11

Nature Biotechnology: doi:10.1038/nbt.3708

Supplementary Table 11 | Light-sheet microscope for spatiotemporally adaptive imaging

Overview of optical and mechanical parts, electronics, computational hardware and software modules used to build the custom light-sheet microscope for spatiotemporally adaptive imaging.

Module	Component	Product(s)	Manufacturer
Optical table and breadboard	Optical table	ST-UT2-48-8 optical table (4' × 8' × 8") S-2000 series 28" isolators with automatic leveling S-2000A-428 (4×) IQ-200-UG-8 damper upgrade	Newport
	Breadboard	Custom RG breadboard 04SI69108 (2.0' × 5.0' × 2.4")	Newport
	Rail system	SYS 40 and SYS 65 rail and slide system components	OWIS
Lasers (shared modules)	SOLE-3 engine with dual-fiber head	Solid-state lasers: 488 nm, 561 nm, 594 nm	Omicron Laserage
Illumination sub-systems (two modules)	High-speed laser shutter	VS14S2ZM1-100 with AlMgF2 coating VMM-D3 three-channel driver	Uniblitz
	Illumination filter wheel	96A351 filter wheel MAC6000 DC servo controller	Ludl
		NDQ neutral density filters	Melles Griot
		Laser cleanup notch filters: 488/10, 561/10, 594/10	Chroma
	Relay lens pair	49-361-INK (2×)	Edmund Optics
	Dual-axis laser scanner (2×)	6215HSM40B galvanometer scanner MicroMax 673XX dual-axis integrating servo driver amplifier 6 mm XY mirror set, mount and interconnect cables	Cambridge Technology
		MK320S-24 power supply	Astrodyne

Nature Biotechnology: doi:10.1038/nbt.3708

Supplementary Table 11 (Continued)

Module	Component	Product(s)	Manufacturer
Illumination sub-systems (two modules)	F-theta lens	66-S80-30T-488-1100nm	Custom design (built by Special Optics)
	Tube lens	49-360-INK	Edmund Optics
	Piezo objective positioner	P-622.1CD PIHera piezo linear stage E-665 piezo amplifier and servo controller	Physik Instrumente
	Illumination objective	Plan Fluor 10×/0.30W	Nikon
Detection sub-systems (two modules)	Detection filter wheel	96A354 filter wheel MAC6000 DC servo controller	Ludl
		RazorEdge and EdgeBasic long-pass filters: 488 nm, 561 nm, 594 nm BrightLine band-pass filters: 525/50 nm	Semrock
	Tube lens module	CFI second lens unit	Nikon
		AxioImager 130 mm ISD tube lens	Carl Zeiss
	Piezo objective positioner	P-628.1CD PIHera piezo linear stage E-665 piezo amplifier and servo controller	Physik Instrumente
	Detection objective	CFI60/75 LWD water-dipping series	Nikon
		Apochromat/Plan-Apochromat water-dipping series	Carl Zeiss
	Camera	Orca Flash 4.0 v2 camera JULABO water chiller	Hamamatsu

Nature Biotechnology: doi:10.1038/nbt.3708

Supplementary Table 11 (Continued)

Module	Component	Product(s)	Manufacturer
Specimen chamber	Four-view specimen chamber	Chamber manufactured from black Delrin	Custom design
	Specimen holder	Plastic sample holder cup Cup holder manufactured from medical-grade stainless steel Adapter for multi-stage positioning system	Custom design
Specimen positioning system	Translation stages (3×)	M-111K046	Physik Instrumente
	Rotary stage	M-116.2DG	Physik Instrumente
	Motion I/O interface and amplifier	C-809.40 4-channel servo-amplifier	Physik Instrumente
	Motion controller	PXI-7354 4-axis stepper/servo motion controller	National Instruments
Real-time electronics	Real-time controller with LabVIEW Real-Time OS	PXI-8110 Core 2 Quad 2.2 GHz	National Instruments
	I/O interface boards (4×)	PXI-6733 high-speed analog output 8-channel board	National Instruments
	BNC connector boxes (4×)	BNC-2110 shielded connector block	National Instruments
	Serial interface board	PXI-8432/2	National Instruments
Control software	Real-time modules	32-bit LabVIEW code	Custom software
	Host modules	64-bit LabVIEW code	Custom software
	AutoPilot modules	Java 8 code C interface library code Third-party libraries*	Custom software and third-party libraries

Nature Biotechnology: doi:10.1038/nbt.3708

Supplementary Table 11 (Continued)

Module	Component	Product(s)	Manufacturer
Microscope control workstation	SX6750 microscope control and data acquisition workstation	Intel Xeon E5-2687W CPUs (2×) 16 GB DDR-3 RAM modules (16×) 16-channel Intel RS2WG160 RAID controller Intel 520 Series 480GB SSDs (2×) Western Digital 2.5 XE 900GB HDDs (14×) Firebird CameraLink frame grabbers (2×) Intel AXXRSBBU8 battery backup Intel X520-SR1 SFP+ SR LC fiber network adapter PNY nVidia Quadro 2000D graphics card	Colfax International

* Third-party libraries used in the AutoPilot framework include the following code modules:

com.googlecode.efficient-java-matrix-library:ejml:0.24
org.apache.commons:commons-collections4:4.+
org.apache.commons:commons-lang3:3.1
org.apache.commons:commons-math3:3.2
commons-beanutils:commons-beanutils:1.7.0'
commons-digester:commons-digester:1.8'
commons-logging:commons-logging:1.1.1'
net.sourceforge.csparsej:csparsej:1.1.1
org.codehaus.groovy:groovy-all:2.2.2
com.github.rwl:jtransforms:2.4.0
commons-io:commons-io:2.+
net.sf.trove4j:trove4j:3.0.3
org.jzy3d:jzy3d-api:0.9.1
javassist:javassist:3.0
jdepend:jdepend:2.9.1
java3d:vecmath:1.3.1
args4j:args4j:2.0.29

Nature Biotechnology: doi:10.1038/nbt.3708

Supplementary Videos

Supplementary Video 1 | Perturbation benchmark of spatiotemporally adaptive imaging performance

Spatiotemporally adaptive imaging of *Drosophila* embryonic development (using a His2Av-mRFP1 embryo with fluorescently labeled cell nuclei), demonstrating the framework's ability to compensate not only for specimen-induced dynamic changes but also for manual perturbations of the microscope state (such as rapid misalignment of the positions of tip/tilt mirrors used for light-sheet illumination or of piezo actuators used for positioning the detection objectives). Following each manual perturbation of the system (see annotations in the time line shown to the top right), the adaptive imaging framework rapidly detects the perturbation through real-time analysis of the image data, determines the appropriate countermeasures (resulting in adjustments of the digitally accessible degrees of freedom of the microscope; see red, green and magenta plots to the right) and restores optimal image quality during time-lapse imaging of the developing *Drosophila* embryo.

Left: dorsal and ventral maximum-intensity projections of the three-dimensional image data, shown together with a small anterior-view projection inset indicating the locations of the four reference planes used for adaptive imaging (labeled 0, 1, 2 and 3). Right: time course of the experiment and manual perturbations of the microscope (top), whole-volume DCTS image quality metric (second from top) and corrections for D_2, I_1 and I_2 for all four reference planes (third to fifth panel). Image quality is temporarily degraded by the instantaneous (red arrows) or continuous (red gradients) system perturbations but quickly recovers as corrections are being applied by the AutoPilot framework.

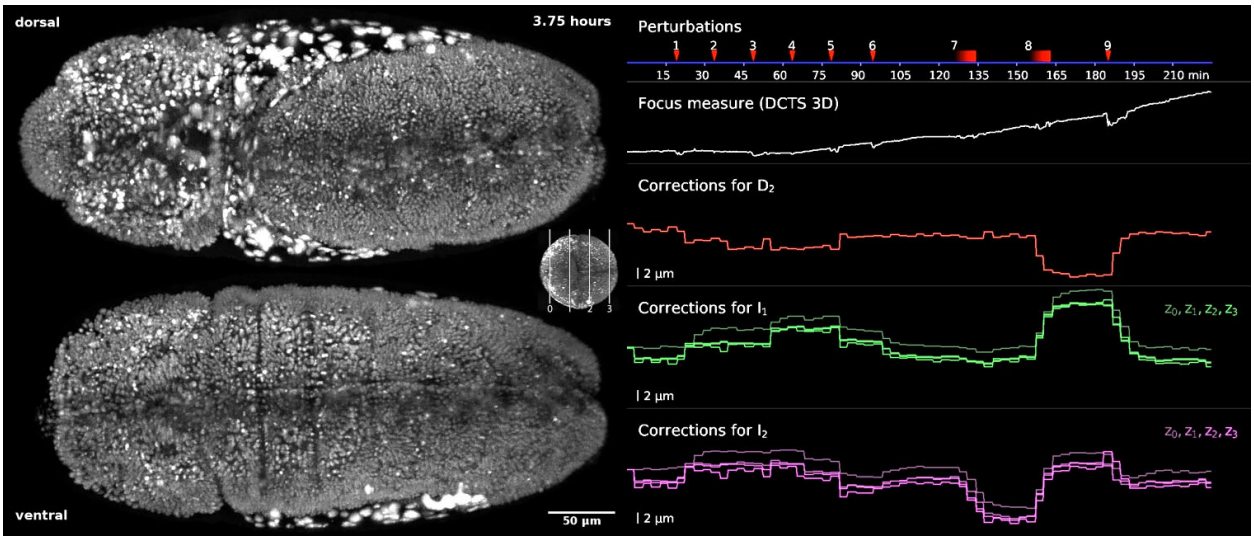

Nature Biotechnology: doi:10.1038/nbt.3708

Supplementary Video 2 | Spatiotemporally adaptive imaging of *Drosophila* embryogenesis

Spatiotemporally adaptive imaging of *Drosophila* embryonic development (using a His2Av-mRFP1 embryo with fluorescently labeled cell nuclei).

Left: dorsal and ventral maximum-intensity projections of the three-dimensional image data, shown together with a small anterior-view projection inset indicating the locations of the six reference planes used for adaptive imaging (labeled 0, 1, 2, 3, 4 and 5). Right: time course of the imaging experiment (top), whole-volume DCTS image quality metric as function of time (second from top) and corrections for D_2, I_1 and I_2 as a function of time for all six reference planes (third to fifth panels).

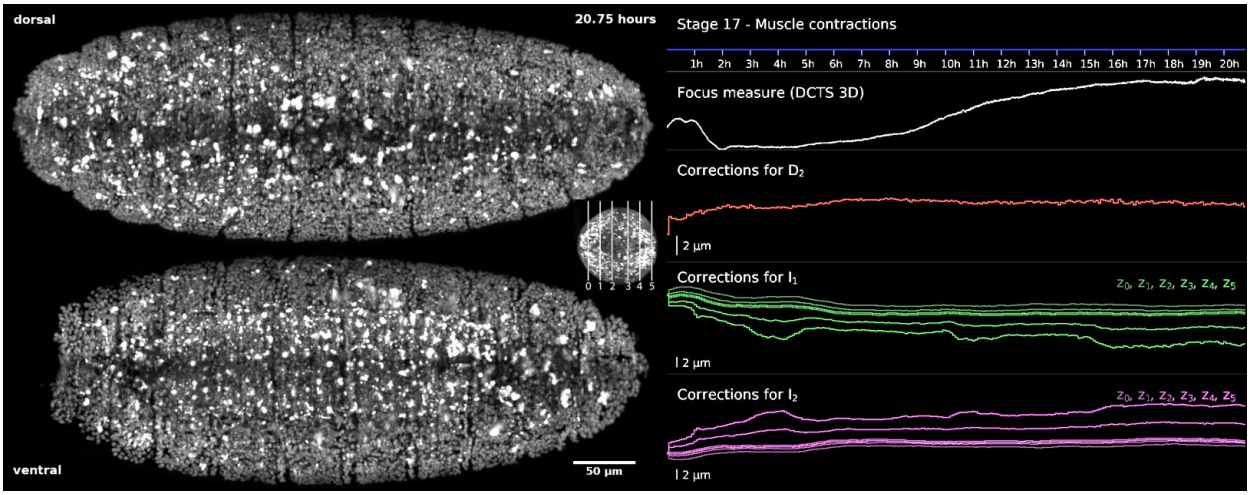

Nature Biotechnology: doi:10.1038/nbt.3708

Supplementary Video 3 | Recovery of high spatial resolution in *Drosophila* adaptive imaging

Quality comparison of corrected and uncorrected time-lapse image data for the spatiotemporally adaptive imaging experiment shown in **Supplementary Video 2**, demonstrating the degradation of image contrast and spatial resolution in the absence of system corrections. The left panel shows a maximum-intensity projection of the embryo and indicates the locations of the four regions shown to the right, which cover a wide range of lateral locations and depths in the sample. For each region, image quality with and without adaptive imaging are shown (center columns). Image quality in the absence of corrections can be reconstructed from focus stacks and parameter protocols, which are routinely logged during adaptive imaging (**Supplementary Methods 6)**. These diagnostics allow us to ascertain that image quality at a given location and time point was indeed optimal (within the microscope's abilities), given sample properties and imaging conditions. Loss of image quality without adaptive imaging is quantified as the difference in DCTS (image quality metric) values for the image data obtained for corrected and uncorrected system states (right). Importantly, corrected and uncorrected systems states are initially identical, i.e. a full system optimization was performed at the beginning of the experiment and was used to acquire all images labeled "Not corrected".

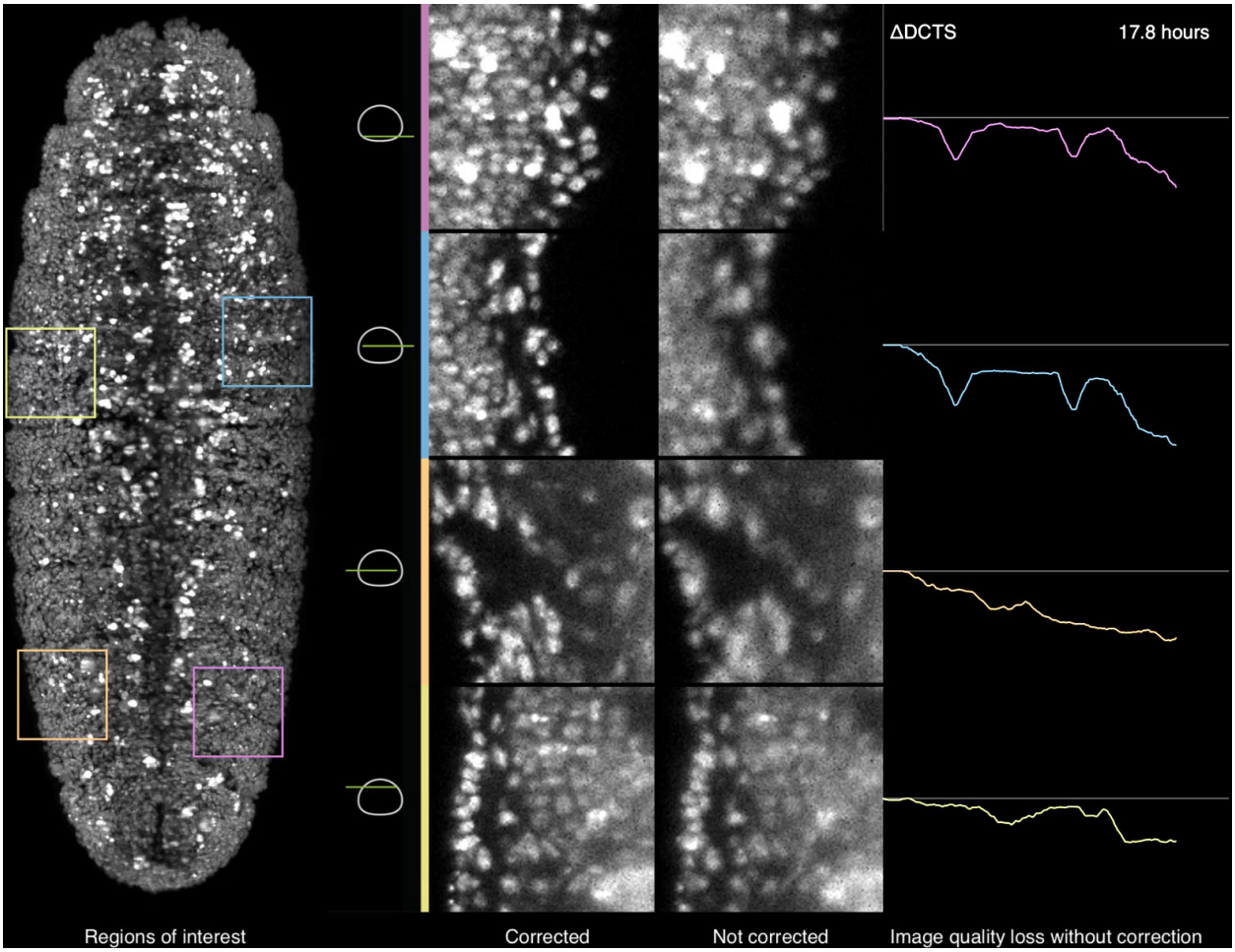

Nature Biotechnology: doi:10.1038/nbt.3708

Supplementary Video 4 | Recovery of cellular resolution in deep tissue layers by adaptive imaging

Quality comparison of corrected and uncorrected time-lapse image data in deep tissue regions of a developing *Drosophila* embryo for the spatiotemporally adaptive imaging experiment shown in **Supplementary Video 2**. The side-by-side comparison demonstrates the degradation of image contrast and spatial resolution in the absence of system corrections in three different regions of the developing nervous system. The left panel shows a lateral view of the *Drosophila* embryonic nervous system (deadpanEE-Gal4, UAS-myr::GFP) and indicates the anatomical locations of the three regions shown to the right (brain lobe, suboesophageal ganglion [SOG] and ventral nerve cord). For each region, image quality with and without adaptive imaging are shown using a ubiquitous nuclear fluorescent label (His2Av-mRFP1, center columns). As is evident from these data, adaptive imaging recovers cellular resolution in many deep-tissue regions that cannot be resolved with non-adaptive microscopy. Uncorrected images were reconstructed as described in section "*Reconstruction of uncorrected image data from AutoPilot logs*" of **Supplementary Methods 6** and are shown here next to corrected images in 6 min intervals. The full temporal resolution of the underlying time-lapse imaging experiment is 1 min. Loss of image quality without adaptive imaging is quantified as the difference in DCTS (image quality metric, grey line corresponds to ΔDCTS = 0) values for the image data obtained for corrected and uncorrected system states (right). Importantly, corrected and uncorrected systems states are initially identical, i.e. a full system optimization was performed at the beginning of the experiment and was used to acquire all images labeled "Not corrected".

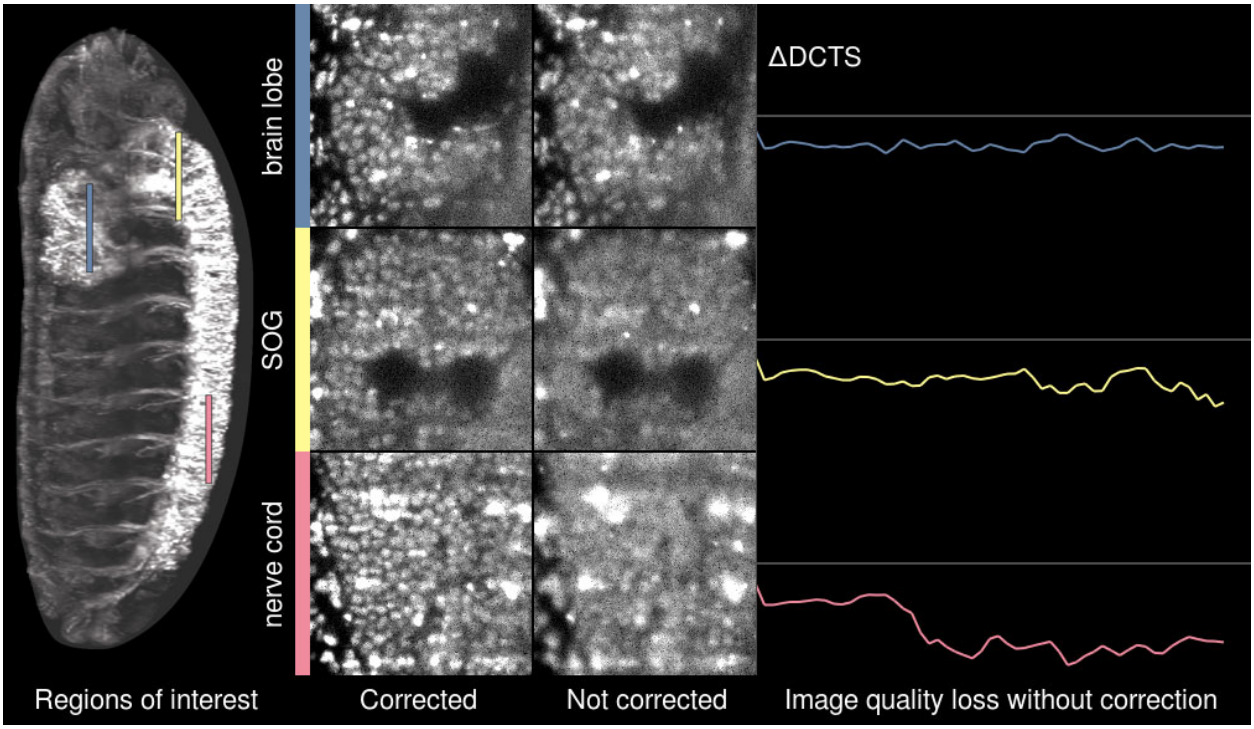

Nature Biotechnology: doi:10.1038/nbt.3708

Supplementary Video 5 | Spatiotemporally adaptive imaging of zebrafish embryogenesis

Spatiotemporally adaptive imaging of zebrafish embryonic development (using a β-actin:H2B-eGFP embryo with fluorescently labeled cell nuclei).

Top: animal, vegetal and lateral views (maximum-intensity projections) of the three-dimensional image data. Bottom: time course of the imaging experiment (first panel below image data), whole-volume DCTS image quality metric as a function of time (second panel below image data) and corrections for D_2, I_1 and I_2 as a function of time for all seven reference planes used in this experiment (third to fifth panels below image data). Note that the adaptive imaging framework automatically detects emerging fluorescence signal in previously unpopulated regions of the imaging volume (ventral hemisphere) and thus adapts on-demand to the large-scale cell movements observed in the course of zebrafish epiboly.

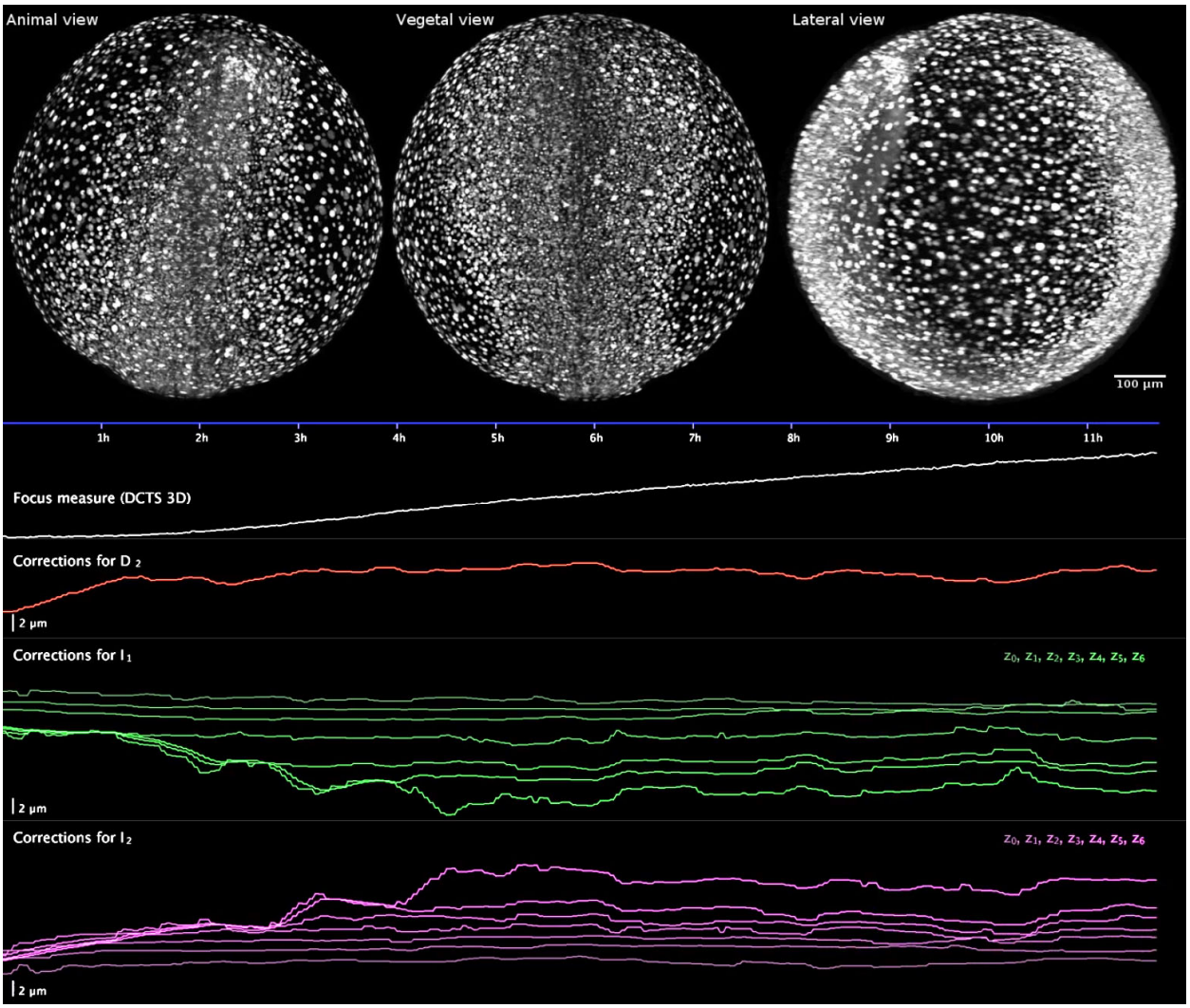

Nature Biotechnology: doi:10.1038/nbt.3708

Supplementary Video 6 | Recovery of high spatial resolution in zebrafish adaptive imaging

Quality comparison (part 1, see next video for part 2) of corrected and uncorrected time-lapse image data for spatiotemporally adaptive imaging of a developing zebrafish embryo, demonstrating adaptation to rapid, large-scale cell movements during epiboly. The left panel shows animal- and lateral-view maximum-intensity projections of the image data, highlighting four regions at different lateral positions and depths. The center columns show image quality in these four regions with and without system corrections. In contrast to **Supplementary Videos 3** and **4**, two versions (corrected, uncorrected) of the image data were acquired by interleaving the time-lapse experiment. Version 1 of the data (time points with even indices) was recorded using adaptive imaging with all degrees of freedom of the microscope, whereas version 2 (time points with odd indices) was recorded with non-adaptive SiMView microscopy. Importantly, both versions of the experiment start with the same initial (optimized) microscope state, i.e. all microscope parameters are identical at time point 0. Regions that are populated by cells at the end of the time-lapse but not in the beginning (ventral hemisphere), suffer the most from a lack of online system corrections (regions marked orange or yellow). Loss of image quality without adaptive imaging is quantified as the difference in DCTS values for the image data obtained for corrected and uncorrected system states. The corresponding plots (right) show that image quality in the absence of system corrections is consistently worse. Red lines indicate lack of local signal.

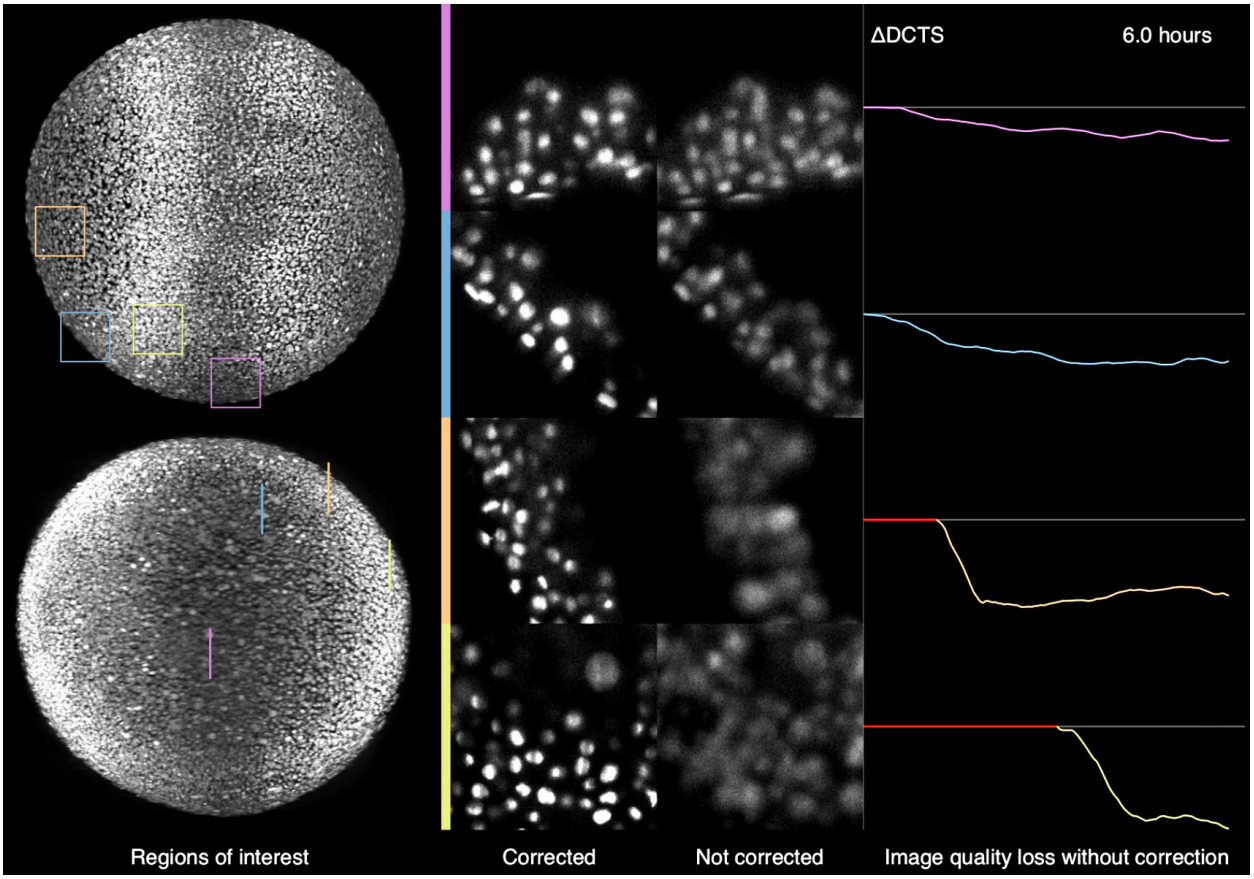

Nature Biotechnology: doi:10.1038/nbt.3708

Supplementary Video 7 | Quantification of resolution improvements in zebrafish adaptive imaging

Quality comparison (part 2, see previous video for part 1) of corrected and uncorrected time-lapse image data for the spatiotemporally adaptive imaging experiment shown in **Supplementary Video 6**. Complementing the visualizations and DCTS quantifications provided in **Supplementary Video 6**, this video additionally shows a side-by-side comparison and quantification of the frequency content of corrected and uncorrected image data. The first two columns show image data for four image regions and associated differences in DCTS values between corrected and uncorrected data, as presented also in **Supplementary Video 6**. The third column shows the same image data in Fourier space and indicates the cut-off radius in frequency space for corrected and uncorrected image data. The ratio of these radii for corrected and uncorrected image data is shown in the fourth column. Note that this measurement is performed *in vivo* and is thus bandwidth-limited as a result of the particular frequency characteristics of the fluorophore distribution in the embryo.

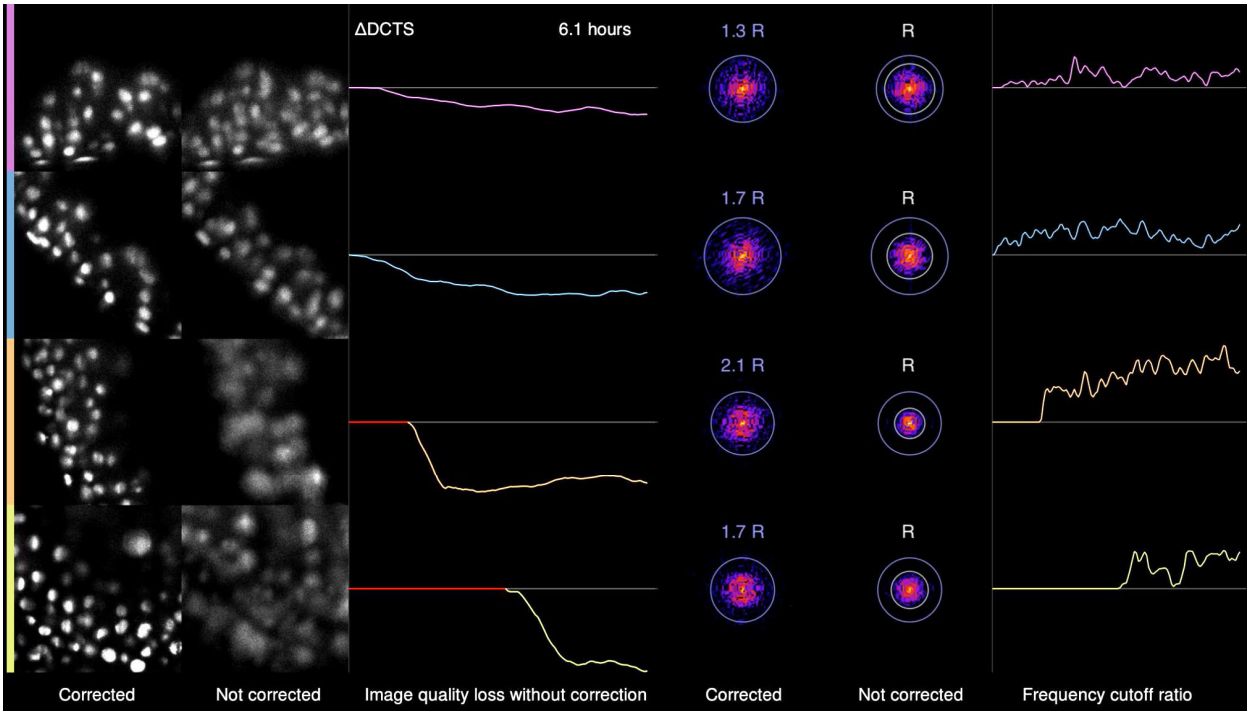

Nature Biotechnology: doi:10.1038/nbt.3708

Supplementary Video 8 | Spatiotemporally adaptive two-color imaging of nervous system development

Spatiotemporally adaptive two-color imaging of *Drosophila* embryonic development, using a ubiquitous nuclear fluorescent label (His2Av-mRFP1) as well as a fluorescent marker for the developing nervous system (deadpanEE-Gal4, UAS-myr::GFP). The video demonstrates how the imaging framework detects spatiotemporal changes in the expression pattern underlying the marker for the developing nervous system, starting with a red color channel that is initially completely devoid of signal. The top panel shows a two-color ventral-view maximum-intensity projection of the developing embryo (blue: ubiquitous nuclear RFP, orange: panneural membrane GFP). The two panels below show anterior-view maximum-intensity projections together with occupancy graphs that visualize the automated detection of signal by the adaptive imaging framework.

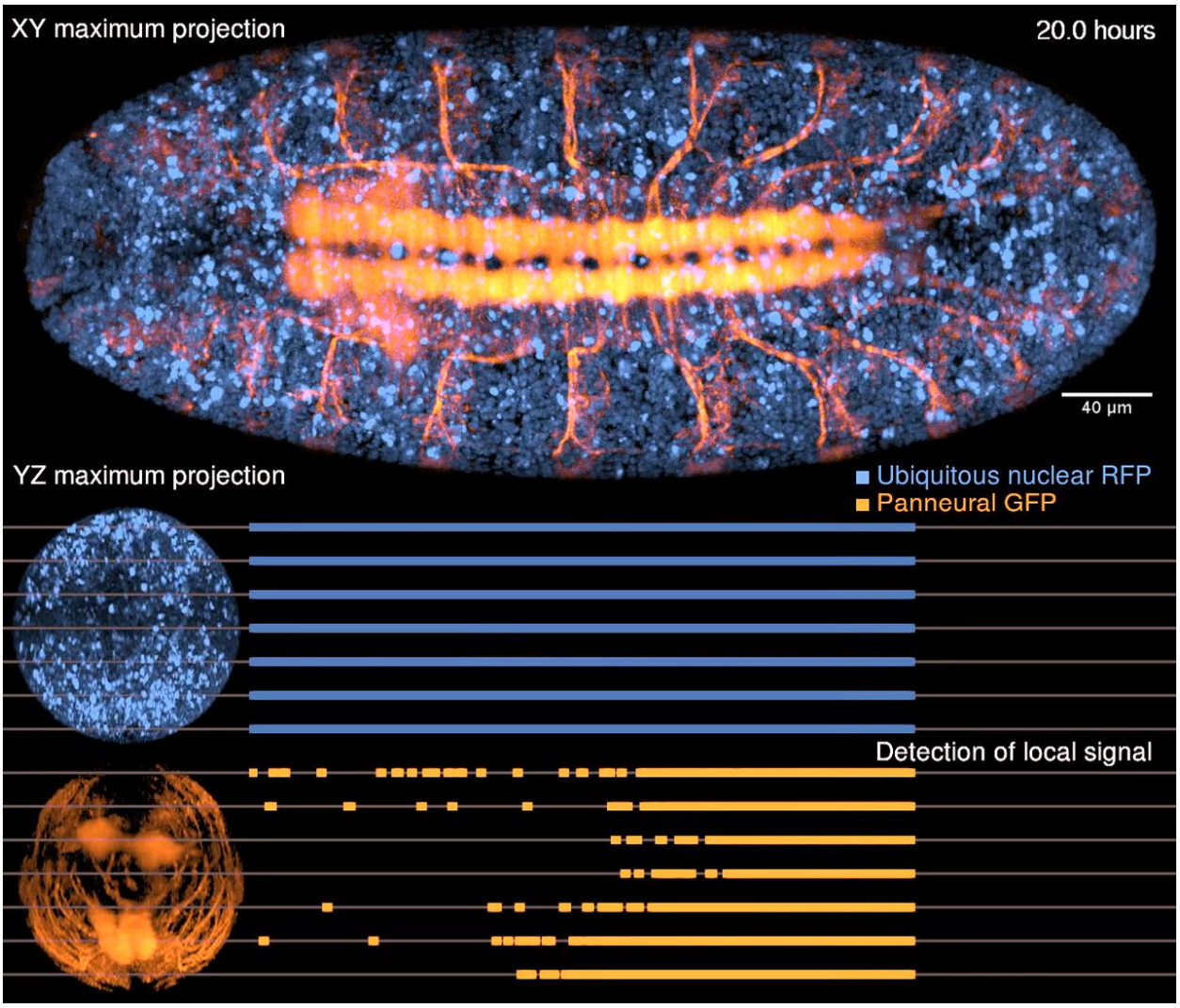

Nature Biotechnology: doi:10.1038/nbt.3708

Supplementary Video 9 | Spatiotemporally adaptive whole-brain functional imaging in larval zebrafish

Quality comparison of corrected and uncorrected time-lapse image data for a spatiotemporally adaptive whole-brain functional imaging experiment in *Tg(elavl3:GCaMP6f)* larval zebrafish (**Supplementary Table 10**). This side-by-side comparison demonstrates the recovery of single-cell resolution in multiple brain regions as well as substantial improvements in the fidelity of single-neuron activity traces by adaptive imaging. The left panel shows a dorsal-view maximum-intensity projection of one half of the brain and indicates the anatomical locations of the three regions shown to the right. For each region, image quality with and without adaptive imaging are shown for single planes (2nd and 3rd center columns), including a representation of ΔF/F for the corrected image data to highlight neuronal activity (1st center column). The two versions of the image data (corrected, uncorrected) were acquired by interleaving the time-lapse experiment, acquiring one complete brain volume every 375 ms and alternating between corrected and uncorrected microscope states in subsequent volumetric scans. Importantly, both versions of the experiment start with the same initial (optimized) microscope state, i.e. all microscope parameters are identical at time point 0. Adaptive imaging was performed for a total period of 20 hours, of which two high-speed sequences are shown at the 1-hour (first part of video) and 11-hour mark (second part of video), respectively. Loss of image quality without adaptive imaging is quantified as the difference in DCTS values of image data obtained for corrected and uncorrected system states (top right panel, grey line corresponds to ΔDCTS = 0). Activity traces are provided below the ΔDCTS panel for single neurons at locations indicated by green and red circles in the image panels to the left. In the early phase of the functional imaging experiment (1 h), image quality is comparable in midbrain regions but already substantially degraded without microscope adaptation in the forebrain. In the late phase of the experiment (11 h), all three brain regions are substantially degraded in the absence of microscope state corrections.

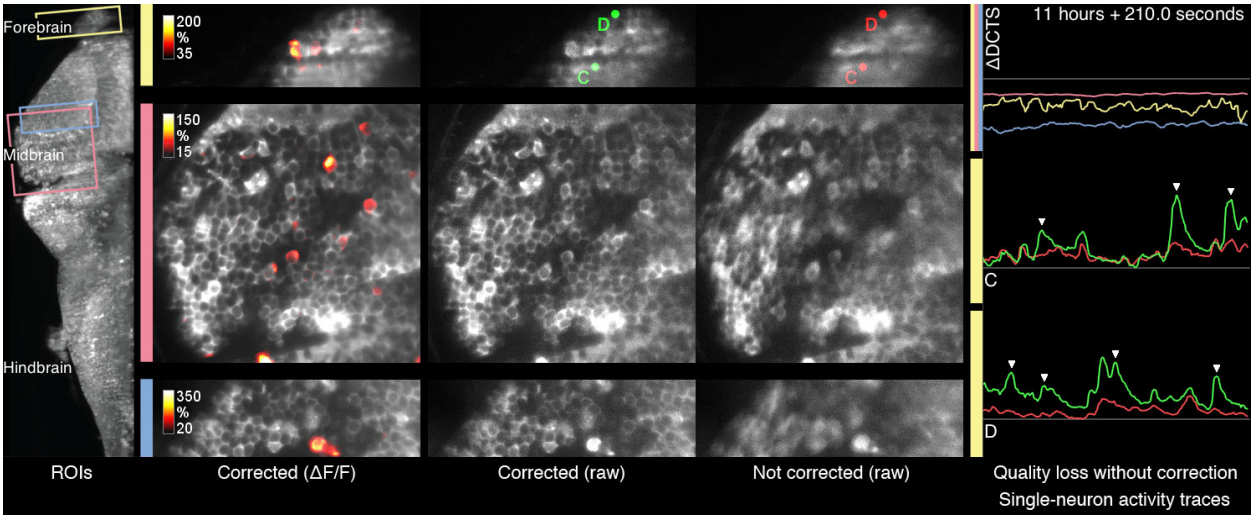

Nature Biotechnology: doi:10.1038/nbt.3708

Supplementary Video 10 | Example of system drift during non-adaptive long-term imaging

Example of a failed time-lapse imaging experiment of *Drosophila* embryogenesis (His2Av-mRFP1 embryo with fluorescently labeled cell nuclei) performed without adaptive imaging. The experiment failed because of system drift, specifically with respect to light-sheet offset positions controlled by PI S-334 tip/tilt mirrors[21], which degraded image quality substantially over time. In the absence of continuous, automated adaptation of the microscope to specimen- or system-induced dynamic changes, optimal positioning, orientation and co-planarity of light-sheets and detection focal planes can easily be compromised, leading to substantial degradation in image quality, in particular during long-term live imaging experiments. In the example shown here, the total acquisition period is dictated by the duration of embryonic development in *Drosophila* (22 hours). During the first two hours of imaging, the second light-sheet drifted out of focus due to thermal fluctuations that affected the positional stability of the tip/tilt mirrors. A human operator eventually intervened and corrected the microscope state. This correction was based on the observation of an obvious degradation in image quality, i.e. such manual corrections are only possible in extreme cases and require the operator to constantly screen the acquired image data. Moreover, such manual corrections are inevitably applied post-hoc, i.e. the quality of the experimental data has essentially already been compromised for an extended period of time, which precludes the use of data for quantitative image analysis and any form of advanced data mining, such as cell segmentation or cell tracking. After 2 hours, the second light-sheet drifted again and the human operator eventually applied another manual correction. However, as in the first correction step before, this correction occurs post-hoc, at a time when it is already too late to rescue this recording. In practice, without the use of an automated, spatiotemporally adaptive imaging system, a successful long-term recording can thus require several attempts and inevitably requires the investigator to accept some amount of system drift and reduction in spatial resolution due to lack of compensation for specimen-induced dynamic changes in optimal system parameters.

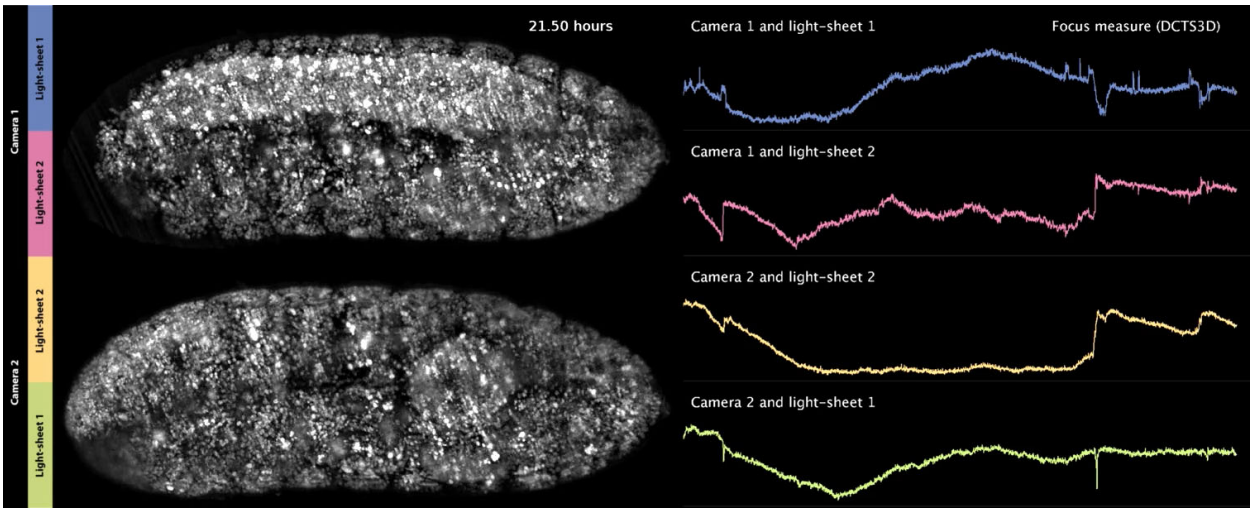

Nature Biotechnology: doi:10.1038/nbt.3708

References

1. Keller, P.J., Schmidt, A.D., Wittbrodt, J. & Stelzer, E.H.K. Reconstruction of zebrafish early embryonic development by scanned light sheet microscopy. *Science* **322**, 1065-1069 (2008).
2. Kristan, M., Pers, J., Perse, M. & Kovacic, S. A Bayes-spectral-entropy-based measure of camera focus using a discrete cosine transform. *Pattern Recogn Lett* **27**, 1431-1439 (2006).
3. Vollath, D. The influence of the scene parameters and of noise on the behavior of automatic focusing algorithms. *J Microsc* **151**, 133-146 (1988).
4. Yeo, T.T.E., Ong, S.H., Jayasooriah & Sinniah, R. Autofocusing for tissue microscopy. *Image Vision Comput* **11**, 629-639 (1993).
5. Nayar, S.K. & Nakagawa, Y. Shape from focus. *PAMI* **16**, 824-831 (1994).
6. Brenner, J.F. et al. An automated microscope for cytologic research a preliminary evaluation. *J Histochem Cytochem* **24**, 100-111 (1976).
7. Tian, Y., Shieh, K. & Wildsoet, C.F. Performance of focus measures in the presence of nondefocus aberrations. *J Opt Soc Am A* **24**, B165-B173 (2007).
8. Sun, Y., Duthaler, S. & Nelson, B.J. Autofocusing in computer microscopy: selecting the optimal focus algorithm. *Microsc Res Techniq* **65**, 139-149 (2004).
9. Groen, F.C.A., Young, I.T. & Ligthart, G. A comparison of different focus functions for use in autofocus algorithms. *Cytometry* **6**, 81-91 (1985).
10. Xie, H., Rong, W.B. & Sun, L.N. Construction and evaluation of a wavelet-based focus measure for Microscopy Imaging. *Microsc Res Techniq* **70**, 987-995 (2007).
11. Kautsky, J., Flusser, J., Zitova, B. & Simberova, S. A new wavelet-based measure of image focus. *Pattern Recogn Lett* **23**, 1785-1794 (2002).
12. Wendykier, P. & Nagy, J.G. Large-scale image deblurring in Java. *Lect Notes Comput Sc* **5101**, 721-730 (2008).
13. Frigo, M. & Johnson, S.G. The design and implementation of FFTW3. *P IEEE* **93**, 216-231 (2005).
14. Roberts, L.G. Picture coding using pseudo-random noise. *Ire T Inform Theor* **8**, 145 (1962).
15. Tian, Y.B. Monte Carlo evaluations of ten focus measures. *P Soc Photo-Opt Ins* **6502**, C5020-C5020 (2007).
16. Born, M. & Wolf, E. Principles of optics: electromagnetic theory of propagation, interference and diffraction of light, Edn. 7th expanded. (Cambridge University Press, Cambridge; 1999).
17. Blinn, J.F. What's that deal with the DCT? *IEEE Comput Graph* **13**, 78-83 (1993).
18. Ahmed, N., Natarajan, T. & Rao, K.R. Discrete Cosine Transform. *IEEE Trans Comp* **C-23**, 90-93 (1974).
19. Royer, L., Reimann, M., Stewart, A.F. & Schroeder, M. Network compression as a quality measure for protein interaction networks. *PLoS ONE* **7**, e35729 (2012).
20. Keller, P.J. et al. Fast, high-contrast imaging of animal development with scanned light sheet-based structured-illumination microscopy. *Nat Methods* **7**, 637-642 (2010).

Nature Biotechnology: doi:10.1038/nbt.3708

21. Tomer, R., Khairy, K., Amat, F. & Keller, P.J. Quantitative high-speed imaging of entire developing embryos with simultaneous multiview light-sheet microscopy. *Nat Methods* **9**, 755-763 (2012).
22. Barata, J.C.A. & Hussein, M.S. The Moore-Penrose pseudoinverse: a tutorial review of the theory. *Braz J Phys* **42**, 146-165 (2012).
23. Kelley, C.T. Iterative methods for optimization. (SIAM, Philadelphia; 1999).
24. Tomer, R., Khairy, K., Amat, F. & Keller, P.J. Quantitative high-speed imaging of entire developing embryos with simultaneous multiview light-sheet microscopy. *Nat Methods* **9**, 755-763 (2012).
25. Ahrens, M.B., Orger, M.B., Robson, D.N., Li, J.M. & Keller, P.J. Whole-brain functional imaging at cellular resolution using light-sheet microscopy. *Nat Methods* **10**, 413-420 (2013).
26. Stewart, C.V. Robust parameter estimation in computer vision. *SIAM Review* **41**, 513-537 (1999).
27. Keller, P.J. in Microtubule dynamic instability analyzed in three dimensions over time with selective plane illumination microscopy and modeling of yeast sporulation (University of Heidelberg, Heidelberg; 2005).
28. Duck, F.A. Physical properties of tissue: a comprehensive reference book. (Academic Press Inc., San Diego; 1990).
29. Supatto, W., McMahon, A., Fraser, S.E. & Stathopoulos, A. Quantitative imaging of collective cell migration during Drosophila gastrulation: multiphoton microscopy and computational analysis. *Nat Protoc* **4**, 1397-1412 (2009).

Nature Biotechnology: doi:10.1038/nbt.3708